

Electronic Thesis and Dissertation Repository

6-22-2011 12:00 AM

Structure and Strength: Anisotropic Polyvinyl Alcohol Hydrogels and Spider Mite Silk Fibres

Stephen Hudson, *The University of Western Ontario*

Supervisor: Dr. Jeffrey Hutter, *The University of Western Ontario*

A thesis submitted in partial fulfillment of the requirements for the Doctor of Philosophy degree in Physics

© Stephen Hudson 2011

Follow this and additional works at: <https://ir.lib.uwo.ca/etd>

 Part of the [Condensed Matter Physics Commons](#)

Recommended Citation

Hudson, Stephen, "Structure and Strength: Anisotropic Polyvinyl Alcohol Hydrogels and Spider Mite Silk Fibres" (2011). *Electronic Thesis and Dissertation Repository*. 185.
<https://ir.lib.uwo.ca/etd/185>

This Dissertation/Thesis is brought to you for free and open access by Scholarship@Western. It has been accepted for inclusion in Electronic Thesis and Dissertation Repository by an authorized administrator of Scholarship@Western. For more information, please contact wlsadmin@uwo.ca.

**STRUCTURE AND STRENGTH: ANISOTROPIC POLYVINYL
ALCOHOL HYDROGELS AND SPIDER MITE SILK FIBRES**

(Spine title: Structure and Strength: PVA Hydrogels and Spider Mite Silk)

(Thesis format: Integrated Article)

by

Stephen Hudson

Graduate Program in Physics

A thesis submitted in partial fulfillment
of the requirements for the degree of
Doctor of Philosophy

The School of Graduate and Postdoctoral Studies
The University of Western Ontario
London, Ontario, Canada

© Stephen Donald Hudson 2011

THE UNIVERSITY OF WESTERN ONTARIO
School of Graduate and Postdoctoral Studies
CERTIFICATE OF EXAMINATION

Supervisor:

.....
Dr. J. L. Hutter

Supervisory Committee:

.....
Dr. T. L. Poepping

.....
Dr. M. Zinke-Allmang

Examiners:

.....
Dr. J. R. de Bruyn

.....
Dr. T. L. Poepping

.....
Dr. J. T. Wood

.....
Dr. T. A. Harroun

The thesis by

Stephen Donald Hudson

entitled:

**Structure and Strength: Anisotropic Polyvinyl Alcohol Hydrogels and Spider Mite
Silk Fibres**

is accepted in partial fulfillment of the
requirements for the degree of
Doctor of Philosophy

.....
Date

.....
Chair of the Thesis Examination Board

Abstract

Polyvinyl alcohol (PVA) is a hydrophilic, biocompatible polymer which can be made into physically cross-linked hydrogels by freezing and thawing PVA solution. These hydrogels can be made with anisotropic mechanical properties closely matching those of porcine aorta, making them a promising material for producing artificial heart valves and heart valve stents.

Small- and ultra small-angle neutron scattering has been used to study the structure of isotropic and anisotropic PVA hydrogels at length-scales of 2 nm to 10 μm . By supplementing the neutron data with data from atomic force microscopy, a large range of length-scales have been probed, within which structural changes responsible for bulk anisotropy occur. The gel is modelled as interconnected PVA blobs of size 20 to 50 nm arranged in fractal aggregates extending to micrometers or tens of micrometers. Bulk mechanical anisotropy appears to be due to the alignment of blobs and connections between blobs.

To further understand the connection between structure and bulk mechanical properties, the uniaxial extension behaviour of isotropic PVA hydrogels was modelled using the 3-chain and 8-chain models, and anisotropic versions of the models were developed for modelling the behaviour of anisotropic PVA hydrogels. The mechanical models are compatible with the structural model described above. The models show that the most highly extended strands dominate the entropy and that there are more dominant strands aligned in the direction for which the gel is strongest than in the other directions.

Nanostructures can be used to reinforce materials, such as PVA hydrogels, providing

a new method to alter the properties of materials. The spider mite genome was recently sequenced, possibly allowing for spider mite silks with bioengineered properties and new polymer-silk nanocomposite materials. Despite this progress, little is known about the properties of natural spider mite silks. The fibres have diameters of tens of nanometres in comparison to typical spider silk fibres with diameters of several microns. 3-point bending tests were performed with an atomic force microscope to determine the mechanical properties of single spider mite fibres and a new model which accounts for bending, stretching, and an initial tensile stress was developed. Adult and larval fibres have Young's moduli of 24 ± 3 GPa and 15 ± 3 GPa, respectively. Both adult and larval fibres have an estimated ultimate strength of 200–300 MPa and a toughness of order 9 MJ/m^3 .

Keywords: polymer, polyvinyl alcohol, hydrogel, anisotropic, soft tissue, neutron scattering, small-angle neutron scattering, ultra small-angle neutron scattering, atomic force microscopy, mechanical properties, spider mite, silk, nanofibre, modulus, ultimate strength, toughness

Co-Authorship Statement

Chapters 3, 4, and 5 contain material from one published journal article and two manuscripts which have been submitted to refereed journals for review. Stephen Hudson took the lead role in writing all three of these manuscripts.

Chapter 3 was authored by Stephen Hudson and co-authored by Jeffrey Hutter, Mu-Ping Nieh, Jeremy Pencer, Leonardo Millon, and Wankei Wan. Millon, under the supervision of Wan and with assistance from Hudson, prepared hydrogel samples for neutron scattering experiments. Hudson, assisted by Hutter, performed the majority of the neutron scattering experiments. In order to make efficient use of the time on the instrument, Hudson and Hutter's neutron beam time was combined with Nieh and Pencer's beam time. Nieh and Pencer gave instruction on data analysis and collected a small amount of data for Hudson during the time that their samples were in the neutron beam. Hudson prepared samples for and performed the atomic force microscopy. Hudson reduced, modelled, and analyzed the neutron scattering data with assistance from Hutter.

Chapter 4 was authored by Stephen Hudson and co-authored by Jeffrey Hutter, Leonardo Millon, Mu-Ping Nieh, and Wankei Wan. Hudson prepared hydrogel samples for neutron scattering experiments. Hudson performed the neutron scattering experiments with assistance from Nieh. Millon provided uniaxial extension mechanical testing data of hydrogels. Hudson prepared samples for and performed uniaxial extension testing to determine the temperature dependence of mechanical strength with assistance from Millon. Under the supervision of Hutter, Hudson reduced the data, developed a new model to explain the

anisotropy of the material, and fit the data.

Chapter 5 was authored by Stephen Hudson and co-authored by Jeffrey Hutter, Vladimir Zhurov, and Miodrag Grbić. Zhurov cared for spider mites and allowed them to deposit silk fibres on silicon gratings. Under the supervision of Hutter, Hudson performed atomic force microscopy to measure the mechanical properties of the silk fibres. Hutter provided the foundation of the software needed to analyze the force measurements. Hudson extended the software's capabilities by adding the ability to calculate force versus fibre displacement from standard force curves, by implementing a model for the force versus displacements curves which considers bending and tensile stresses, and by adding the ability to estimate the ultimate strength and toughness of the fibres.

Acknowledgements

This thesis was made possible by the support of many people. I would like to thank them for their academic support and for making my time at Western memorable and fulfilling.

Foremost, I would like to thank my supervisor Dr. Jeffrey Hutter for his guidance, training, and thoughtful suggestions. Dr. Hutter has encouraged me to develop a broad set of skills and has allowed me the freedom to pursue many interests.

Many thanks to the collaborators who have helped to make this project successful. I am thankful for the opportunity to work with Dr. Leonardo Millon and Dr. W. K. Wan on anisotropic polyvinyl alcohol (PVA) hydrogels and for the training Dr. Millon provided on the mechanical testing system. I thank Dr. Mu-Ping Nieh for guidance and helpful suggestions regarding the neutron scattering studies. Special thanks go to Dr. Vladimir Zhurov and Dr. Miodrag Grbić for the opportunity to study spider mite silk nanofibres. Their enthusiasm helped the project move forward quickly.

It has been a pleasure to work with great colleagues and friends. In particular, I acknowledge my lab mates Shailesh Nene, Nan Yang, and Mark Gooyers. I am grateful to Brian Dalrymple for providing training in the machine shop and for assistance with the design and construction of assorted apparatuses including moulds used to produce PVA hydrogels.

I am grateful to my wonderful parents, Don and Deborah, and to the rest of my family for providing the love, encouragement, and support which have allowed me to pursue my Ph.D. and to complete this thesis. Above all, I am sincerely grateful to my beautiful wife

Parisa for the love and support she has provided over the years, and for the strength she has shown and the sacrifices she has made for our newborn son during the most challenging part of our graduate careers.

I acknowledge research funding from the Natural Sciences and Engineering Research Council of Canada (NSERC), the Advanced Foods and Materials Network, and the Western Graduate Thesis Research Fund Awards. I am grateful for scholarship support from the NSERC Postgraduate Scholarship and the Ontario Graduate Scholarship programs.

Lastly, I acknowledge the support of the National Institute of Standards and Technology, U.S. Department of Commerce, in providing the neutron research facilities used in this work, and local contacts Min Lin and Steven Kline for assisting with the neutron scattering. The neutron scattering work utilized facilities supported in part by the National Science Foundation under Agreement No. DMR-0944772.

Contents

Certificate of Examination	ii
Abstract	iii
Co-Authorship Statement	v
Acknowledgements	vii
Table of Contents	ix
List of Tables	xii
List of Figures	xiii
List of Appendices	xvi
List of Abbreviations	xvii
1 Introduction	1
1.1 Motivation	1
1.2 Objective	3
1.3 Thesis Organization	4
1.4 Bibliography for Chapter 1	5
2 Literature Review	7
2.1 Hydrogels	7
2.1.1 Diverse Compositions and Properties	7
2.1.2 Applications in Medicine	7
2.2 Neutron Scattering	13
2.2.1 Scattering Theory	15
2.2.2 Small-Angle Neutron Scattering	21
2.2.3 Ultra Small-Angle Neutron Scattering	21

2.3	Atomic Force Microscopy	22
2.4	Equilibrium of Beams and Fibres	26
2.4.1	Bending Moments	28
2.4.2	Shear Forces and Distributed Loads	30
2.5	Bibliography for Chapter 2	34
3	Characterization of Anisotropic PVA Hydrogel by SANS and USANS	37
3.1	Introduction	37
3.2	Materials and Methods	38
3.2.1	Sample Preparation	38
3.2.2	Neutron Scattering	39
3.2.3	Data Reduction	43
3.2.4	Atomic Force Microscopy	44
3.3	Theory and Data Analysis	44
3.3.1	Solution	45
3.3.2	Hydrogel	46
3.3.3	Data Fitting	50
3.4	Discussion	54
3.4.1	Isotropic Gels	55
3.4.2	Anisotropic Gels	60
3.5	Conclusion	62
3.6	Bibliography for Chapter 3	63
4	Anisotropic Polyvinyl Alcohol Hydrogel: Connection Between Structure and Bulk Mechanical Properties	66
4.1	Introduction	66
4.2	Materials and Methods	69
4.2.1	Neutron Scattering	69
4.2.2	Mechanical Testing	71
4.3	Theory and Data Analysis	72
4.3.1	Neutron Scattering	72
4.3.2	Stress of Entropic Polymer Networks	73
4.3.3	Uniaxial Extension of Isotropic Hydrogels	75
4.3.4	Uniaxial Extension of Anisotropic Hydrogels	80
4.3.5	Temperature Dependence of Stress Versus Strain	89
4.4	Discussion	93

4.4.1	Isotropic Hydrogels	93
4.4.2	Anisotropic Hydrogels	95
4.4.3	Temperature Dependence of Stress Versus Strain	99
4.4.4	Connection Between Structural and Mechanical Models	99
4.5	Conclusion	101
4.6	Bibliography for Chapter 4	103
5	Measurement of the Elastic Modulus of Spider Mite Silk Fibres Using the Atomic Force Microscope	106
5.1	Introduction	106
5.2	Materials and Methods	107
5.3	Theory and Data Analysis	109
5.3.1	Pure Bending	111
5.3.2	Bending With Deformation-Induced Tension	113
5.3.3	Bending With Both Deformation-Induced Tension and an Initial Tension	114
5.3.4	Analysis of Force Curves	115
5.4	Discussion	120
5.5	Conclusion	122
5.6	Bibliography for Chapter 5	124
6	Conclusions	126
6.1	Thesis Summary	126
6.2	Future Work	127
6.2.1	Mechanical Modelling of PVA hydrogels	127
6.2.2	Spider Mite Silk Fibres	128
6.3	Bibliography for Chapter 6	129
7	Curriculum Vitae	140

List of Tables

3.1	NG3 SANS configurations.	40
3.2	PVA samples produced and scattering techniques used.	42
3.3	Fractal aggregate sizes as determined by fitting Eq. 3.7 to combined SANS and USANS data.	51
3.4	Blob sizes as determined by fitting Eq. 3.7 to combined SANS and USANS data.	51
4.1	NG7 SANS configurations.	70
4.2	Blob size R versus the number of thermal cycles.	74
4.3	Estimates of the number of links per strand n_K , the number of strands per cubic metre N , and the percentage of monomers contained in strands that contribute to network strength.	100
5.1	Silk fibre lengths, diameters, moduli, and initial tensions for samples prepared with adults and larvae, adults only, and larvae only.	119
5.2	Comparison of the elastic modulus, tensile strength, breaking strain, and toughness of adult spider mite, spider, and silkworm silks.	122

List of Figures

2.1	Moulds used to produce PVA hydrogel ultrasound phantoms for Prof. Tamie Poepping’s ultrasonics group at The University of Western Ontario, Canada.	9
2.2	PVA hydrogel MRI phantoms used to measure image artifacts caused metals commonly used in implants and prostheses.	10
2.3	Comparison of the finite element method results and the ultrasound images in support of the simulation in the opening phase.	13
2.4	Incident wave of neutrons scattered towards a detector by the nuclei located at positions M and P.	15
2.5	Illustration of the scattering vector defined by Eq. 2.4 and the scattering vector 2θ .	17
2.6	A schematic diagram of the NG-3 30 m small-angle neutron scattering (SANS) instrument located at the National Institute of Standards and Technology (NIST).	22
2.7	A schematic layout of the BT-5 perfect crystal diffractometer located at the NIST.	23
2.8	Schematic of an atomic force microscope.	25
2.9	Small element of a deflected beam or fibre.	27
2.10	Small element of a beam bent by bending moments M at each end.	28
2.11	Illustration, used for finding equilibrium of torques and forces, of bending moments M and $M + dM$ (blue), shear forces V and $V + dV$ (green) and a distributed load q (orange) acting on a small element of a beam or fibre.	31
3.1	Raw SANS data for isotropic (left column) and anisotropic (right column) cycle-six PVA hydrogels using the NG3 configurations shown in Table 3.1.	41
3.2	Differential scattering cross-section from PVA solution after reduction to an absolute scale and circular averaging.	46
3.3	Schematic of the structure showing aggregates of size ξ_1 , blobs of size R , and the fixed polymer length-scale ξ_{fixed}	50
3.4	Differential scattering cross-section from a cycle-one PVA hydrogel.	52

3.5	Differential scattering cross-sections from cycle-one, -three, and -six PVA hydrogels.	53
3.6	Differential scattering cross-sections from cycle-six PVA hydrogels.	54
3.7	Surface fractal dimension versus processing strain.	55
3.8	Fixed gel length-scale versus processing strain.	56
3.9	Gel exponent versus processing strain.	57
3.10	Contact mode atomic force microscopy images of a cycle-ten PVA hydrogel that were taken under fluid.	59
4.1	Differential scattering cross-sections from cycle-one and cycle-ten hydrogels.	73
4.2	Unit cell of the isotropic 3-chain network model.	76
4.3	Engineering stress versus engineering strain, for isotropic hydrogels produced with one through six thermal cycles, with fits of the 3-chain model.	78
4.4	Unit cell of the isotropic 8-chain network model.	80
4.5	Engineering stress versus engineering strain, for isotropic hydrogels produced with one through six thermal cycles, with fits of the 8-chain model.	81
4.6	Engineering stress versus engineering strain for isotropic and anisotropic hydrogels produced with two thermal cycles.	82
4.7	Engineering stress versus engineering strain for anisotropic hydrogels for uniaxial extension a) perpendicular and b) parallel to the processing strain with solid and dashed curves showing fits of the anisotropic 3-chain model.	86
4.8	Engineering stress versus engineering strain for anisotropic hydrogels for uniaxial extension a) perpendicular and b) parallel to the processing strain with solid and dashed curves showing fits of the anisotropic 8-chain model.	88
4.9	Effective elastic moduli of cycle-two and cycle-six PVA hydrogels as a function of temperature.	89
4.10	Effective elastic moduli of cycle-two and cycle-six PVA hydrogels as a function of temperature.	90
4.11	Equilibrium fractional extension of polymer strands in cycle-two and cycle-six PVA hydrogels as a function of temperature determined by fitting the 3-chain isotropic model to uniaxial extension engineering stress versus engineering strain data.	91
4.12	Equilibrium fractional extension of polymer strands in cycle-two and cycle-six PVA hydrogels as a function of temperature determined by fitting the 8-chain isotropic model to uniaxial extension engineering stress versus engineering strain data.	92

4.13	Equilibrium fractional extensions of strands for isotropic, x_0 , and anisotropic, $u_{1,0}$, $v_{1,0}$, $u_{2,0}$, and $v_{2,0}$, hydrogels determined by fitting the 3-chain model to experimental engineering stress versus engineering strain data.	94
4.14	Equilibrium fractional extensions of strands for isotropic, x_0 , and anisotropic, $u_{1,0}$ and $u_{2,0}$, hydrogels determined by fitting the 8-chain model to experimental engineering stress versus engineering strain data.	95
4.15	Effective elastic moduli for isotropic, G , and anisotropic hydrogels determined by fitting the 3-chain model to experimental engineering stress versus engineering strain data.	96
4.16	Effective elastic moduli for isotropic, G , and anisotropic hydrogels determined by fitting the 8-chain model to experimental engineering stress versus engineering strain data.	97
5.1	5.3 $\mu\text{m} \times 5.3 \mu\text{m}$ contact atomic force microscopy (AFM) image of a spider mite silk fibre suspended over a trench.	109
5.2	AFM force-volume (FV) height image of the same spider mite silk fibre shown in Fig. 5.1.	110
5.3	Diagram of the segment of fibre under analysis a) before clamping and without initial tension, b) after application of initial tension and clamping to grating but before contact with AFM cantilever tip, and c) after contact with AFM cantilever tip.	112
5.4	AFM force curves obtained by pushing against a suspended fibre (solid curve) and rigid substrate (dashed curve).	116
5.5	Experimental force versus displacement curves of single silk fibres with relatively low and relatively high initial tensions.	117
5.6	The Young's Modulus, obtained from fitting individual force curves, displayed versus the position of the force curve on the fibre as a fraction of the fibre length.	118
A.1	Glass bead glued to a triangular NP-S cantilever.	132

List of Appendices

Appendix A. Attachment of Microspheres to Atomic Force Microscope Cantilevers	131
Appendix B. Copyright Permissions	133

List of Abbreviations

AFM atomic force microscopy

BC bacterial cellulose

BNCT boron neutron capture therapy

FV force-volume

MRI magnetic resonance imaging

NIST National Institute of Standards and Technology

PVA polyvinyl alcohol

SANS small-angle neutron scattering

STM scanning tunnelling microscopy

USANS ultra small-angle neutron scattering

UV ultraviolet

Chapter 1

Introduction

1.1 Motivation

The human body is a marvel of evolution, and its complexity and robustness are astonishing, but it has limitations. For instance, our bodies cannot consistently eliminate and recover from all infections and diseases, and cannot fully repair all types of tissue damage caused by injury. These limitations are so pervasive that in Canada in 2008, each Canadian had an average of five to six consultations with doctors during the year and total health-care expenditure was 10.4% of the gross domestic product [1]. The natural sciences and engineering provide materials, such as hydrogels, which are used for diagnosis, drug delivery, and tissue repair, helping medicine to achieve its goal of improving our longevity and quality of life.

Hydrogels are viscoelastic solids with cross-linked networks, commonly comprised of proteins or polymers, that are swollen with water. The vast number of proteins and polymers capable of forming hydrogels yields many materials which are useful to medicine and engineering. In medicine, hydrogels are used for testing and calibrating medical imaging devices, for delivering drugs, and for aiding healing and tissue repair.

Polyvinyl alcohol (PVA) is a biocompatible polymer that has been used to make hy-

drogels for many medical applications. PVA can be made into a hydrogel by dissolution in water and cross-linking to create a polymer network. PVA is very hydrophilic and as a result its hydrogels exhibit a high degree of swelling and can contain greater than 90% *w/w* water. Cross-links may be chemical or physical. Physically cross-linked hydrogels are generally the most biocompatible because they are free of residual cross-linking agents. One promising physically cross-linked PVA hydrogel is made by freezing and thawing PVA solution. During the freeze/thaw thermal cycle, formation of PVA crystallites is induced as the concentration of PVA increases in the spaces between ice crystals. The crystallites act as cross-links and are essentially permanent at physiological temperatures. This particular PVA hydrogel is significant because the mechanical properties are similar to those of soft biological tissue. The mechanical properties of this hydrogel can be controlled by changing the PVA concentration, the PVA molecular weight, the time held frozen during a thermal cycle, the thawing rate, and the number of thermal cycles [2–4].

The ability to control mechanical properties is critical for many applications. For instance, compliance mismatch between the the aortic root and an artificial heart valve can lead to tissue fatigue and premature failure [5–8]. Cardiovascular tissue exhibits nonlinear elastic behaviour due to strain stiffening and is anisotropic. With suitable thermal cycle parameters, PVA hydrogels can be made to match the nonlinear mechanical properties of porcine aorta [4]. Further, by producing a one-cycle hydrogel in the form of a cylindrical shell, stretching the hydrogel over a cylinder with larger diameter, and subjecting the hydrogel to at least one additional thermal cycle, it is possible to produce an anisotropic PVA hydrogel whose longitudinal and axial tensile properties simultaneously match those of porcine aorta [9]. Therefore, the material is a good candidate for producing cardiovascular prosthesis such as aortic stents.

Greater variety and control of mechanical properties can be obtained by reinforcing PVA hydrogels with, e.g., bacterial cellulose nanofibres, hydroxyapatite, or clay nanoparticles [10–16]. Spider mite silk is another biocompatible material which may be useful

for creating new nanocomposite materials, but whose mechanical properties have not been characterized. In order to develop new composite PVA materials, it is important to understand both the microstructure and the relationship between structure and bulk properties of PVA hydrogels, to determine the mechanical properties of the reinforcing material, and to understand the interaction between the polymer network and the reinforcing material.

1.2 Objective

The overall goal of this research is to characterize the microstructure of PVA hydrogels, to make a quantitative connection between microstructure and bulk properties of PVA hydrogels, and to measure the mechanical properties of silk nanofibres which have potential use in biomedical engineering.

The specific objectives are:

1. To characterize the microstructure of isotropic and anisotropic PVA hydrogels using small-angle neutron scattering (SANS), ultra small-angle neutron scattering (USANS), and atomic force microscopy (AFM);
2. To identify the structural features that determine bulk mechanical properties including anisotropy of the modulus;
3. To further our understanding of the link between structure and bulk mechanical properties by developing a model of the bulk mechanical properties which is motivated by the observed microstructure; and
4. To measure the mechanical strength of silk nanofibres using AFM.

1.3 Thesis Organization

Chapter 2 gives a review of literature relevant to this thesis. The properties of hydrogels useful to medicine are discussed. Afterwards, examples of hydrogels used for medical diagnosis, for drug delivery, and for tissue repair are reviewed. Next, the foundation of this work is established by reviewing available literature on the structure and mechanical properties of PVA hydrogels. Finally, the experimental techniques and theoretical concepts used in this study are described.

Chapter 3 presents SANS, USANS, and AFM experiments and modelling of isotropic and anisotropic PVA hydrogel structure. The structural features responsible for anisotropy are discussed. The content is adapted from a published journal article [17].

Chapter 4 presents a mechanical model, motivated by the structural model developed in Chapter 3, which explains the observed stress versus strain behaviour of isotropic and anisotropic PVA hydrogels. The content is adapted from a manuscript which is being prepared for publication.

Chapter 5 presents a model for determining the mechanical properties of pretensioned nanofibres from three-point bending tests. The model is applied to AFM measurements of spider mite silk nanofibres to determine the Young's modulus and to estimate the ultimate strength and toughness of the fibres. The content is adapted from a manuscript which is being prepared for publication.

Finally, Chapter 6 summarizes the results of the presented research and discusses how they address the objectives outlined above and how the results impact the relevant fields. Recommendations for future work are made.

1.4 Bibliography for Chapter 1

1. OECD *OECD Health Data* doi:<http://dx.doi.org/10.1787/data-00350-en> ;/content/data/data-00350-enj.
2. Trieu, H. & Qutubuddin, S. “Poly(vinyl alcohol) hydrogels: 2. Effects of processing parameters on structure and properties.” *Polym.* **36**, 2531–2539 (1995).
3. Hassan, C. M. & Peppas, N. A. “Structure and Applications of Poly(vinyl alcohol) Hydrogels Produced by Conventional Crosslinking or by Freezing/Thawing Methods.” *Adv. Polym. Sci.* **153**, 37–65 (2000).
4. Wan, W. K., Campbell, G., Zhang, Z. F., Hui, A. J. & Boughner, D. R. “Optimizing the Tensile Properties of Polyvinyl Alcohol Hydrogel for the Construction of a Bioprosthetic Heart Valve Stent.” *J. Biomed. Mater. Res.* **63**, 854–861 (2002).
5. Hansen, B., Menkis, A. H. & Vesely, I. “Longitudinal and Radial Distensibility of the Porcine Aortic Root.” *Ann. Thorac. Surg.* **60**, S384–S390 (1995).
6. Schoen, F. J. & Levy, R. J. “Tissue heart valves: Current challenges and future research perspectives.” *J. Biomed. Mater. Res.* **47**, 439–465 (1999).
7. Haruguchi, H. & Teraoka, S. “Intimal hyperplasia and hemodynamic factors in arterial bypass and arteriovenous grafts: a review.” *J. Artif. Organs* **6**, 227–235 (2003).
8. Rashid, S. T., Salacinski, H. J., Fuller, B. J., Hamilton, G. & Seifalian, A. M. “Engineering of bypass conduits to improve patency.” *Cell Prolif.* **37**, 351–366 (2004).
9. Millon, L. E., Mohammadi, H. & Wan, W. K. “Anisotropic Polyvinyl Alcohol Hydrogel for Cardiovascular Applications.” *J. Biomed. Mater. Res. Part B: Appl. Biomater.* **79B**, 305–311 (2006).
10. Millon, L. E. & Wan, W. K. “The Polyvinyl Alcohol-Bacterial Cellulose System As a New Nanocomposite for Biomedical Applications.” *J. Biomed. Mater. Res. Part B: Appl. Biomater.* **79B**, 245–253 (2006).
11. Millon, L. E., Guhadós, G. & Wan, W. “Anisotropic Polyvinyl Alcohol – Bacterial Cellulose Nanocomposite for Biomedical Applications.” *J. Biomed. Mater. Res. B: Appl. Biomater.* **86B**, 444–452 (2008).
12. Millon, L. E., Oates, C. J. & Wan, W. “Compression Properties of Polyvinyl Alcohol – Bacterial Cellulose Nanocomposite.” *J. Biomed. Mater. Res. B: Appl. Biomater.* **90B**, 922–929 (2009).

13. Wu, G., Su, B., Zhang, W. & Wang, C. “*In vitro* behaviors of hydroxyapatite reinforced polyvinyl alcohol hydrogel composite.” *Mater. Chem. Phys.* **107**, 364–369 (2008).
14. Xu, F., Li, Y., Deng, Y. & Xiong, J. “Porous nano-hydroxyapatite/poly(vinyl alcohol) composite hydrogel as artificial cornea fringe: characterization and evaluation in vitro.” *J. Biomater. Sci. Polymer Edn.* **19**, 431–439 (2008).
15. Pan, Y., Xiong, D. & Gao, F. “Viscoelastic behavior of nano-hydroxyapatite reinforced poly(vinyl alcohol) gel biocomposites as an articular cartilage.” *J. Mater. Sci.-Mater. M.* (2008).
16. Kokabi, M., Sirousazar, M. & Hassan, Z. M. “PVAclay nanocomposite hydrogels for wound dressing.” *Eur. Polym. J.* **43**, 773–781 (2007).
17. Hudson, S. D. *et al.* “Characterization of anisotropic poly(vinyl alcohol) hydrogel by small- and ultra-small-angle neutron scattering.” *J. Chem. Phys.* **130**, 034903:1–9 (2009).

Chapter 2

Literature Review

2.1 Hydrogels

2.1.1 Diverse Compositions and Properties

Hydrogels can be made from a large number of natural and synthetic polymers. Some biocompatible natural polymers are chitosan, polylysine, collagen, fibrin, dextran, and aragose, while some biocompatible synthetic polymers are polyethylene glycol, polylactic acid, polyacrylamide, polyvinyl acetate, and polyvinyl alcohol [1].

Hydrogels may be chemically cross-linked through covalent bonds or physically cross-linked by entanglements, ionic bonding, hydrogen bonding, or crystallite formation. Typically, physical gelation is reversible and may be controlled with temperature, pH, or ion concentration [1–3].

2.1.2 Applications in Medicine

Diagnosis and Dosimetry

Magnetic resonance and ultrasound imaging systems are commonly used for imaging anatomic structure and function. Accurate imaging is always desired, and in some cases, it is crit-

ically important. For instance, the location and shape of tumours must be accurately determined prior to radiation therapy. The dose received by the tumour must be maximized and the dose received by vital organs and neighbouring healthy tissue must be minimized. The water content, density, and bulk modulus of thermally cycled polyvinyl alcohol (PVA) hydrogels are similar to those of biological tissue, giving them a proton density suitable for magnetic resonance imaging (MRI) phantoms and a speed of sound suitable for ultrasound phantoms [4, 5].

Assisted by the author, Tamie Poepping's ultrasonics group at The University of Western Ontario, Canada produced PVA hydrogel ultrasound phantoms for field-interaction measurements. The moulds used to produce the phantoms are shown in Fig. 2.1. Further, metallic implants and prostheses pose a threat to patient safety and imaging accuracy in MRI and x-ray scanners [6]. The author assisted Prof. Blaine Chronik's magnetic resonance systems development lab with the production of PVA hydrogel MRI phantoms used to measure image artifacts caused by aluminum, stainless steel, and titanium as shown in Fig. 2.2.

Proliferation of radiotherapy techniques for specific medical applications has created demand for specialized dosimeters which can be used to verify the dose of photons, neutrons, or ions. Radiation-sensitive polymer gels provide a method for three-dimensional dose verification.

Boron neutron capture therapy (BNCT) is an experimental treatment for head and neck cancers. Boron-10 is tagged with a chemical that preferentially binds to tumour cells and injected into a patient. The patient is irradiated with neutrons which react with the boron and produce lithium-7 nuclei and alpha particles which are intended to kill nearby cancer cells. Methacrylic and ascorbic acid in gelatin initiated by copper (MAGIC) gels may be used as dosimeters for BNCT. A hydrogel gel phantom put into the neutron beam in place of the patient is irradiated and dose is determined by measuring the decay rate of transverse relaxation with magnetic resonance imaging (MRI) [7].



Figure 2.1: Moulds used to produce PVA hydrogel ultrasound phantoms for Prof. Tamie Poepping’s ultrasonics group at The University of Western Ontario, Canada.

Intensity-Modulated Radiation Therapy (IMRT) is a promising radiotherapy technique that provides higher precision than older radiotherapy techniques. Treatment of tumours near the spinal cord or vital organs is often deemed too dangerous, but IMRT may allow treatment in some of these cases. PVA hydrogels containing ferrous sulfate are suitable for measuring gamma irradiation from IMRT and dose may be measured using MRI or spectrophotometry on the irradiated gel [8].

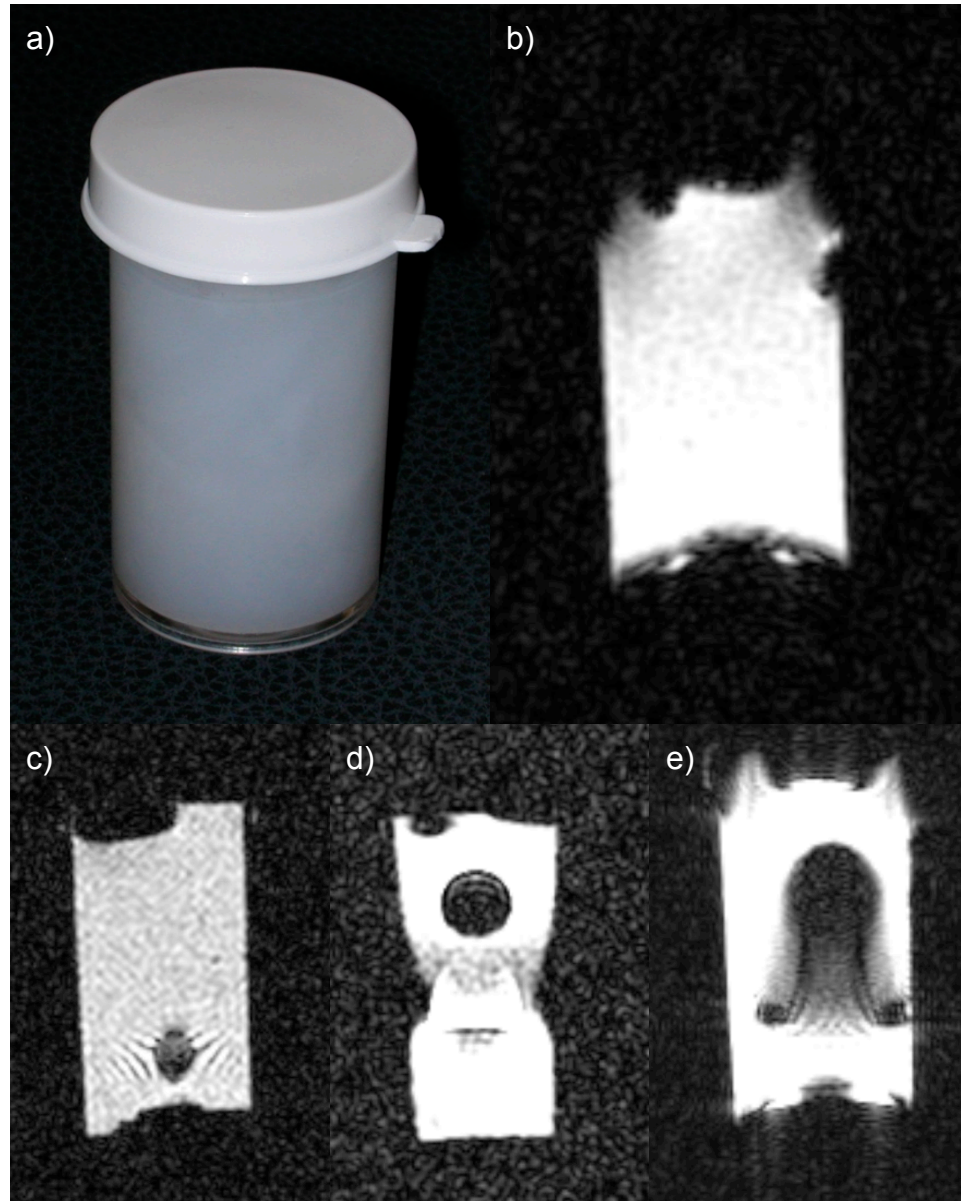


Figure 2.2: PVA hydrogel MRI phantoms used to measure image artifacts caused by metals commonly used in implants and prostheses. The top row shows a) a photograph and b) a MRI image of a reference phantom without metal. The bottom row shows MRI images of phantoms containing c) aluminum, d) stainless steel, and e) titanium. MRI images courtesy of the B. A. Chronik group, The University of Western Ontario, Canada.

Drug Delivery

An ideal drug delivery system will deliver a drug at a predictable rate for a known length of time. Further, the rate of drug release should remain in the therapeutic range for as long as possible. A release rate that is too high can be toxic and one that is too low will be ineffective. Polymer hydrogels are useful because the polymer, the molecular weight, the degree of cross-linking, the porosity and, and the connectivity of pores can all be modified to select the desired diffusive properties. Many biocompatible hydrogels with suitable diffusive properties are already used in commercial drug delivery products. These include topical, oral, injectable, implantable, anal, and vaginal drug delivery systems [9].

Wound Healing and Tissue Repair

Hydrogels are used for reasons other than their desirable diffusive properties. One example is a wound dressing material. Hydrogel wound dressings have high water content and can keep a wound moist for a long time. Their flexibility allows them to stay firmly in contact with the wound, preventing bacteria from reaching the wound. Further, the aqueous component may be loaded with dissolved antibiotics and growth factors that that will prevent infection and speed healing and they can be made with diffusive properties suitable for nearly uniform release of the drugs to the wound over time [9–11].

Hydrogels are also capable of acting as cell scaffolds for tissue regeneration. They may contain live cells in addition to the growth factors used in wound dressings. To repair internal tissues, injectable cell scaffolds are desirable. Numerous injectable hydrogels, which are designed to cross-link after injection via either chemical or physical bonds, have been developed [3, 12]. Some injectable hydrogel precursors begin to gel immediately after preparation, while others only gel in response to a change in pH or temperature after injection [3].

Tissue Augmentation and Replacement

In a few cases, hydrogels are used to augment healthy tissue. For example, silicone hydrogels are used to make commercially available contact lenses. They are desirable because they provide moisture to prevent the eye from drying, they allow oxygen to permeate through the lens to the eye, they can be machined and polished into the desired shape, and they are reasonably durable [13–15]. Hydrogels may even be used to replace damaged tissue when repair is not possible. Substantial progress has been made towards producing artificial cartilage which has compressive behaviour, durability, and lubrication similar to, or better than, natural cartilage [16–19].

The thermally cycled PVA hydrogel introduced in Chapter 1 shows promise for use as heart-valves when reinforced with bacterial cellulose (BC) fibres [20]. Recently, the dynamics of a PVA-BC hydrogel trileaflet aortic heart valve were simulated using the finite element method [21]. The simulated valve was found to behave very similarly to a natural heart valve imaged with ultrasound at various stages of opening, as shown in Fig. 2.3. A strong understanding of the structure of PVA hydrogels and the relationship between structure and bulk mechanical properties will aid the development of prostheses such as heart valves and aortic stents.

The structure of isotropic freeze-thaw PVA hydrogels has been studied by a variety of techniques including neutron scattering, solid-state nuclear magnetic resonance, and confocal laser scanning microscopy [22, 23]. Prior to the work presented here in Chapter 3, only one study has looked at the structure of anisotropic PVA hydrogels. Millon *et al.* performed small-angle neutron scattering (SANS) on anisotropic PVA hydrogels and determined that anisotropy was not due to structural changes at the scale of tens of nanometres, but must be due to changes at scales larger than 100 nanometres [24]. Much remains to be learned about the structure of PVA hydrogels and its relationship to bulk elastic properties.

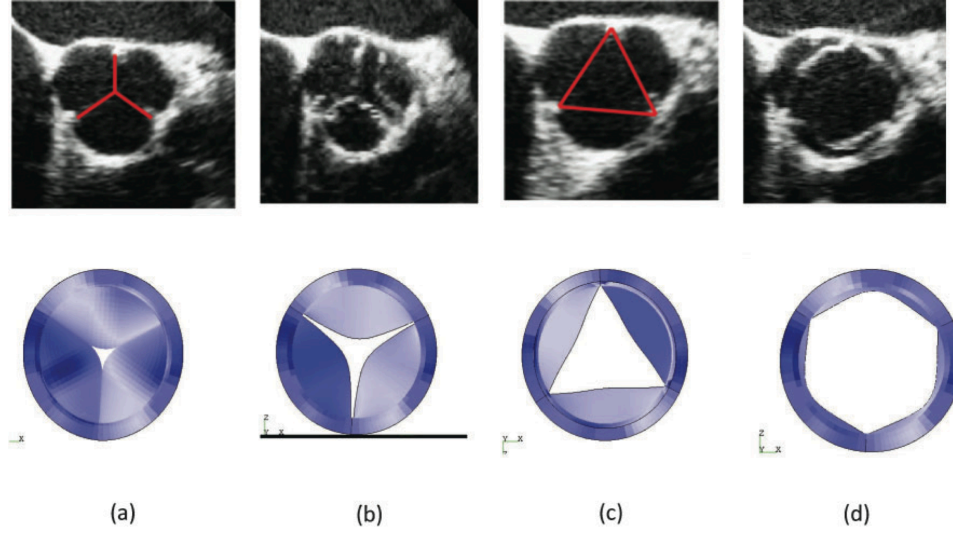


Figure 2.3: Comparison of the finite element method results and the ultrasound images in support of the simulation in the opening phase: (a) the initial state of opening phase; (b) the boomerang shape of the free edges at the beginning of the opening phase; (c) the triangular shape of the free edges; (d) the hexagonal shape of the free edges which closely match the ultrasound images. Reproduced from Mohammadi *et al.* [21] with permission from Sage Publications.

2.2 Neutron Scattering

The neutron was predicted by Rutherford and reported by Chadwick in 1932. It has a mass of approximately $m_n = 1.67 \times 10^{-27}$ kg and a magnetic moment, but does not have electric charge and its electric dipole moment is zero or negligibly small. As a result, neutrons interact with the nuclei of atoms via the short-ranged nuclear force or dipole-dipole interactions and do not interact significantly with electrons.

A thermal neutron is a neutron in equilibrium with room temperature surroundings. From the equipartition theorem, we expect it to have, on average, a kinetic energy K of

$$K = \frac{3}{2}k_B T \approx 6 \times 10^{-21} \text{ J} \approx 40 \text{ meV}$$

where $k_B = 1.38 \times 10^{-23}$ J/K is Boltzmann's constant and T is the temperature. At this energy, the magnitude of the neutron's velocity is

$$v = \sqrt{\frac{2K}{m_n}} \approx 2700 \text{ m/s.}$$

The de Broglie wavelength of this thermal neutron, given by $\lambda = h/mv$, is 1.5 Å and is the same order of magnitude as the interatomic spacings in crystals. Therefore, thermal neutrons are good probes of structure at atomic scales.

Since the range of the nuclear force is small compared to the de Broglie wavelength of the neutron, nuclei behave as point scatterers and neutrons scatter isotropically. The ease with which neutrons scatter varies by nuclear species and depends on the cross-section, σ_s , of the nuclei which can be thought of as the effective area presented by the nucleus to the passing neutron. The cross-section is typically measured in barns where 1 barn = 10^{-28} m².

Neutron scattering is ideal for studying opaque hydrogels. Such hydrogels cannot be studied with light scattering, which requires high transmittance. Further, typical hydrogels made with organic molecules are difficult to study with x-ray scattering because their low atomic-number atoms provide low electron densities and poor electron density contrast. Another advantage of neutron scattering is that hydrogen and deuterium nuclei have significantly different scattering cross-sections, so the contrast of scattering cross-sections can be controlled by varying the ratio of hydrogen to deuterium in a sample. In hydrogels, contrast between the cross-linked network we wish to investigate and the surrounding fluid is easily achieved by substituting heavy water for regular water.

Structure is investigated using neutron scattering by measuring the differential scattering cross-section with a detector and finding a structural model whose calculated differential scattering cross-section best matches the observed scattering. The scattering cross-section is calculated from the total number of neutrons scattered per second divided by the total number of incident neutrons arriving per second. The differential scattering cross-

section, $d\sigma_s/d\Omega$, is the total number of neutrons scattered per second into the small solid angle $d\Omega$, also scaled by the incident neutron rate.

2.2.1 Scattering Theory

Scattered Intensity

Numerous textbooks on scattering theory are available and the notation can vary significantly, especially between the x-ray and neutron scattering disciplines. The derivations and notation used here are based on the clearly presented work of R.-J. Roe [25].

Neutrons of wavelength λ travelling in the positive x direction can be considered as plane waves described by

$$A(x, t) = A_0 e^{i2\pi(\nu t - x/\lambda)} \quad (2.1)$$

where A_0 is the amplitude and ν is the linear frequency. We now consider an incident wave which scatters from a pair of identical nuclei, M and P, as shown in Fig. 2.4. The vector \mathbf{r}

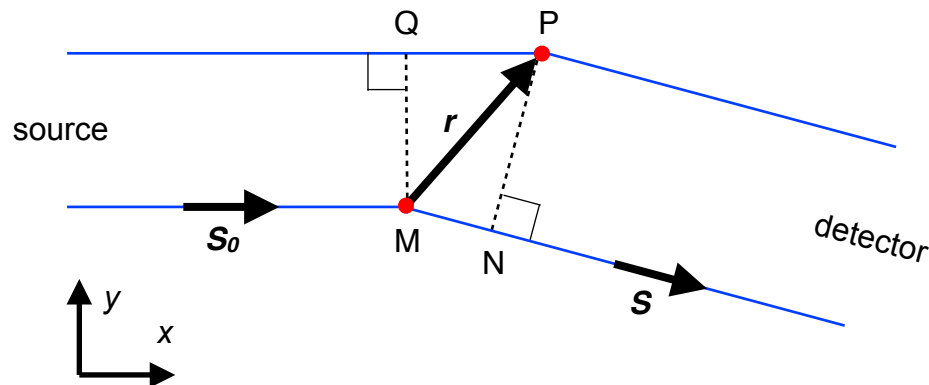


Figure 2.4: Incident wave of neutrons scattered towards a detector by the nuclei located at positions M and P.

defines the position of nucleus P with respect to nucleus M and unit vectors \mathbf{S}_0 and \mathbf{S} define the directions of the incident and scattered waves, respectively. Here, and in Chapters 3

and 4, we only consider elastic scattering. In this case, the wavelength is constant and the phase difference between two waves scattered from nuclei M and P is

$$\Delta\phi = \frac{2\pi}{\lambda} (QP - MN) \quad (2.2)$$

where $QP - MN$ is the path length difference between the two waves. Using vector projections, we may rewrite Eq. 2.2 as

$$\Delta\phi = \frac{2\pi}{\lambda} (\mathbf{S}_0 \cdot \mathbf{r} - \mathbf{S} \cdot \mathbf{r}). \quad (2.3)$$

We define a scattering vector

$$\mathbf{s} = \frac{\mathbf{S} - \mathbf{S}_0}{\lambda} \quad (2.4)$$

which, when substituted into Eq. 2.3 yields

$$\Delta\phi = -2\pi\mathbf{s} \cdot \mathbf{r}. \quad (2.5)$$

An alternative definition of the scattering vector,

$$\mathbf{q} = 2\pi\mathbf{s}, \quad (2.6)$$

is commonly found in the neutron scattering literature and will be used below and in Chapters 3 and 4. Customarily, the scattering angle is defined to be 2θ . The definition of the scattering vector and the scattering angle are shown in Fig. 2.5.

With these definitions, and recalling that \mathbf{S}_0 and \mathbf{S} are unit vectors, the magnitude of the scattering vector is

$$q = 2\pi s = \frac{4\pi}{\lambda} \sin \theta. \quad (2.7)$$

We now endeavour to determine the sum of the waves scattered from nuclei M and P at

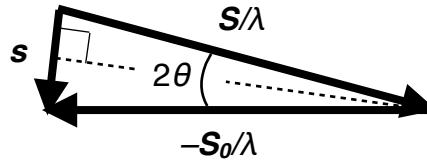


Figure 2.5: Illustration of the scattering vector defined by Eq. 2.4 and the scattering vector 2θ .

the detector. The spherical wave scattered by nucleus P is

$$A_P(x, t) = A_0 b e^{i2\pi(\nu t - x/\lambda)} \quad (2.8)$$

where b is called the scattering length of the nucleus. Since nuclei M and P are identical, the wave scattered from nucleus M differs only in phase by the amount given by Eqs. 2.5 and 2.6, and has amplitude

$$\begin{aligned} A_M(x, t) &= A_0 b e^{i2\pi(\nu t - x/\lambda)} e^{i\Delta\phi} \\ &= A_0 b e^{i2\pi(\nu t - x/\lambda)} e^{-i\mathbf{q} \cdot \mathbf{r}}. \end{aligned} \quad (2.9)$$

The sum of the amplitudes at the detector, $A(x, t)$, is

$$\begin{aligned} A(x, t) &= A_P(x, t) + A_M(x, t) \\ &= A_0 b e^{i2\pi(\nu t - x/\lambda)} (1 + e^{-i\mathbf{q} \cdot \mathbf{r}}). \end{aligned}$$

The intensity or flux of neutrons detected is given by

$$\begin{aligned}
 J &= |A|^2 \\
 &= A(x, t)A^*(x, t) \\
 &= A_0^2 b^2 (1 + e^{-iq \cdot r})(1 + e^{iq \cdot r}).
 \end{aligned}$$

The factors dependent on time and position have cancelled out and do not need to be considered hereafter. We redefine the amplitude with only the phase component as

$$A(\mathbf{q}) = A_0 b (1 + e^{-iq \cdot r}).$$

If we consider a collection of N identical scatterers at positions \mathbf{r}_j , the total amplitude becomes

$$A(\mathbf{q}) = A_0 b \sum_{j=1}^N e^{-iq \cdot \mathbf{r}_j}. \quad (2.10)$$

It is often convenient to treat a sample as a continuous substance with a scatterer number density of $n(\mathbf{r})$ at position \mathbf{r} . Using this definition, the number of scatterers in a volume $d\mathbf{r}$ located at position \mathbf{r} is $n(\mathbf{r})d\mathbf{r}$ and Eq. 2.10 may be written as

$$A(\mathbf{q}) = A_0 b \int_V n(\mathbf{r}) e^{-iq \cdot \mathbf{r}} d\mathbf{r}$$

where V is the volume of sample material exposed to the incident neutron beam. We identify the scattered amplitude as being the Fourier transform of the number density of scatterers. For a material comprised of more than one species of nuclei, the scattering length b will vary with position. By defining a scattering length density distribution $\rho(\mathbf{r}) = b(\mathbf{r})n(\mathbf{r})$, the scattered amplitude becomes

$$A(\mathbf{q}) = A_0 \int_V \rho(\mathbf{r}) e^{-iq \cdot \mathbf{r}} d\mathbf{r}. \quad (2.11)$$

Finally, the intensity normalized to the amplitude of the incident wave A_0 is

$$\begin{aligned} I(\mathbf{q}) &= \frac{1}{A_0^2} A(\mathbf{q}) A^*(\mathbf{q}) \\ &= \left| \int_V \rho(\mathbf{r}) e^{-i\mathbf{q} \cdot \mathbf{r}} d\mathbf{r} \right|^2. \end{aligned} \quad (2.12)$$

Since we detect only the magnitude squared of the amplitudes and cannot measure the individual phases of scattered waves, we cannot invert Eq. 2.12 to determine the scattering length density $\rho(\mathbf{r})$ from the measured intensity. Therefore, in order to determine structure from neutron scattering, it is necessary to make an educated guess of the scattering length density, make a prediction for the scattered intensity, and compare the predicted intensity to the measured intensity.

Form Factors and Structure Factors

For particulate samples, it is advantageous to calculate the scattered intensity from a single particle before calculating the scattered intensity from an ensemble of particles. The scattering from a single particle is called a form factor. As an example, consider a sphere of radius R with uniform scattering length density ρ_0 . Rewriting Eq. 2.11 in spherical coordinates, the amplitude of scattering from the sphere is

$$A(\mathbf{q}) = \rho_0 \int_{\Phi=0}^{2\pi} \int_{\Theta=0}^{\pi} \int_{r=0}^R e^{-i\mathbf{q} \cdot \mathbf{r}} r^2 \sin \Theta dr d\Theta d\Phi.$$

Choosing \mathbf{q} to be aligned along the z axis, $\mathbf{q} \cdot \mathbf{r} = qr \cos \Theta$ and

$$A(q) = 2\pi\rho_0 \int_{\Theta=0}^{\pi} \int_{r=0}^R e^{-iqr \cos \Theta} r^2 \sin \Theta dr d\Theta.$$

If we let $u = \cos \Theta$,

$$\begin{aligned}
 A(q) &= 2\pi\rho_0 \int_{u=-1}^1 \int_{r=0}^R e^{-iqr u} r^2 dr du \\
 &= 2\pi\rho_0 \int_{r=0}^R \frac{e^{-iqr} - e^{iqr}}{-iqr} r^2 dr \\
 &= 2\pi\rho_0 \int_{r=0}^R \frac{e^{iqr} - e^{-iqr}}{iqr} r^2 dr \\
 &= 4\pi\rho_0 \int_{r=0}^R \frac{\sin(qr)}{qr} r^2 dr.
 \end{aligned}$$

Integration by parts yields

$$A(q) = 3\rho_0 v \frac{\sin(qR) - qR \cos(qR)}{(qR)^3}$$

where v is the volume of the sphere. The form factor, or scattered intensity from one particle, is

$$P(q) = |A(q)|^2 = 9\rho_0^2 v^2 \frac{[\sin(qR) - qR \cos(qR)]^2}{(qR)^6}.$$

Once the scattering from a single particle is known, the scattering from a sample comprised of many particles may be found. If the sample is dilute and the positions of particles are uncorrelated, the scattering from the sample is simply the number of particles exposed to the incident neutron beam multiplied by the form factor of a single particle.

However, if the sample is not dilute and there is correlation between the positions of the particles, interference of the waves scattered from individual particles must be taken into account. The preferred method is to find a function $f(\mathbf{r})$ such that the scattering length density of the sample, $\rho(\mathbf{r})$, can be expressed as the convolution of the scattering length density of a single particle, $\rho_1(\mathbf{r})$, with the function f :

$$\rho(\mathbf{r}) = \rho_1(\mathbf{r}) * f(\mathbf{r}).$$

The Fourier transform of the convolution of two functions is the product of the individual Fourier transforms of the functions. Therefore,

$$A(\mathbf{q}) = P(\mathbf{q})S(\mathbf{q})$$

where the form factor $P(\mathbf{q})$ is the Fourier transform of $\rho_1(\mathbf{r})$ and $S(\mathbf{q})$, the Fourier transform of $f(\mathbf{r})$, is called the structure factor.

2.2.2 Small-Angle Neutron Scattering

Small-angle neutron scattering (SANS) provides information on structure at length-scales of nanometres to hundreds of nanometres. Neutrons may be obtained from a spallation source or from a fission reactor. In a typical instrument with a fission reactor neutron source, neutrons are collimated in a neutron guide, passed through a velocity selector, and further collimated before reaching a sample. The velocity selector truncates the distribution of velocities to a narrow range about the chosen mean velocity. After scattering from a sample, the neutrons enter a vacuum chamber and travel several meters to a detector containing ^3He gas. ^3He gas has a high absorption cross-section for thermal neutrons. Upon absorption, the helium nucleus and neutron become ^3H and a proton which can be detected in a proportional counter. To make efficient use of neutrons, an area detector is commonly used to detect neutrons scattered at different angles simultaneously. A schematic diagram of the NG-3 SANS instrument used in Chapter 3 is shown in Fig. 2.6 [26].

2.2.3 Ultra Small-Angle Neutron Scattering

The smallest angle a SANS instrument can measure is limited by its ability to differentiate scattered neutrons from unscattered neutrons. To achieve smaller angles, the neutron beam must be collimated to smaller cross-sectional areas and the detector must be moved farther from the sample. In addition, spread of neutron wavelengths must be decreased by further

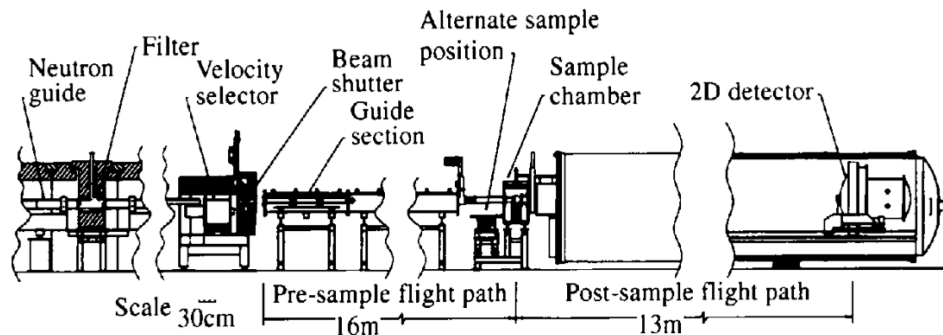


Figure 2.6: A schematic diagram of the NG-3 30 m SANS instrument located at the NIST, Gaithersburg, Maryland, USA. Reproduced from Glinka *et al.* [26] with permission from the International Union of Crystallography.

reducing the range of neutron velocities. Reduced neutron flux, due to increased collimation and reduced velocity spread, and space requirements make this approach impractical.

Double-crystal ultra small-angle neutron scattering (USANS) diffractometers such as the BT-5 instrument at the NIST offer a better solution [27]. A schematic diagram of the BT-5 instrument is provided by Fig. 2.7. Reflection of neutrons from a pair of perfect crystals (the monochromator) provide a nearly monochromatic neutron beam because only the neutrons meeting the Bragg condition pass through the instrument. The beam scatters from the sample to another pair of perfect crystals called an analyzer. Only neutrons meeting the Bragg condition of the analyzer are reflected to the detector. The sensitivity of Bragg reflection to the incident angle of neutrons allows the instrument to measure the differential scattering cross-section with higher angular resolution and at smaller angles than is possible in the SANS instrument described above.

2.3 Atomic Force Microscopy

The atomic force microscope was invented in 1986 by Binnig, Gerber, and Quate [28]. By measuring extremely small deflections of a cantilever beam with a small effective spring constant, the inventors suggested that forces as small as 10^{-18} N could be measured. In

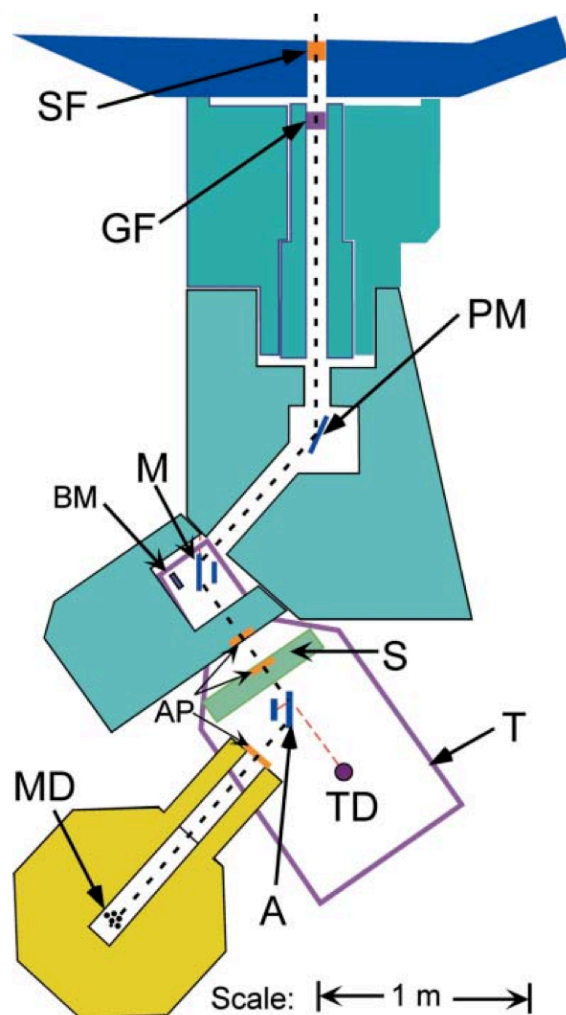


Figure 2.7: A schematic layout of the BT-5 perfect crystal diffractometer located at the NIST, Gaithersburg, Maryland, USA. The dashed line indicates the beam path. The main instrument components are: sapphire filter (SF), pyrolytic graphite filter (GF), graphite premonochromator (PM), silicon monochromator (M), beam monitor (BM), sample changer (S), silicon analyzer (A), transmission detector (TD), vibration isolation table (T), beam apertures (AP), and the main detector (MD). Both MD and A are mounted on precision slides, allowing placement of large ancillary equipment on a hidden sample table. Reproduced from Barker *et al.* [27] with permission from the International Union of Crystallography.

practice, thermal noise limits the force resolution to values larger than 10^{-18} N [29, 30]. The original atomic force microscope proposed by Binnig *et al.* used a scanning tunnelling microscope to measure the deflection of its cantilever while a modern atomic force microscope measures deflections by detecting the displacement of a beam of laser light reflected from the end of its cantilever, as illustrated in Fig. 2.8. A typical multipurpose atomic force microscope can acquire force measurements with piconewton resolution.

In its most basic mode of operation, contact imaging, a cantilever with a sharp tip is brought into contact with a sample positioned on top of a piezoelectric scanner. The sample is raster scanned line-by-line over a rectangular area under the cantilever tip with the scanner. Cantilever deflections are measured as a difference in voltage between the top and bottom halves of a photodetector. A proportional-integral controller adjusts the height of the sample to maintain a constant cantilever deflection. By recording the vertical position of the piezoelectric scanner as a function of the horizontal coordinates, a topographical map of the sample is constructed. Unlike scanning tunnelling microscopy (STM), atomic force microscopy (AFM) may be used to image both conducting and insulating materials, in a variety of environments.

Sometimes, as is done in Chapter 5, AFM is used to make force measurements. Force measurements may be repeated at a single location or performed at many locations over an area to construct a so-called force volume image. During each force measurement, the sample is moved up and down under the cantilever, bringing it in and out of contact with the tip of the cantilever, and the cantilever deflection is recorded as a function of the scanner's vertical position. The deflection of the cantilever is converted to force by multiplying by the effective spring constant of the cantilever. Additionally, deformations of the sample can be found by subtracting the cantilever displacement from the vertical displacement of the scanner, allowing measurement of the mechanical properties of a variety of samples [31].

AFM has been used to determine the mechanical properties of nanofibres, nanowires, and nanotubes such as bacterial cellulose[32], carbon nanotubes [33, 34], gold and silicon

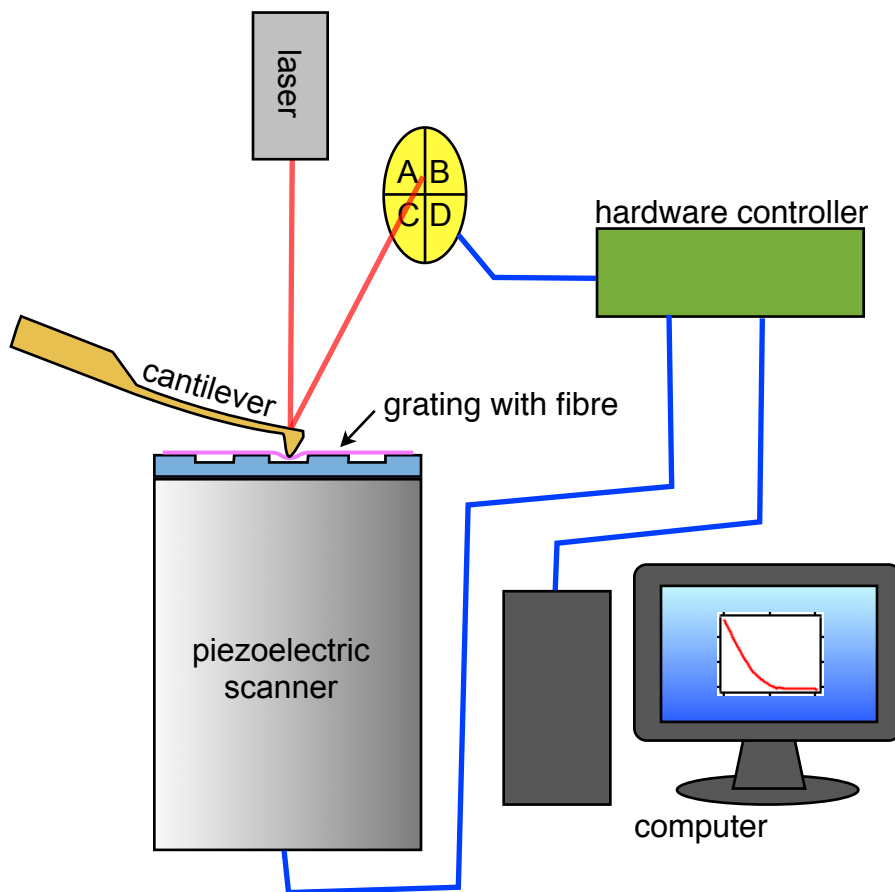


Figure 2.8: Schematic of an atomic force microscope. A piezoelectric scanner moves a mounted sample both horizontally and vertically beneath a mounted cantilever. Forces between the tip of the cantilever and the sample cause the cantilever to deflect. A laser beam, reflected from the end of the cantilever to a four-part area detector, allows vertical deflection to be recorded via the voltage signal $(A+B)-(C+D)$ and torsion via the signal $(A+C)-(B+D)$. A computer sends instructions to a hardware control unit and receives and records force imaging data.

nanowires [35], silicon dioxide nanowires [36], and zinc oxide nanowires [37]. In addition to measuring mechanical properties, AFM can measure magnetic force, friction, protein folding, and receptor-ligand interactions [31].

2.4 Equilibrium of Beams and Fibres

When external forces, bending moments, or distributed loads act on a beam, the beam will deform to a new equilibrium shape for which internal stresses balance the external stresses. Consider a straight beam made of a linearly elastic material with no external stresses which is parallel to the x axis when in equilibrium. Upon application of external stresses which cause the beam to bend to a new equilibrium configuration, small elements of the beam can be described by their position in x and y and their radius of curvature R as shown in Fig. 2.9. The arc length, ds , of the element is

$$ds = R d\theta$$

and the curvature, κ , of the element is

$$\kappa = \frac{1}{R} = \frac{d\theta}{ds}. \quad (2.13)$$

The slope of the element is

$$\frac{dy}{dx} = \tan \theta. \quad (2.14)$$

We now consider only very small deflections, such that that $\theta \ll 1$, with the goal of solving for the beam displacement $y(x)$ in terms of external forces, bending moments, and distributed loads. In the limit of very small deflections, $ds \approx dx$ and $\tan \theta \approx \theta$. Equa-

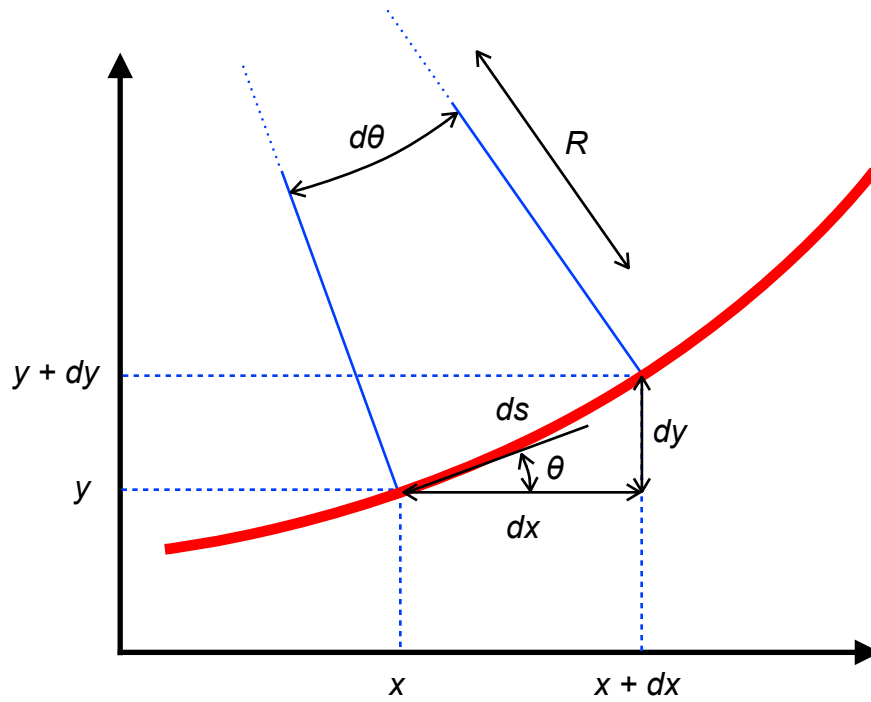


Figure 2.9: Small element of a deflected beam or fibre. The element has length $ds = R d\theta$ where R is the radius of curvature of the element.

tions 2.13 and 2.14 may be rewritten as

$$\kappa = \frac{1}{R} \approx \frac{d\theta}{dx} \quad (2.15)$$

and

$$\frac{dy}{dx} \approx \theta, \quad (2.16)$$

respectively. Substitution of θ from Eq. 2.16 into Eq. 2.15 yields

$$\kappa \approx \frac{d^2y}{dx^2}. \quad (2.17)$$

2.4.1 Bending Moments

We first consider the effect of bending moments M on the beam element in Fig. 2.10. The moments induce stresses which compress and stretch the material above and below a

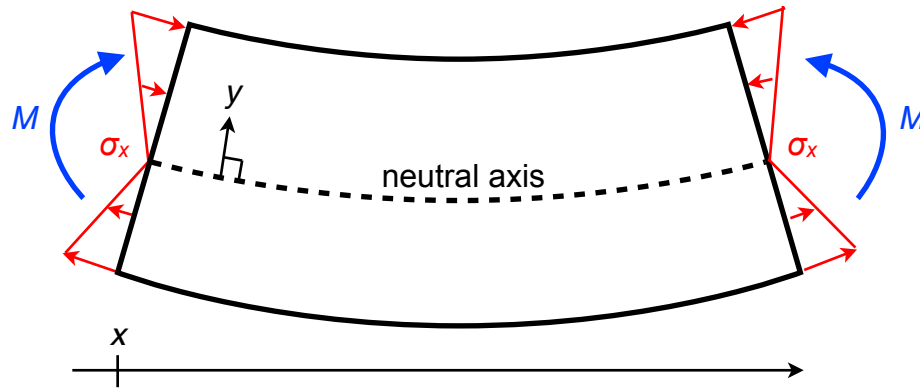


Figure 2.10: Small element of a beam bent by bending moments M at each end. The beam has a neutral axis whose length is unchanged by the moments. The bending moments create stresses which compress the material above the neutral axis and stretch the material below the neutral axis.

neutral axis whose length remains unchanged. Here, y is the position across the diameter of the fibre, measured with respect to the neutral axis. Before deformation, the length of the element is dx at all positions y within the element. After deformation, the length of the element varies vertically, becoming shorter where the material is compressed and longer where the material is stretched. The length at position y equals the arc length at position y and is given by $ds = (R - y)d\theta$ since $R - y$ is the radius of curvature at position y . The strain in the x direction is

$$\begin{aligned}\epsilon_x &= \frac{ds - dx}{dx} \\ &= \frac{(R - y)d\theta - dx}{dx}.\end{aligned}$$

Assuming small deformations, Eq. 2.15 applies and

$$\begin{aligned}\epsilon_x &= \frac{(R-y)\frac{dx}{R} - dx}{dx} \\ &= \frac{R}{R} - \frac{y}{R} - 1 \\ &= -\frac{y}{R}.\end{aligned}\tag{2.18}$$

The stress in the x direction is

$$\begin{aligned}\sigma_x &= E\epsilon_x \\ &= -\frac{Ey}{R} = -E\kappa y\end{aligned}\tag{2.19}$$

where E is the Young's modulus of the material.

There is no net force acting on the ends of the beam element, so the stress must satisfy

$$\int_A \sigma_x dA = 0\tag{2.20}$$

where A is the cross-sectional area of the beam. For symmetric cross-sections such as rectangles and circles, Eq. 2.20 requires that the neutral axis passes through the centre of the beam.

In order to relate the stress σ_x to the bending moment M , we recognize that the moment acts to rotate the end of the fibre about the axis defined by the intersection of the cross-section and the neutral axis. The elemental bending moment dM acting on area element dA located at position y above or below the neutral axis is

$$dM = -\sigma_x y dA.$$

Integration over the entire cross-sectional area A yields the total bending moment

$$M = - \int_A \sigma_x y dA.$$

Upon substitution of Eq. 2.19,

$$\begin{aligned} M &= \frac{E}{R} \int_A y^2 dA \\ &= \frac{EI}{R} \end{aligned} \quad (2.21)$$

where we have defined the area moment of inertia

$$I = \int_A y^2 dA \quad (2.22)$$

which depends on the shape of the beam's cross-section. We rearrange Eq. 2.21 as

$$\kappa = \frac{1}{R} = \frac{M}{EI},$$

equate the result with Eq. 2.17, and obtain

$$\frac{d^2 y}{dx^2} \approx \frac{M}{EI}. \quad (2.23)$$

The equilibrium shape of a beam deformed by moment M acting on its ends may be found from Eq. 2.23, provided that the deformation remains small.

2.4.2 Shear Forces and Distributed Loads

In the final case, we consider a small beam element subjected to moments M , shear forces V , and a distributed load q (force per unit length) as shown in Fig. 2.11. The moments and shear forces may differ between the left and right edges due to stresses internal to the

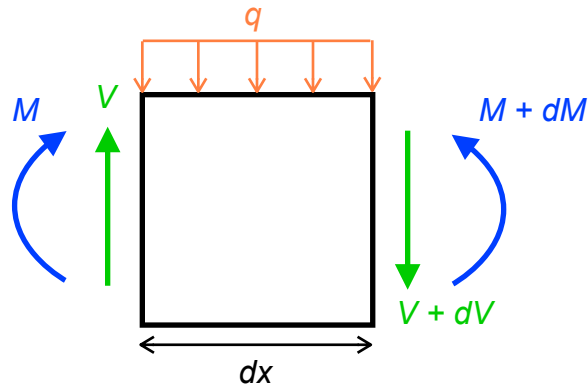


Figure 2.11: Illustration, used for finding equilibrium of torques and forces, of bending moments M and $M + dM$ (blue), shear forces V and $V + dV$ (green) and a distributed load q (orange) acting on a small element of a beam or fibre.

element. In order for the element to be in equilibrium, the sum of forces acting in the vertical direction must be zero and the sum of moments acting about a rotation axis in the element must be zero. Taking the up direction as positive, the sum of vertical forces is

$$V - qdx - (V + dV) = 0$$

$$qdx + dV = 0$$

or

$$\frac{dV}{dx} = -q. \quad (2.24)$$

If clockwise moments are positive, the sum of the moments acting on a rotation axis on the left hand edge is

$$M + qdx\left(\frac{dx}{2}\right) + (V + dV)dx - (M + dM) = 0.$$

In the limit that dx goes to zero, dV and dM also go to zero. Therefore, products of differentials may be discarded. The remaining terms are

$$M + Vdx - M - dM = 0$$

or

$$\frac{dM}{dx} = V. \quad (2.25)$$

Differentiation of Eq. 2.23 and substitution of Eq. 2.25 yields

$$V = \frac{d}{dx} \left(EI \frac{d^2 y}{dx^2} \right)$$

or

$$V = EI \frac{d^3 y}{dx^3} \quad (2.26)$$

when both E and I are uniform along the length of the beam. Differentiation of Eq. 2.26 and substitution of Eq. 2.24 yields

$$q = -\frac{d^2}{dx^2} \left(EI \frac{d^2 y}{dx^2} \right)$$

or

$$q = -EI \frac{d^4 y}{dx^4} \quad (2.27)$$

in the case of constant E and I .

In summary, Eqs. 2.23, 2.26, and 2.27 define the equilibrium shape of a beam, fibre, or other structural element subjected to any combination of a distributed load, bending

moments at its ends, and shear forces at its ends, provided that the deflections are small. These equations form the basis for the model used to determine the mechanical properties of silk fibres from AFM measurements in Chapter 5.

2.5 Bibliography for Chapter 2

1. Hoffman, A. S. "Hydrogels for Biomedical Applications." *Ann. N.Y. Acad. Sci.* **944**, 62–73 (2001).
2. Ruel-Gariépy, E. & Leroux, J.-C. "In situ-forming hydrogels—review of temperature-sensitive systems." *Eur. J. Pharm. Biopharm.* **58**, 409–426 (2004).
3. Yu, L. & Ding, J. "Injectable hydrogels as unique biomedical materials." *Chem. Soc. Rev.* **37**, 1473–1481 (2008).
4. Chu, K. C. & Rutt, B. K. "Polyvinyl Alcohol Cryogel: An Ideal Phantom Material for MR Studies of Arterial Flow an Elasticity." *Magn. Reson. Med.* **37**, 314–319 (1997).
5. Surry, K. J. M., Austin, H. J. B., Fenster, A. & Peters, T. M. "Poly(vinyl alcohol) cryogel phantoms for use in ultrasound and MR imaging." *Phys. Med. Biol.* **49**, 5529–5546 (2004).
6. Sullivan, P. K., Smith, J. F. & Rozelle, A. A. "Cranio-Orbital Reconstruction: Safety and Image Quality of Metallic Implants on CT and MRI Scanning." *Plast. Reconstr. Surg.* **94**, 489–596 (1994).
7. Uusi-Simola, J. *et al.* "MAGIC polymer gel for dosimetric verification in boron neutron capture therapy." *Am. Coll. Med. Phys.* **8**, 114–123 (2007).
8. Hill, B. *et al.* "Investigation and analysis of ferrous sulfate polyvinyl alcohol (PVA) gel dosimeter." *Phys. Med. Biol.* **47**, 4233–4246 (2002).
9. Gupta, P., Varmani, K. & Garg, S. "Hydrogels: from controlled release to pH-responsive drug delivery." *Drug Delivery Today* **7**, 569–579 (2002).
10. Varshney, L. "Role of natural polysaccharides in radiation formation of PVA-hydrogel wound dressing." *Nucl. Instr. and Meth. in Phys. Res. B* **255**, 343–349 (2007).
11. Gupta, A., Kumar, R., Upadhyay, N. K., Surekha, P. & Roy, P. K. "Synthesis, Characterization and Efficacy of Chemically Crosslinked PVA Hydrogels for Dermal WoundHealing in Experimental Animals." *J. Appl. Polym. Sci.* **111**, 1400–1408 (2009).
12. Ossipov, D. A., Brännvall, K., Forsberg-Nilsson, K & Hilborn, J. "Formation of the First Injectable Poly(vinyl alcohol) Hydrogel by Mixing of Functional PVA Precursors." *J. Appl. Polym. Sci.* **106**, 60–70 (2007).
13. Ellis, E. J. & Salamone, J. C. *pat.* 4,152,508 (1979).
14. Nandu, M. P., Bawa, R. S. & Lai, Y.-C. *pat.* 5,260,000 (1993).

15. Kunzler, J. F. & Seelye, D. E. *pat.* US 7,268,198 B2 (2007).
16. Suh, J.-K. F. & Matthew, H. W. T. “Application of chitosan-based polysaccharide biomaterials in cartilage tissue engineering: a review.” *Biomaterials* **21**, 2589–2598 (2000).
17. Bodugoz-Senturk, H., Macias, C. E., Kung, J. H. & Muratoglu, O. K. “Poly(vinyl alcohol)–acrylamide hydrogels as load-bearing cartilage substitute.” *Biomaterials* **30**, 489–596 (2009).
18. Chen, M., Briscoe, W. H., Armes, S. P. & Klein, J. “Lubrication at Physiological Pressures by Polyzwitterionic Brushes.” *Science* **323**, 1698–1701 (2009).
19. Ma, R., Xiong, D., Miao, F., Zhang, J. & Peng, Y. “Friction properties of novel PVP/PVA blend hydrogels as artificial cartilage.” *J. Biomed. Mater. Res. A* **93A**, 1016–1019 (2010).
20. Millon, L. E., Guhados, G. & Wan, W. “Anisotropic Polyvinyl Alcohol – Bacterial Cellulose Nanocomposite for Biomedical Applications.” *J. Biomed. Mater. Res. B: Appl. Biomater.* **86B**, 444–452 (2008).
21. Mohammadi, H., Boughner, D., Millon, L. E. & Wan, W. K. “Design and simulation of a poly(vinyl alcohol)bacterial cellulose nanocomposite mechanical aortic heart valve prosthesis.” *P. I. Mech. Eng. H* **223**, 697–711 (2009).
22. Willcox, P. J. *et al.* “Microstructure of Poly(vinyl alcohol) Hydrogels Produced by Freeze/Thaw Cycling.” *J. Polym. Phys.* **37**, 3438–3454 (1999).
23. Fergg, F., Keil, F. J. & Quader, H. “Investigations of the microscopic structure of poly(vinyl alcohol) hydrogels by confocal laser scanning microscopy.” *Colloid. Polym. Sci.* **279**, 61–67 (2001).
24. Millon, L. E., Nieh, M.-P., Hutter, J. L. & Wan, W. “SANS Characterization of an Anisotropic Poly(vinyl alcohol) Hydrogel with Vascular Applications.” *Macromol.* **40**, 3655–3662 (2007).
25. Roe, R.-J. *Methods of X-Ray and Neutron Scattering in Polymer Science* (Oxford University Press, 2000).
26. Glinka, C. J. *et al.* “The 30 m Small-Angle Neutron Scattering Instruments at the National Institute of Standards and Technology.” *J. Appl. Cryst.* **31**, 430–445 (1998).
27. Barker, J. G. *et al.* “Applied Design and performance of a thermal-neutron double-crystal diffractometer for USANS at NIST.” *J. Appl. Cryst.* **38**, 1004–1011 (2005).

28. Binnig, G., Quate, C. F. & Gerber, C. "Atomic Force Microscope." *Physical Review Letters* **56**, 930–933 (1986).
29. Butt, H.-J. & Jaschke, M. "Calculation of thermal noise in atomic force microscopy." *Nanotechnol.* **6**, 1–7 (1995).
30. Gittes, F. & Schmidt, C. F. "Thermal noise limitations on micromechanical experiments." *Eur. Biophys. J.* **27**, 75–81 (1998).
31. Müller, D. J. & Dufrêne, Y. F. "Atomic force microscopy as a multifunctional molecular toolbox in nanobiotechnology." *Nat. Nanotechnol.* **3**, 261–269 (2008).
32. Guhadós, G., Wan, W. & Hutter, J. L. "Measurement of the Elastic Modulus of Single Bacterial Cellulose Fibers Using Atomic Force Microscopy." *Langmuir* **21**, 6642–6646 (2005).
33. Kim, G.-T., Gu, G., Waizmann, U. & Roth, S. "Simple method to prepare individual suspended nanofibers." *Appl. Phys. Lett.* **80**, 1815–1817 (2002).
34. Guhadós, G., Wan, W., Sun, X. & Hutter, J. L. "Simultaneous measurement of Young's and shear moduli of multiwalled carbon nanotubes using atomic force microscopy." *J. Appl. Phys.* **101**, 033514–1–5 (2007).
35. Heidelberg, A. *et al.* "A generalized description of the elastic properties of nanowires." *Nano Lett.* **6**, 1101–1106 (2006).
36. Ni, H., Li, X. & Gao, H. "Elastic modulus of amorphous SiO₂ nanowires." *Appl. Phys. Lett.* **88**, 043108:1–3 (2006).
37. Wen, B., Sader, J. E. & Boland, J. J. "Mechanical Properties of ZnO Nanowires." *Phys. Rev. Lett.* **101**, 175502:1–4 (2008).

Chapter 3

Characterization of Anisotropic Polyvinyl Alcohol Hydrogel by Small- and Ultra Small-Angle Neutron Scattering

3.1 Introduction

Polyvinyl alcohol (PVA) hydrogel is a hydrophilic, biocompatible material that has received recent attention for a variety of applications. For instance, physically cross-linked PVA hydrogels can be tailored to have mechanical properties similar to those of cardiovascular tissue [1–5], raising the possibility of its use in cardiovascular prostheses with a reduced risk of failure due to compliance mismatch [6, 7].

Physically cross-linked PVA hydrogels are formed from PVA solution during freeze/thaw thermal cycling or quenching. The mechanism by which PVA solution gels during thermal

Reprinted with permission from Hudson, S. D. *et al.* “Characterization of anisotropic poly(vinyl alcohol) hydrogel by small- and ultra-small-angle neutron scattering.” *J. Chem. Phys.* **130**, 034903-1–9 (2009). Copyright 2009, American Institute of Physics.

cycling has received much attention [1, 3, 8–10]. The generally accepted model is that cycling to low temperatures causes the formation of ice crystals, which increases the polymer concentration in the surrounding unfrozen regions, inducing PVA crystallization. Using solid-state nuclear magnetic resonance, differential scanning calorimetry, and small-angle X-ray scattering, Willcox *et al.* showed that PVA crystallites of size 3–8 nm and average separation 30 nm form in the concentrated polymer regions. Cryogenic transmission electron microscopy showed that the dense, crystallite-filled regions surround much larger ice crystals where little polymer is found [10].

Recently, an anisotropic PVA hydrogel has been reported in which anisotropy is induced by stretching a weak isotropic gel, formed by a single thermal cycle, and following with further cycling [4]. The authors were able to optimize the stress-strain properties of the anisotropic PVA hydrogel to match those of porcine aorta in the physiological range, raising the possibility of use for cardiovascular tissue replacement. Small-angle neutron scattering (SANS) studies of this anisotropic hydrogel showed that its anisotropic properties were due to structural changes at a scale larger than 100 nm [5].

In this study ultra small-angle neutron scattering (USANS) is used to extend the length-scale probed to approximately 10 μm and to measure a wide range of gels formed by varying the number of thermal cycles and the amount of processing strain. Here a combined SANS and USANS study of thermally cycled anisotropic PVA hydrogels is presented.

3.2 Materials and Methods

3.2.1 Sample Preparation

PVA solutions were prepared by dissolving atactic PVA with an average molecular weight of 146000–186000 (99+% hydrolyzed, Sigma-Aldrich, Canada) in Deuterium Oxide (D_2O) (99.9 atom%, Sigma-Aldrich, Canada) to achieve a D_2O :PVA molar ratio of 21.9:1, closely matching the molar ratio used in previous studies [4, 5], in which H_2O was the solvent. The

solutions were held at 90 °C while stirring for 3 h as reported previously [5] to fully dissolve the PVA. A reflux column and drying tube containing anhydrous calcium sulphate (Drierite, Sigma-Aldrich, Canada) were used to prevent the loss of D₂O and to minimize exchange with H₂O in the air.

Cooled PVA solution was used to fill moulds comprised of 17.8 cm × 17.8 cm plates of aluminum separated by a 1.6 mm thick rubber gasket. The solution was carefully added to the moulds using a syringe to prevent the introduction of air bubbles. Moulds were sealed and submerged in a water bath for thermal cycling. Each cycle consisted of ramping the temperature from 20 °C to −20 °C at 0.1 °C/ min, holding the temperature at −20 °C for 1 h, ramping the temperature back to 20 °C at 0.1 °C/ min, and holding the temperature at 20 °C for 1 h. This cycle was repeated as required.

Anisotropic gels were made by stretching cycle-one gels and securing them in modified aluminum moulds with clamps. The extension required for the desired strain was determined before stretching and measured with a ruler during stretching. Each clamp consisted of a thin aluminum strip that could be screwed, through the gel, into the bottom aluminum plate [5]. Further cycling with this setup resulted in gels with *permanent* anisotropic properties.

3.2.2 Neutron Scattering

Small-angle neutron scattering (SANS) experiments were performed on the NG3 beamline at the National Institute of Standards and Technology (NIST) in Gaithersburg, MD [11]. Three sample-to-detector distance (SDD) and wavelength (λ) combinations were used to cover a scattering vector (q) range from 0.0013–0.3 Å^{−1}, as shown in Table 3.1. The corresponding length-scales $r = 2\pi/q$ range from 2.1–480 nm. At the large scattering angles of the shortest SDD configuration, the geometry of the titanium sample holders caused a reduction in neutron counts at scattering vectors above a magnitude of 0.3 Å^{−1}. For this reason, data above this scattering vector magnitude were not used. At the longest SDD

Table 3.1: NG3 SANS configurations.

SDD (m)	λ (Å)	q (Å ⁻¹)	r (nm)
1.33 ^a	6.0	0.033 – 0.3 ^b	2.1 – 19
5.0 ^a	6.0	0.0099 – 0.11	5.7 – 63
13.19 ^{ac}	8.4	0.0013 – 0.031	20 – 480

^a Detector offset 20 cm from centre to achieve a larger q -range at a particular SDD

^b Maximum q limited by sample cell geometry

^c Lens configuration used to achieve low q

configuration, a focusing lens system consisting of concave MgF₂ lenses was used to provide better low- q resolution and higher flux than could be attained using a conventional pinhole collimation system [12]. Examples of raw data from isotropic and anisotropic gels are shown in Fig. 3.1.

USANS experiments were performed at NIST on the BT5 instrument, which is an ultra-high resolution small-angle neutron scattering double-crystal diffractometer [13]. This instrument collects one dimensional data, so anisotropic samples were run twice: once with the processing strain direction parallel with the measured q -axis, and once with the sample rotated in plane by ninety degrees, i.e., with the processing strain direction perpendicular to the measured q -axis. Neutrons of wavelength 2.38 Å are selected by Bragg reflection from perfect-crystal monochromators and reflected towards the sample. Behind the sample, an analyzer, also consisting of a perfect crystal monochromator, is rotated to reflect scattered neutrons into a detector. Due to the high angular sensitivity of Bragg reflection, only neutrons that are scattered through a very narrow range of angles are diffracted by the analyzer into the detector, providing excellent angular resolution extending to very small angles. By rotating the analyzer to a maximum angle of 0.046 degrees, scattering vectors up to 0.0021 Å⁻¹ and length-scales down to 300 nm were studied, providing overlap with the SANS data.

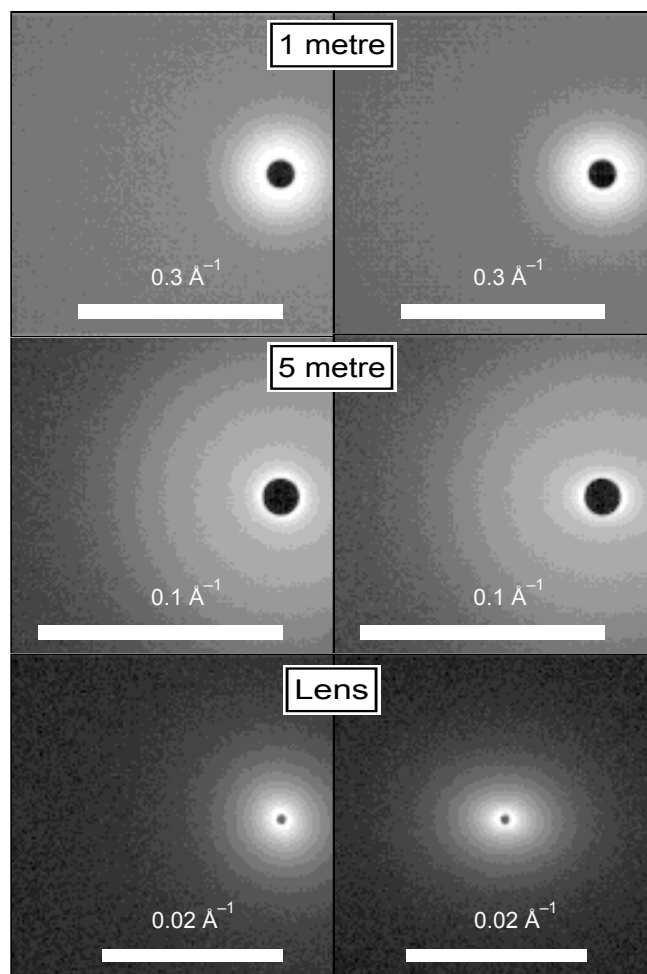


Figure 3.1: Raw SANS data for isotropic (left column) and anisotropic (right column) cycle-six PVA hydrogels using the NG3 configurations shown in Table 3.1. The scale bars indicate the scattering vector, q , with the largest q range occurring at the nearest detector position (1 metre) and the smallest q range occurring at the farthest detector position (lens, 13 metre). The brightness represents the logarithm of the total number of neutrons counted on the detector (arbitrary scale), and is not corrected for background or the contribution of the sample cell. Sixteen grayscale colours have been used in order to show contours of constant neutron counts, elucidating the anisotropy. Note that a beamstop is used to prevent detector damage due to the unscattered beam, resulting in dark spots centred at $q = 0$. The strain induced during cycling for the anisotropic gel was 75%, resulting in an anisotropy that is most obvious at the largest length-scales (smallest q).

Table 3.2: PVA samples produced and scattering techniques used. The number of thermal cycles, N , and the processing strain, ε_0 , used to produce each sample are shown.

N	ε_0	Scattering Techniques
1	0	SANS, USANS
3	0	SANS, USANS
	0.25	SANS
	0.50	SANS
	0.75	SANS, USANS
6	0	SANS, USANS
	0.25	SANS, USANS
	0.50	SANS
	0.75	SANS, USANS

Data were collected for hydrogel samples made with various numbers of thermal cycles and processing strains. However, due to time constraints, not all of the samples studied by SANS could be studied with USANS. Table 3.2 shows the combinations of thermal cycles, N , processing strains, ε_0 , and scattering techniques employed. Priority was given to samples produced with a strain of 0.75, as a cycle-three hydrogel produced with a strain of 0.75 was previously shown to closely match the stress-strain properties of porcine aorta [4]. Isotropic samples were not stretched and are indicated with processing strains of zero. Samples were considered fresh, as they were prepared less than one month before the neutron scattering experiments and it has been previously verified that the mechanical properties of anisotropic PVA hydrogels do not change significantly after aging for thirteen months [5].

3.2.3 Data Reduction

Differential scattering cross-sections ($d\Sigma/d\Omega(\mathbf{q})$) were extracted from the SANS data in Igor Pro (WaveMetrics, Inc., Portland, OR) using routines provided by NIST [14]. Briefly, the data were corrected for background and empty sample cell scattering, divided by the sensitivity of the detector, and converted to absolute scaling in units of cm^{-1} . One-dimensional differential scattering cross-sections were extracted by circularly averaging the isotropic data about the $q = 0$ position. In the case of anisotropic gels, two one-dimensional cross-sections were obtained by sector averaging parallel and perpendicular to the direction of applied strain. An angular width of 45° was chosen for all sector averages because there was negligible difference from 30° sector averages. For each sample, data from the three q -ranges were combined into a single SANS data set spanning a range of $0.0013 < q < 0.3 \text{ \AA}^{-1}$.

USANS data were also reduced using Igor Pro routines provided by NIST [14]. Similar to SANS data reduction, this also involved subtraction of background and empty cell scattering and conversion to absolute scaling. In order to facilitate simultaneous fitting to SANS and USANS data, NIST's implementation [14] of the Lake algorithm [15] was used to deconvolve the smearing due to the finite angular range of neutrons outside of the nominal scattering plane. The Lake algorithm uses an iterative algorithm to deduce what the scattering observed using an infinitesimally small pinhole would be, given the smeared scattering observed using a collimation slit of known dimensions. In practice, unscattered neutrons are detected at very low q -values, creating large background and limiting the maximum length-scale that can be probed. For a few data points at low q , the empty cell scattering counts outnumber the sample scattering counts. After subtraction and absolute scaling, these points show negative scattered intensity. While desmearing, these low q data points with negative intensities were masked. No data smoothing was used prior to desmearing. After desmearing, the remaining noisy points at low q were eliminated, leaving useable data up to approximately 10 \mu m .

3.2.4 Atomic Force Microscopy

A PVA hydrogel was studied using a BioScope II atomic force microscope (Veeco Metrology Inc., Santa Barbara, CA). A cycle-ten hydrogel was imaged because it was stiffer than hydrogels made with fewer thermal cycles, thus allowing higher resolution imaging. NP-S silicon nitride cantilevers with nominal spring constants of 0.06 N/m (Veeco Metrology Inc., Santa Barbara, CA) were used. Imaging was performed in water with unmodified cantilevers and cantilevers modified by 20 μm glass beads (Duke Scientific Corporation, Palo Alto, CA) glued to their ends, using the procedure described in Appendix A, with NOA 81 ultraviolet-curing optical adhesive (Norland Products Inc., New Brunswick, NJ). Modified glass bead tips greatly reduced sample damage and imaging artifacts at the expense of imaging resolution, and were reserved for imaging at the largest scan size where imaging resolution was less important.

3.3 Theory and Data Analysis

Neutron scattering results from variations of the scattering length density in the sample. In PVA hydrogels, there is good contrast between the polymer and solvent, so variation in polymer concentration results in variation in the scattering length density. The goal is to deduce the polymer concentration as a function of position from the scattered neutrons. However, as with most scattering techniques, only the intensity of the scattered waves is measured while the amplitudes and phases of individual scattered waves are unknown, making it impossible to directly deduce the polymer concentration as a function of position. Instead, one generally hypothesizes a structure and compares the predicted scattering to that observed. Care must be taken because a concentration distribution that gives the measured scattering is not unique.

3.3.1 Solution

First, scattering from the solution is considered. By approximating the PVA as freely jointed polymer chains comprised of $n_k = 1530$ links of Kuhn length $b_k = 6.2 \text{ \AA}$, $n_k^{-4/5}/b_k^3$ yields an estimate of the overlap concentration of roughly 0.2% by mass in a good solvent [16–18]. At 10% polymer by mass, the concentration of the PVA solution is well above the overlap concentration but well below 100%. Scattering from a neutral, ungelled polymer solution in this “semi-dilute” regime is expected to exhibit Ornstein-Zernicke (Lorentzian) behaviour described by

$$\left(\frac{d\Sigma}{d\Omega}\right)_{\text{sol}}(q) = \frac{A_{\text{sol}}}{1 + (q\xi_{\text{sol}})^2} + bg \quad (3.1)$$

where A_{sol} is a constant incorporating the osmotic compression modulus, the inherent D₂O–PVA contrast, and the volume fraction; ξ_{sol} is the density-density correlation or screening length [18]; and bg includes background and incoherent scattering.

A fit of Eq. 3.1 to the differential scattering cross-section of the uncycled solution yields a screening length of 2.9 nm and is shown in Fig. 3.2. The model and experimental data closely match, except at low q where the data systematically show higher scattering than the model. Some gelation of the solution is expected to occur as the solution ages, even without freeze/thaw cycling, and is likely responsible for the increase in scattering at low q . The screening length may be estimated from the sum of the contour lengths of polymer per cubic metre of solution. Assuming a molecular weight of 166 kg/mol, the total contour length of polymer per cubic centimetre is approximately 3.4×10^{13} cm, which can be divided into 3.4×10^{13} straight pieces of polymer, each 1 cm in length. These pieces divide the cubic centimetre into a cubic lattice with a lattice spacing of 3 nm. The lattice spacing, which equals the distance between adjacent chains, is in close agreement with the screening length of 2.9 nm.

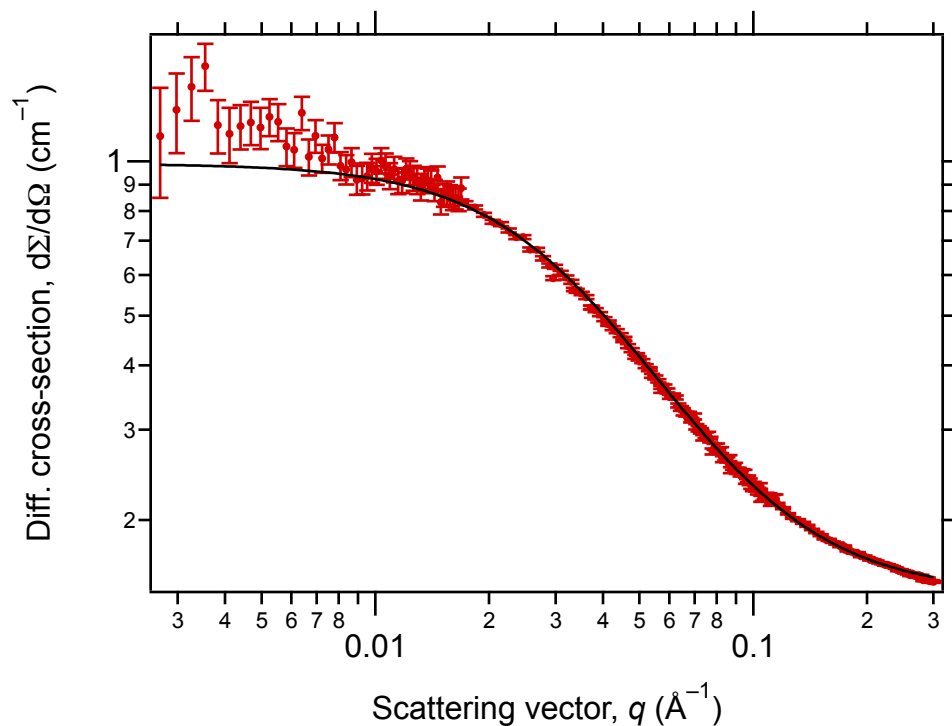


Figure 3.2: Differential scattering cross-section from PVA solution after reduction to an absolute scale and circular averaging. The solid line is the fit to Eq. 3.1.

3.3.2 Hydrogel

When the PVA solution is thermally cycled, PVA crystallites form and act as cross-linking sites [1, 8, 10]. The model for the hydrogel structure is motivated by previous studies that suggest the crystallites are a few nanometers in size and separated by tens of nanometres [5, 10, 19, 20].

The gel is modelled as a combination of polymer that is cross-linked and fixed, and polymer that is free to move [21–25]. This approach has been applied successfully to a variety of chemically cross-linked polymer gels [21, 23, 26], including chemically cross-linked PVA [25] (see [24] for a good review.) This model is referred to as the Horkay-Geissler model.

Scattering from the free polymer, e.g., polymer in solution without cross-links, is still

described by an Ornstein-Zernicke term and will be referred to as free polymer scattering.

Thus

$$\left(\frac{d\Sigma}{d\Omega}\right)_{\text{free}}(q) = \frac{A_{\text{free}}}{1 + (q\xi_{\text{free}})^2} \quad (3.2)$$

where A_{free} and ξ_{free} are expected to differ from the corresponding values in the ungelled solution because the PVA density in regions containing free polymer will be different than the density in the initial solution.

Permanent density fluctuations in cross-linked polymer gels are often described by a Gaussian density correlation function

$$\Gamma_{\rho}(r) \propto \exp\left(-r^2/2\xi_{\text{fixed}}^2\right),$$

resulting in scattering of the form

$$\left(\frac{d\Sigma}{d\Omega}\right)_{\text{fixed}}(q) = A_{\text{fixed}} \exp\left(-q^2\xi_{\text{fixed}}^2/2\right)$$

where ξ_{fixed} is the average size of the fixed density fluctuations and the amplitude A_{fixed} depends on the scattering contrast and concentration [21, 26]. Scattering from other gels, including this one, is better described by the more general and empirical equation

$$\left(\frac{d\Sigma}{d\Omega}\right)_{\text{fixed}}(q) = A_{\text{fixed}} \exp\left[-(q\xi_{\text{fixed}})^b\right] \quad (3.3)$$

where b is a constant that determines how abruptly the density changes with distance [23–25].

While the Horkay-Geissler model [23–25] successfully describes the data at high q , significant excess scattering is seen at low q (Fig. 3.4), which is attributed to scattering from large polymer-poor voids where ice crystals have melted. The polymer structure surrounding the pores is modelled as a network of dense polymer knots or blobs, each of which has an internal structure described by the small-scale gel structure discussed above.

The PVA blobs cannot be considered sparse and non-interacting, so it is necessary to consider interference effects from scattering between the blobs. This is accomplished by modelling the data as the product of a form factor, $P(q)$, that describes the scattering from a single blob, and a structure factor, $S(q)$, that describes the arrangement of all of the blobs and the resulting interference.

The blobs are expected to be irregular and to have a distribution of sizes, but without evidence that indicates what the distribution should be, it is difficult to justify increasing the number of parameters by integrating a basic form factor (e.g., the form factor for a sphere) over a distribution of radii. Instead, a form factor similar to the Debye-Anderson-Brumberger form factor

$$P(q) \propto \frac{1}{[1 + (q\xi)^2]^2} \quad (3.4)$$

that was derived for a randomly distributed phase of correlation length ξ is used [27]. For non-uniform objects that are approximately spherical, ξ is proportional to the average radius of the objects [28]. However, the low- q contribution to the scattering data does not obey the Porod power law ($d\Sigma/d\Omega \propto q^{-4}$) in the high- q limit [29]. For all samples made with three or six thermal cycles, the power law exponent, which can be determined from the slope on a log-log plot, is shallower than -4 , indicating that the interface has a rough or surface fractal structure. The exponent is therefore modified to obtain the form factor [30]

$$P(q) = \frac{A_1}{\left[1 + \frac{D+1}{3} (Rq)^2\right]^{D/2}} \quad (3.5)$$

where R is the average size of the blobs, D is related to the surface fractal dimension d_s by $D = 2(4 - d_s)$, and A_1 is a scattering amplitude. The surface fractal dimension can vary from 2 for a perfectly smooth surface to 3 for a surface with maximum roughness. For this range of d_s , D can vary between 2 and 4.

The USANS and atomic force microscopy (AFM) data (see below) indicate that structures extend to length-scales of at least 10 μm . To capture this behaviour, the mass-fractal

structure factor

$$S(q) = 1 + \frac{D_m \Gamma(D_m - 1)}{(qR)^{D_m}} \left[\left(1 + \frac{1}{(q\xi_1)^2} \right)^{(1-D_m)/2} \times \sin [(D_m - 1) \arctan (q\xi_1)] \right] \quad (3.6)$$

is used where D_m is the mass-fractal dimension, Γ is the gamma function, R is the average blob size from Eq. 3.5, and ξ_1 is the upper limit of the fractal structure [31]. This allows the scattering to roll off as q decreases to values corresponding to the aggregate size ξ_1 .

The complete model for the hydrogel structure is then

$$\frac{d\Sigma}{d\Omega} = P(q)S(q) + \left(\frac{d\Sigma}{d\Omega} \right)_{\text{fixed}} + \left(\frac{d\Sigma}{d\Omega} \right)_{\text{free}} + bg. \quad (3.7)$$

The first term is for scattering from the large structure of PVA blobs, the second term describes the density fluctuations in the blobs due to cross-linking of the polymer molecules, and the free scattering term has been included to determine if there is any remaining free polymer (i.e., polymer that has not been cross-linked). Finally, a constant term has been included to account for background and incoherent scattering, giving a total of eleven parameters. A schematic of the structure showing aggregates, blobs, and the fixed polymer length-scale is shown in Fig. 3.3.

An example fit is shown in Fig. 3.4, in which the full model of Eq. 3.7 is shown with a solid line, and the contributions of individual terms are indicated by dashed lines. Fig. 3.4 also shows the slopes that are determined by the mass and surface fractal dimensions, as well as the transitions between slopes that are determined by the fractal aggregate size and the blob size. Fig. 3.5 shows how the neutron data change with the number of thermal cycles and Fig. 3.6 shows neutron data for an isotropic cycle-six hydrogel, and an anisotropic cycle-six hydrogel produced with a processing strain of 75%.

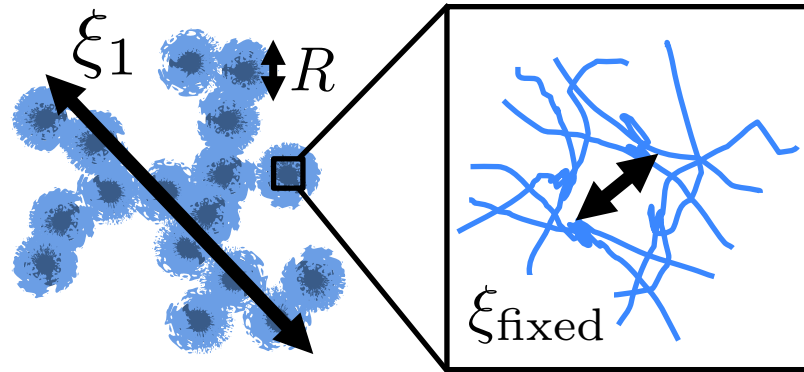


Figure 3.3: Schematic of the structure showing aggregates of size ξ_1 , blobs of size R , and the fixed polymer length-scale ξ_{fixed}

3.3.3 Data Fitting

The blob size R determines where the transition between the slopes of D_m and D occurs. The overlap between USANS and SANS data occurs at approximately the same magnitude of q as this transition, and neither data are sufficient to determine R alone. For this reason, the fitting is performed in two steps. In the first, ξ_1 , D_m , and R are determined by fitting to Eq. 3.7 for samples in which both SANS and USANS data were acquired. In the second, d_s , ξ_{fixed} , b , ξ_{free} , and bg are determined by fitting Eq. 3.7, with the larger scale parameters held constant, for samples in which only SANS data were acquired.

Fractal aggregate sizes determined by fitting combined SANS and USANS data sets to the full model of Eq. 3.7 are shown in Table 3.3. Blob sizes versus number of thermal cycles are shown in Table 3.4 for isotropic and anisotropic gels. While there is a wide variation in parameters, it is clear that for anisotropic gels both R and ξ_1 show a significant difference between the perpendicular and parallel directions. The mass fractal dimension showed no clear trends with the number of thermal cycles or with direction in anisotropic gels and had an average value of 2.2 ± 0.2 . Although the scattering in the limit of $q = 0$ must be the same in both directions, the presence of structures much larger than the length scales accessible by USANS does not permit us to add this constraint to our fitting.

Table 3.3: Fractal aggregate sizes as determined by fitting Eq. 3.7 to combined SANS and USANS data. For anisotropic gels, the initial processing strain was 75% unless noted otherwise.

Aggregate Size, ξ_1 (μm)			
Cycle	Isotropic	Perpendicular	Parallel
1	0.9	—	—
3	~ 10	3.4	> 10
6	2.4	2.9 ^a	$> 10^a$
6		4.3	> 10

^a Processing strain of 25%

Table 3.4: Blob sizes as determined by fitting Eq. 3.7 to combined SANS and USANS data. For anisotropic gels, the initial processing strain was 75% unless noted otherwise.

Blob Size, R (nm)			
Cycle	Isotropic	Perpendicular	Parallel
1	18	—	—
3	51	46	76
6	40	27 ^a	34 ^a
6		29	78

^a Processing strain of 25%

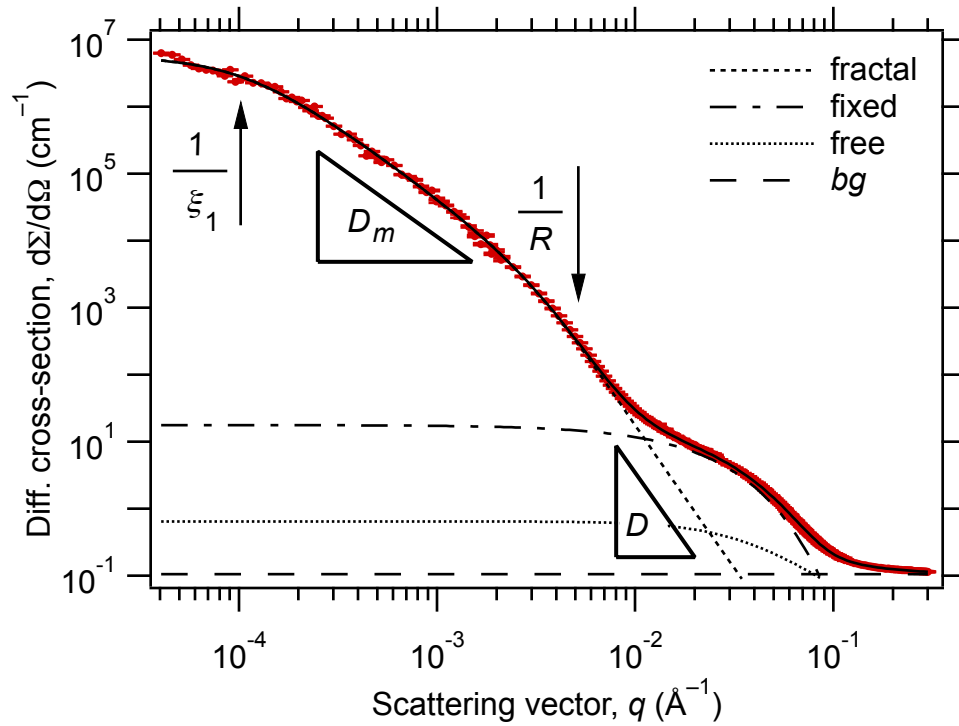


Figure 3.4: Differential scattering cross-section from a cycle-one PVA hydrogel. The solid line is the model fit to the data, i.e., the sum of the individual scattering terms in Eq. 3.7. The contributions of individual terms are indicated by dashed lines. Triangles are shown to mark the slopes that determine the mass fractal dimension, D_m , and surface fractal dimension, $d_s = 4 - D/2$. The positions where the slope changes determine the mass fractal aggregate size, ξ_1 , and blob size, R .

Where supplementary USANS data do not exist, the large scale fractal aggregate parameters cannot be determined because the fractal aggregate size is well beyond the range of the SANS data, and the transition between the slopes D_m and D (Fig. 3.4) occurs approximately at the lower limit of the SANS data. No clear trend was observed for the mass fractal dimension versus the number of thermal cycles, so D_m is held constant at the value of 2.2 determined above. For this value of D_m , the structure factor (Eq. 3.6) reduces to

$$S(q) = 1 + \frac{1.92}{(qR)^{2.2}} \quad (3.8)$$

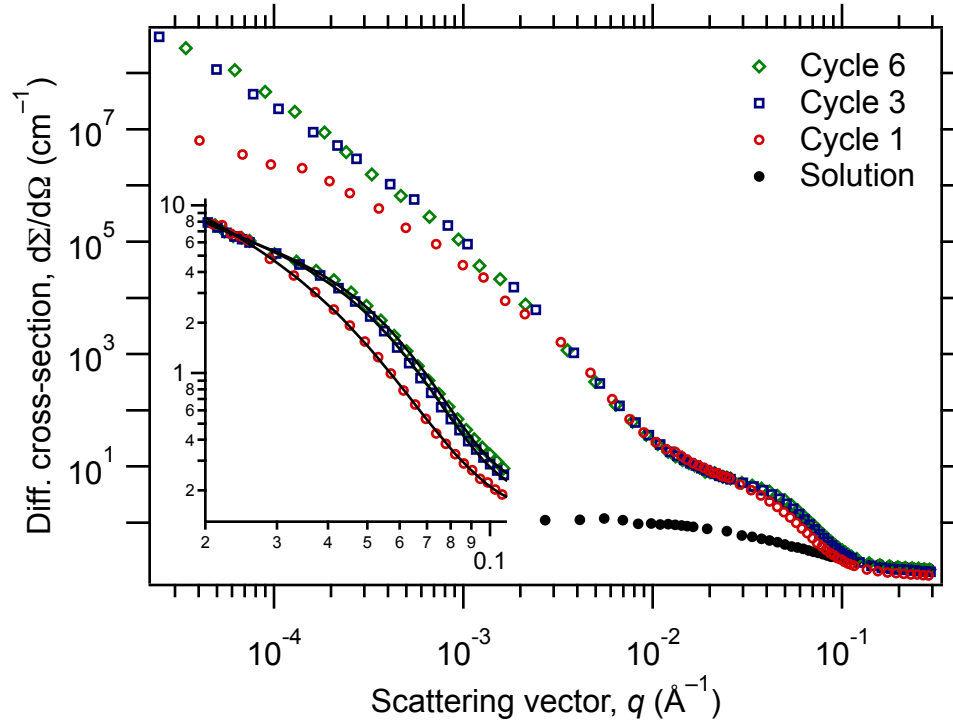


Figure 3.5: Differential scattering cross-sections from cycle-one, -three, and -six PVA hydrogels. Four-fifths of the data points have been omitted for clarity, and data for solution are included for comparison. Inset: Expanded view of the high- q scattering data dominated by the small-scale fixed polymer scattering. The solid lines are the model fit to the data.

in the limit $q\xi_1 \gg 1$. The smallest product $q\xi_1$ occurs for the cycle-one gel (smallest ξ_1), and in this case, the full structure factor differs from Eq. 3.8 by 2.6%. Therefore, for all SANS data, Eq. 3.8 differs from Eq. 3.6 by 2.6% or less, justifying the elimination of ξ_1 and the use of Eq. 3.8 for the structure factor during fitting.

Although R was allowed to vary as a fit parameter, it was deemed that the values returned were not reliable except from cycle one where R is smallest. Plots of d_s , ξ_{fixed} , and b versus the processing strain ε_0 are shown in Figs. 3.7, 3.8, and 3.9, respectively. ξ_{free} shows no anisotropy and little or no dependence on N and has the average value 2.7 ± 0.2 nm.

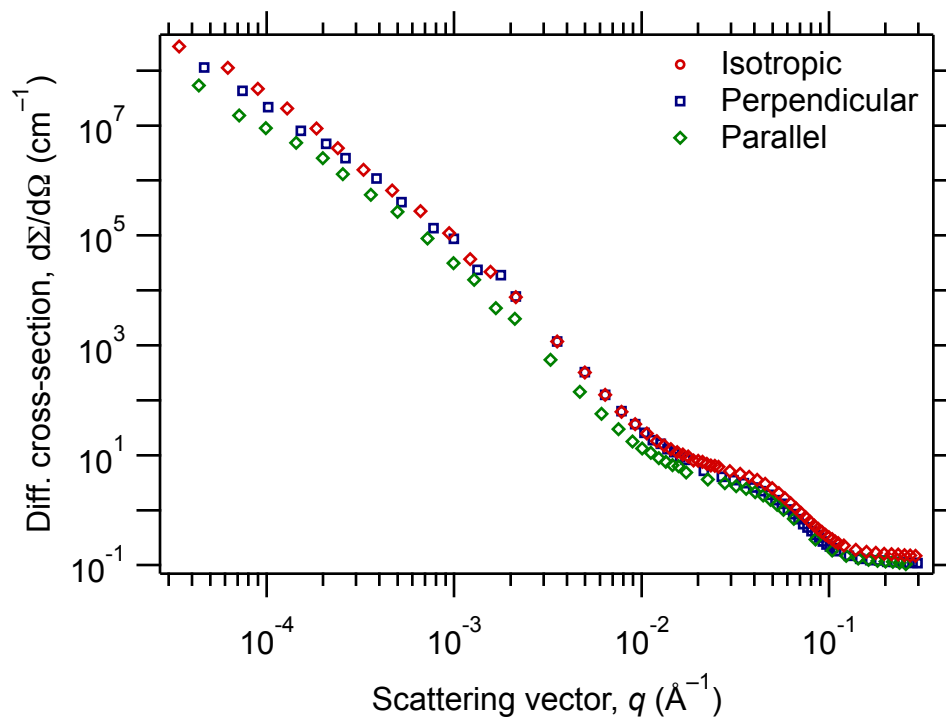


Figure 3.6: Differential scattering cross-sections from cycle-six PVA hydrogels. Data are shown for an isotropic gel and for an anisotropic gel produced with a processing strain of 75%. The anisotropic data are from sector averages parallel and perpendicular to the direction of the processing strain. Four-fifths of the data points have been omitted for clarity.

3.4 Discussion

It is well established that PVA hydrogels are cross-linked by polymer crystallites formed during thermal processing. The modelling of SANS and USANS data and AFM imaging show that the cross-linked polymer is concentrated into relatively dense blobs with a length-scale of a few nanometres assembled in a structure with mass-fractal characteristics up to a length-scale of at least several micrometres. Anisotropic gels show similar characteristics, but exhibit longer length-scales in the direction of the strain applied during processing.

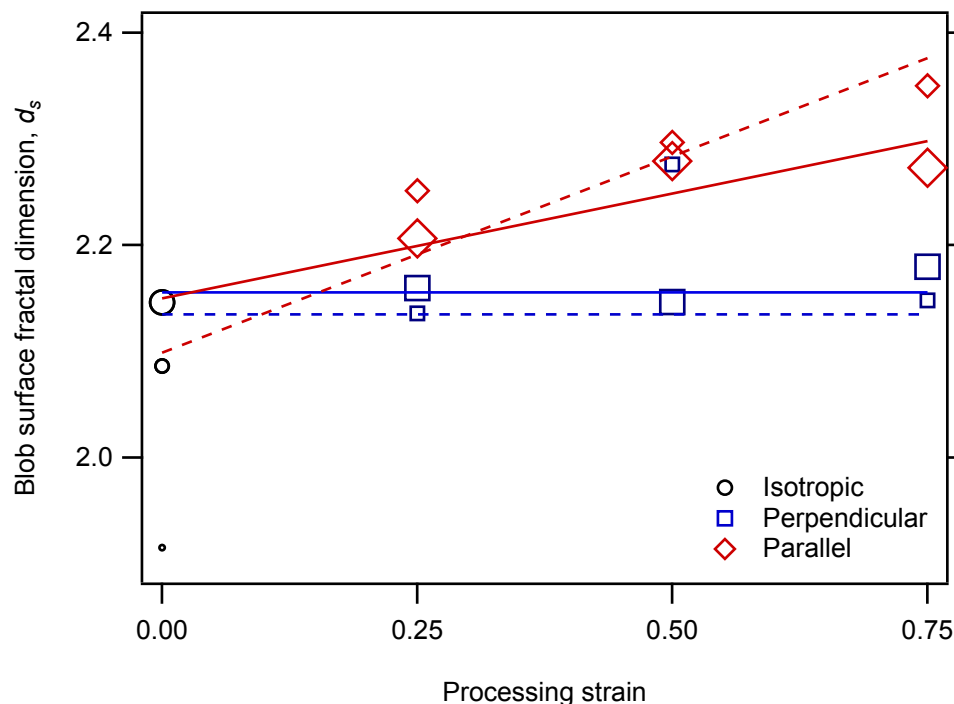


Figure 3.7: Surface fractal dimension versus processing strain. Data for cycles one, three, and six are represented by small, medium, and large symbols, respectively. Trends versus processing strain are shown for cycle three (dashed lines) and cycle six (solid lines). Error bars (not shown for clarity) range from 0.02 to 0.09.

3.4.1 Isotropic Gels

The smallest length-scales (highest q) show a feature that is well modelled by the density correlation function previously applied to cross-linked gels by Horkay and Geissler. The characteristic length of the density fluctuations, 4.7 nm, obtained by a fit to this model for a weak, cycle-one gel, is larger than the screening length of 2.9 nm obtained for the ungelled solution, but the relative sharpness of the feature (see Fig. 3.5) and exponential (vs. power-law) decay of the correlation function indicates a more compact structure. This argues that the gelation process has concentrated the PVA into clumps, which are taken to be crystallites surrounded by dangling chains. This necessarily means that other regions have been depleted of polymer, consistent with the structure of polymer-poor pores that

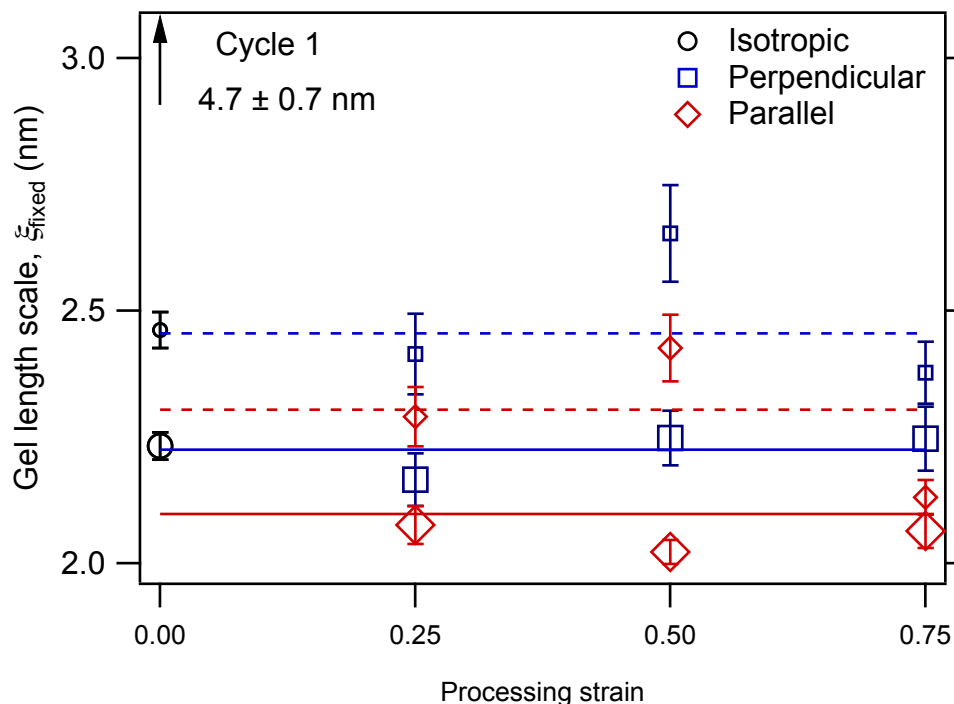


Figure 3.8: Fixed gel length-scale versus processing strain. Data for cycles one, three, and six are represented by small, medium, and large symbols, respectively. Average values are shown for cycle three (dashed lines) and cycle six (solid lines). Error bars (not shown for clarity) range from 0.02 to 0.1.

has been previously described.

Continued cycling systematically decreases the length-scale ξ_{fixed} of the density fluctuations and sharpens the fall-off of the correlation function parameterized by the exponent b as shown in Figs. 3.8 and 3.9 versus processing strain, respectively (the present discussion focuses on a processing strain of 0 only). It is thus apparent that the freeze/thaw process enhances the density fluctuations and expels water from the polymer-rich regions, possibly by increasing the size and perfection of existing crystallites and/or by nucleating additional crystallites, as described previously [32]. This indicates that thermal cycles promote separation between water and PVA on nanometre scales.

Larger length-scales, represented by q values below 0.01 \AA^{-1} in Fig. 3.5, show that the

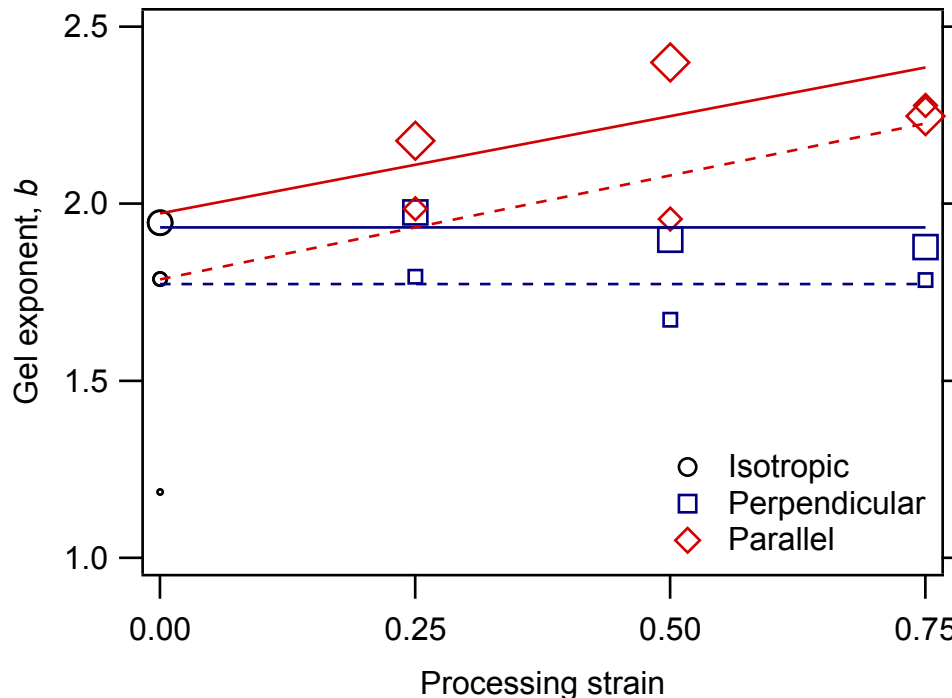


Figure 3.9: Gel exponent versus processing strain. Data for cycles one, three, and six are represented by small, medium, and large symbols, respectively. Trends versus processing strain are shown for cycle three (dashed lines) and cycle six (solid lines). Error bars (not shown for clarity) range from 0.01 to 0.07.

density fluctuations are organized into large structures. The observation that the scattering data do not level off for small q , except possibly for the weakest gel, indicates features extending from $\sim 1 \mu\text{m}$ for cycle-one gels to at least several μm for cycle-three and -six gels. The low- q regime was not successfully modelled using structures described by a single length-scale (e.g., the Debye-Anderson Brumberger form factor), so a structure of blobs of characteristic size R and surface fractal dimension d_s arranged in a mass fractal aggregate of dimension D_m and extent ξ_1 was considered.

The modelling reveals that the blob size increases abruptly from 18 nm to ~ 50 nm between cycles 1 and 3, with little change thereafter. The surface fractal dimension of these blobs is 1.9 for cycle-one gels and fairly uniform at ~ 2.1 for cycle-three and -six

gels. A fractal dimension less than 2 indicates that the surface is diffuse. This suggests that there is a significant amount of loosely bound polymer available at the surfaces of the blobs to reinforce the gel structure during later thermal cycles. It is noteworthy that the gel correlation length ξ_{fixed} and blob size R are similar to the principal length-scales of the gel phase described in a previous study [5], albeit determined from a different model. The interpretation is that the gel phase consists of polymer crystallites of size no more than a few nanometres surrounded by uncrystallized polymer. As is usual in polymer crystallization, significant portions of chains participating in crystallization are expected to extend from the crystallite surfaces. These may extend to other crystallites or be entangled with chains extending from other crystallites, creating a gel. It is noted that the natural length-scales of the PVA stock—a radius of gyration of 13–15 nm, as determined from a simple self-avoiding random-walk model [18], and contour length of 830–1060 nm based on its molecular weight—is consistent with the gel length-scales measured here.

The maximum size of the mass-fractal aggregates is at or above the largest length-scale probed by the USANS data, limiting the ability to determine the large-scale structure accurately. However, it is clear from the data of Fig. 3.5 that the maximum length-scale increases abruptly between cycles 1 and 3, but likely does not change much between cycles 3 and 6.

The hierarchy of structures described above is corroborated by direct imaging. The AFM images shown in Fig. 3.10 reveal structures on several scales. At the smallest scales imaged, seen in Fig. 3.10(a), dense regions with sizes ~ 100 nm are seen surrounding randomly distributed regions with sizes from several 100 nm to ~ 1 μm . Although the softness of the gel limits the resolution of the images so that no structure can be seen inside the denser regions, the pictures are consistent with the model of connected polymer blobs forming an aggregate around polymer poor pores. At larger scales, Fig. 3.10(b), it is seen that the dense regions form structures of at least a few micrometres. It is only at very large scales, as in Fig. 3.10(c), that a more uniform structure exists, though even then ridges and

furrows, which may be relics of dendritic ice crystals, are evident.

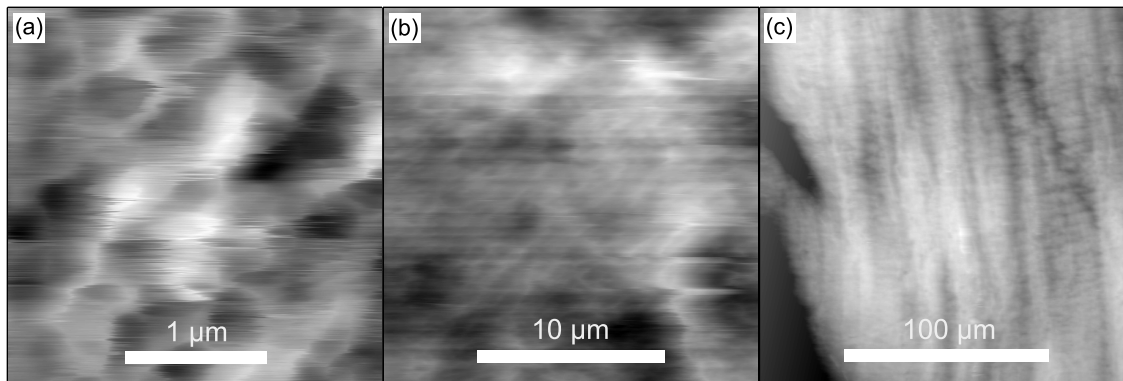


Figure 3.10: Contact mode atomic force microscopy images of a cycle-ten PVA hydrogel that were taken under fluid. Images (a) and (b) were acquired with unmodified tips and image (c) was acquired with a 20-micron glass bead tip. Brighter shading corresponds to higher features.

It is noted that structures similar to those shown by the AFM have been demonstrated by Fergg, et al. using confocal microscopy [33], although in that case the pores were considerably larger ($\sim 6 \mu\text{m}$), perhaps due to the limited ability of optical techniques to resolve smaller details in such a complicated material.

Previous mechanical studies [1, 2, 4, 34] show that the Young's modulus of PVA hydrogels increases monotonically with the number of thermal cycles. This increase could result from both the increased crystallinity indicated by the decrease in the gel length-scale ξ_{fixed} and exponent b , and the increased size of the largest gel aggregates, as shown by the USANS data. However, the observation that the main change in the large structure occurs between cycles one and three while the mechanical strength continues to increase at least up to cycle six suggests that the increase is mainly due to strengthening of the gel phase within the blob structures.

3.4.2 Anisotropic Gels

Anisotropic gels—i.e., those subjected to a strain during thermal cycling—show clear differences in scattering between the directions parallel and perpendicular to the strain direction, thus producing the elliptical patterns in the 2D SANS data shown in Fig. 3.1. Fig. 3.6 shows the differential scattering cross-sections determined by SANS and USANS for the two principal directions measured for a sample subjected to a strain of 75% after one thermal cycle and cycled an additional 5 times (the corresponding isotropic scattering from Fig. 3.5 is shown for comparison).

It is immediately evident that the most striking differences between scattering from isotropic and anisotropic samples are seen at low q . This is quantified by the fits of combined SANS/USANS data to the functional form of Eq. 3.7, which show that while the size of the fractal aggregates in the direction perpendicular to the processing strain remain somewhat constant at a few micrometres, the aggregates are consistently larger than the maximum size that can be probed by USANS in the parallel direction (see Table 3.3). The blob sizes determined from the combined data sets also show a markedly larger value in the direction parallel to the processing strain. Note, though, that this increase is certainly less than the strain itself, suggesting some relaxation during the remaining cycles. Together, these observations suggest that, while the blobs are elongated along the strain direction (and possibly slightly contracted in the perpendicular direction), the main source of the permanent anisotropic mechanical properties is at the largest length-scales, as has been suggested previously [5].

In order for the structural rearrangements that take place upon stretching to become permanent after further cycling, additional cross-links must form to prevent the structure from collapsing back to an isotropic state after the strain is released. To study anisotropy at small length-scales, SANS data were acquired for samples having applied strains from 0 (isotropic) to 0.75 at intervals of 0.25. For each of the small length-scale parameters—gel length-scale, gel exponent, blob size, and blob surface fractal dimension—linear fits versus

strain were performed to determine whether there was a significant trend.

Fig. 3.7 shows no significant change in the surface fractal dimension between cycles three and six for isotropic gels. However, there is a significant trend versus the processing strain in the parallel direction of the anisotropic samples. In this direction, p-values of 0.032 and 0.035 for cycles three and six, respectively, indicate that the observed trend is less than 4% likely to have occurred by chance. No significant trend is seen in the perpendicular direction, so these data are fit to constant values (horizontal lines in Fig. 3.7), resulting in very nearly the same values for cycles 3 and 6.

No systematic dependence on the processing strain is evident in Fig. 3.8, showing that the gel phase itself does not exhibit significant anisotropy. However, Fig. 3.9 shows that the gel exponent increases slightly between cycles three and six. There may be slight dependence on the processing strain for the parallel direction as one linear trend was significant at the 5% level, but not the perpendicular direction: the p-values are 0.041 and 0.13 in the parallel direction and 0.61 and 0.18 in the perpendicular direction, for cycles 3 and 6 respectively.

The relatively minor change in gel length-scale and exponent as a function of processing strain argues that rearrangements at this scale are unimportant to the anisotropy in mechanical properties that has been previously reported [4]. It is hypothesized that the dense polymer network inside the blobs is much stronger than the bulk gel so that when strain is applied it is easier to change the position of blobs in the gel than to stretch the blobs themselves. This would cause a net alignment of connections between blobs in the direction of strain, increasing the roughness of blob surfaces, and hence the associated fractal dimension, in that direction. It is interesting that the mechanical data show no significant dependence on processing strain of the Young's modulus in the perpendicular direction, in agreement with the lack of structural change in that direction seen here.

3.5 Conclusion

By applying a stress during thermal processing, anisotropic PVA hydrogels can be produced. Previous results have shown that with proper selection of processing parameters, the bulk anisotropic elastic properties can be made to closely match those of cardiovascular tissue, making the material suitable for the manufacture of grafts and other cardiovascular prostheses. However an understanding of the structural features resulting in this anisotropy is important.

Small- and ultra small-angle neutron scattering was performed to study anisotropic hydrogels at length-scales from 2 nm to 10 μm , extending previous neutron scattering work [5] to larger length-scales. The structure was modelled as blobs of size ~ 50 nm arranged in an aggregate with mass-fractal characteristics up to a maximum length-scale of several micrometres. The polymer inside the blobs was described by a Horkay-Geissler stretched-exponential correlation function. Systematically varying the number of thermal cycles revealed that the resulting increase in gel strength at macroscopic scales is due to an increase in aggregate size, especially for early cycles, as well as an increase in strength of the gel phase, perhaps due to increased crystallinity. It is also evident that mechanical anisotropy resulting from strain applied during processing is due to stretching of the mass fractal aggregates and alignment of the aggregate building blocks. The building blocks themselves are slightly elongated in the direction parallel to the applied processing strain, but little or no anisotropy is observed in the polymer arrangement at the smallest scales.

3.6 Bibliography for Chapter 3

1. Hassan, C. M. & Peppas, N. A. "Structure and Applications of Poly(vinyl alcohol) Hydrogels Produced by Conventional Crosslinking or by Freezing/Thawing Methods." *Adv. Polym. Sci.* **153**, 37–65 (2000).
2. Wan, W. K., Campbell, G., Zhang, Z. F., Hui, A. J. & Boughner, D. R. "Optimizing the Tensile Properties of Polyvinyl Alcohol Hydrogel for the Construction of a Bioprosthetic Heart Valve Stent." *J. Biomed. Mater. Res.* **63**, 854–861 (2002).
3. Paradossi, G., Cavalieri, F., Chiessi, E., Spagnoli, C. & Cowman, M. K. "Poly(vinyl alcohol) as versatile biomaterial for potential biomedical applications." *J. Mater. Sci.* **14**, 687–691 (2003).
4. Millon, L. E., Mohammadi, H. & Wan, W. K. "Anisotropic Polyvinyl Alcohol Hydrogel for Cardiovascular Applications." *J. Biomed. Mater. Res. Part B: Appl. Biomater.* **79B**, 305–311 (2006).
5. Millon, L. E., Nieh, M.-P., Hutter, J. L. & Wan, W. "SANS Characterization of an Anisotropic Poly(vinyl alcohol) Hydrogel with Vascular Applications." *Macromol.* **40**, 3655–3662 (2007).
6. Haruguchi, H. & Teraoka, S. "Intimal hyperplasia and hemodynamic factors in arterial bypass and arteriovenous grafts: a review." *J. Artif. Organs* **6**, 227–235 (2003).
7. Rashid, S. T., Salacinski, H. J., Fuller, B. J., Hamilton, G. & Seifalian, A. M. "Engineering of bypass conduits to improve patency." *Cell Prolif.* **37**, 351–366 (2004).
8. Peppas, N. A. "Turbidimetric studies of aqueous poly(vinyl alcohol) solutions." *Makromol. Chem.* **176**, 3433–3440 (1975).
9. Mori, Y., Tokura, H. & Yoshikawa, M. "Properties of hydrogels synthesized by freezing and thawing aqueous polyvinyl alcohol solutions and their applications." *J. Mater. Sci.* **32**, 491–496 (1997).
10. Willcox, P. J. *et al.* "Microstructure of Poly(vinyl alcohol) Hydrogels Produced by Freeze/Thaw Cycling." *J. Polym. Phys.* **37**, 3438–3454 (1999).
11. Glinka, C. J. *et al.* "The 30 m Small-Angle Neutron Scattering Instruments at the National Institute of Standards and Technology." *J. Appl. Cryst.* **31**, 430–445 (1998).
12. Mildner, D. F. R., Hammouda, B. & Kline, S. R. "A refractive focusing lens system for small-angle neutron scattering." *J. Appl. Cryst.* **38**, 979–987 (2005).

13. Barker, J. G. *et al.* “Applied Design and performance of a thermal-neutron double-crystal diffractometer for USANS at NIST.” *J. Appl. Cryst.* **38**, 1004–1011 (2005).
14. Kline, S. R. “Applied Reduction and analysis of SANS and USANS data using IGOR Pro.” *J Appl. Cryst.* **39**, 895 (2006).
15. Lake, J. A. “An Iterative Method of Slit-Correcting Small Angle X-ray Data.” *Acta. Cryst.* **23**, 191–194 (1967).
16. Rubinstein, M. & Colby, R. H. *Polymer physics* (Oxford University Press, 2003).
17. Li, H. *et al.* “Single molecule force spectroscopy on poly(vinyl alcohol) by atomic force microscopy.” *Macromol. Rapid Commun.* **19**, 609–611 (1998).
18. de Gennes, P.-G. *Scaling Concepts in Polymer Physics* 76 (Cornell University Press, 1979).
19. Ricciardi, R. *et al.* “Structural Organization of Poly(vinyl alcohol) Hydrogels Obtained by Freezing and Thawing Techniques: A SANS Study.” *Chem. Mater.* **17**, 1183–1189 (2005).
20. Auriemma, F., Rosa, C. D. & Triolo, R. “Slow Crystallization Kinetics of Poly(vinyl alcohol) in Confined Environment during Cryotropic Gelation of Aqueous Solutions.” *Macromol.* **39**, 9429–9434 (2006).
21. Mallam, S., Hecht, A.-M. & Geissler, E. “Structure of swollen polydimethyl siloxane gels.” *J. Chem. Phys.* **91**, 6447–6454 (1989).
22. Geissler, E., Horkay, F. & Hecht, A.-M. “Osmotic and Scattering Properties of Chemically Cross-Linked Poly(vinyl alcohol) Hydrogels.” *Macromol.* **24**, 6006–6011 (1991).
23. Horkay, F., Hecht, A.-M., Mallam, S., Geissler, E. & Rennie, A. R. “Macroscopic and Microscopic Thermodynamic Observations in Swollen Poly(vinyl acetate) Networks.” *Macromol.* **24**, 2896–2902 (1991).
24. Geissler, E., Horkay, F. & Hecht, A.-H. “Scattering from network polydispersity in polymer gels.” *Phys. Rev. Lett.* **71**, 645–648 (1993).
25. Horkay, F., Hecht, A.-M. & Geissler, E. “Small Angle Neutron Scattering in Poly(vinyl alcohol) Hydrogels.” *Macromol.* **27**, 1795–1798 (1994).
26. Mallam, S., Horkay, F., Hecht, A.-M., Rennie, A. R. & Geissler, E. “Microscopic and macroscopic thermodynamic observations in swollen poly(dimethylsiloxane) networks.” *Macromol.* **24**, 543–548 (1991).

27. P. Debye, H. R. A. J. & Brumberger, H. "Scattering by an Inhomogeneous Solid. II. The Correlation Function and Its Application." *J. Appl. Phys.* **28**, 679–683 (1957).
28. Emmerling, A. *et al.* "Relationship between optical transparency and nanostructural features of silica aerogels." *J. Non-cryst. sol.* **185**, 240–248 (1995).
29. Roe, R.-J. *Methods of X-Ray and Neutron Scattering in Polymer Science* (Oxford University Press, 2000).
30. Shibayama, M. *et al.* "Small-angle neutron scattering from poly(vinyl alcohol)-borate gels." *Polym.* **33**, 2883–2890 (1992).
31. Chen, S.-H. & Teixeira, J. "Structure and Fractal Dimension of Protein-Detergent Complexes." *Phys. Rev. Lett.* **57**, 2583–2586 (1986).
32. Ricciardi, R., Auriemma, F., Rosa, C. D. & Lauprêtre, F. "X-ray Diffraction Analysis of Poly(vinyl alcohol) Hydrogels, Obtained by Freezing and Thawing Techniques." *Macromol.* **37**, 1921–1927 (2004).
33. Fergg, F., Keil, F. J. & Quader, H. "Investigations of the microscopic structure of poly(vinyl alcohol) hydrogels by confocal laser scanning microscopy." *Colloid. Polym. Sci.* **279**, 61–67 (2001).
34. Yokoyama, F., Masada, I., Shimamura, K., Ikawa, T. & Monobe, K. "Morphology and structure of highly elastic poly(vinyl alcohol) hydrogel prepared by repeated freezing-and-melting." *Coll. Polym. Sci.* **264**, 595–601 (1986).

Chapter 4

Anisotropic Polyvinyl Alcohol Hydrogel: Connection Between Structure and Bulk Mechanical Properties

4.1 Introduction

PVA is a versatile hydrophilic polymer that can be made into hydrogels using numerous solvents and cross-linking methods. Soon after the discovery of biocompatible physically cross-linked PVA hydrogel produced by freezing and thawing aqueous PVA solution [1], efforts to adapt PVA hydrogel for biomedical applications began.

The structure and properties of freeze-thaw PVA hydrogels can be controlled with processing parameters such as the initial PVA concentration [2, 3], the PVA molecular weight [2], the freeze temperature [2, 3], the freeze rate or freeze time [2], and the number of freeze-thaw cycles [4]. Another method for controlling the mechanical properties is to incorporate reinforcing structures into the PVA solution before freeze/thaw cycling. Bacterial cellulose fibres and carbon nanotubes have been added to PVA hydrogel, allowing greater control over strength [5–7].

Here, PVA hydrogels containing of order 10% *w/w* PVA in water that are physically cross-linked using several slow freeze-thaw cycles are discussed, because they can be produced with mechanical properties closely matching those of cardiovascular tissues [8, 9]. Recently, a method for producing these PVA hydrogels with anisotropic mechanical properties was discovered, potentially allowing for manufacture of cardiovascular prostheses that mimic the nonlinear and anisotropic mechanical response of natural cardiovascular tissues [9]. The microscopic structure of these anisotropic PVA hydrogels has been characterized using small- and ultra-small-angle neutron scattering [10, 11], but the connection between the microscopic structure and the bulk elasticity is not well understood.

Both physical and phenomenological models are widely used to explain the elastic response of materials. Most materials, in the small deformation limit, obey Hooke's law and thus exhibit a restoring force proportional to deformation [12]. Further, the entire range of elastic response of many of these materials, prior to yielding or fracturing, is adequately modelled by Hooke's law because they yield or fracture within the small deformation limit. However, Hooke's law is not sufficient for elastomers, which remain elastic beyond the small deformation limit and exhibit nonlinear stress-strain curves.

One approach for predicting the mechanical response of an elastomer is to evaluate its Helmholtz free energy and differentiate with respect to strain. For many elastomers, the internal energy varies negligibly with deformation so the free energy varies mainly with entropy, which decreases as the network is deformed from equilibrium. The entropy of polymer networks may be estimated from model networks constructed with idealized freely-jointed polymer chains [13]. Remarkably, simple network models with repeated unit cells of 3, 4, or 8 chains have proven useful for modelling the elastic response of elastomers [13–15]. In cases where a suitable physical model cannot be found, or an analytic expression for the strain energy is desired, phenomenological models are used. For instance, if one desires to perform finite element analysis on a complex geometry such as a tri-leaf replacement heart valve [16] to determine its response to blood flow, an analytic

expression for the strain energy is preferred over a calculation involving integration or numerical simulation. The successful Mooney-Rivlin model writes the strain energy density as a sum of strain invariants of the deformation tensor without giving consideration to the macromolecular structure of the material [17, 18].

In Chapter 3, it was shown that the polyvinyl alcohol (PVA) hydrogel structure could be modelled as interconnected PVA blobs of size 20 to 50 nm arranged in fractal aggregates extending to micrometers or tens of micrometers. Furthermore, it was shown that anisotropy was due to elongation of the fractal aggregates and alignment of blobs, but that individual blobs and their internal structures showed only slight anisotropy. The full model fit to the data was

$$\frac{d\Sigma}{d\Omega} = P(q)S(q) + \left(\frac{d\Sigma}{d\Omega}\right)_{\text{static}} + \left(\frac{d\Sigma}{d\Omega}\right)_{\text{dyn}} + bg. \quad (4.1)$$

The form factor

$$P(q) = \frac{A_1 R^3}{\left[1 + \frac{D+1}{3} (Rq)^2\right]^{D/2}} \quad (4.2)$$

describes scattering from an average polymer blob of size R , surface fractal dimension $d_s = 4 - D/2$, and scattering amplitude A_1 [19]. The structure factor

$$S(q) = 1 + \frac{D_m \Gamma(D_m - 1)}{(qR)^{D_m}} \left[\left(1 + \frac{1}{(q\xi_1)^2}\right)^{(1-D_m)/2} \times \sin[(D_m - 1) \arctan(q\xi_1)] \right] \quad (4.3)$$

describes interference effects of polymer blobs in a fractal aggregate of extent ξ_1 and mass fractal dimension D_m [20]. The term

$$\left(\frac{d\Sigma}{d\Omega}\right)_{\text{fixed}}(q) = A_{\text{static}} \exp\left[-(q\xi_{\text{static}})^b\right] \quad (4.4)$$

describes scattering from permanent, polymer density fluctuations of average size ξ_{fixed}

resulting from physical cross-linking [21]. Finally,

$$\left(\frac{d\Sigma}{d\Omega}\right)_{\text{free}}(q) = \frac{A_{\text{free}}}{1 + (q\xi_{\text{free}})^2} \quad (4.5)$$

describes Ornstein-Zernicke scattering from density fluctuations of size ξ_{free} of free, uncross-linked polymer and the constant bg accounts for incoherent and background scattering.

Here, a more thorough examination of the small-scale gel phase using small-angle neutron scattering (SANS) is conducted to motivate physical models that improve the understanding of the relationship between structure and mechanical properties in anisotropic PVA hydrogel. The models provide insight about the elastic deformation limits of the hydrogel and may assist in the development and durability testing of cardiovascular prostheses such as artificial heart valves.

4.2 Materials and Methods

4.2.1 Neutron Scattering

PVA solutions were prepared by dissolving PVA with an average molecular weight of 146–186 kDa (99+% hydrolyzed, Sigma-Aldrich, Canada) in Deuterium Oxide (D_2O) (99.9 atom%, Sigma-Aldrich, Canada) to achieve a D_2O :PVA molar ratio of 21.9:1, which matches the molar composition used below for mechanical testing. The solution was held at 95 °C while stirring for 1 h to fully dissolve the PVA, similar to the procedures reported previously [9–11]. The stirring assembly included a water-cooled condenser surrounding its shaft to prevent the loss of D_2O .

Cooled PVA solution was used to fill aluminum moulds comprised of 10 cm \times 10 cm plates of aluminum separated by a 1.6 mm thick poly(tetrafluoroethylene) (PTFE) gasket. The solution was carefully added to the moulds using a syringe to prevent air bubbles from being introduced to the solution. Moulds were sealed and submerged in a Neslab RTE-

Table 4.1: NG7 SANS configurations.

SDD (m)	λ (Å)	q (Å ⁻¹)	r (nm)
1.0	6.0	0.050 – 0.54	1.2 – 13
5.0	6.0	0.0099 – 0.11	5.7 – 63
15.3 ^a	8.09	0.0011 – 0.026	24 – 570

^a Lens configuration to achieve low q

111 water bath (Thermo Fisher Scientific, Inc., Waltham, MA) for thermal cycling using temperature control software implemented in Igor Pro (WaveMetrics, Portland, OR). Each cycle consisted of ramping the temperature from 20 °C to –20 °C at 0.1 °C/min, holding the temperature at –20 °C for 6 h, ramping the temperature back to 20 °C at 0.1 °C/min, and holding the temperature at 20 °C for 1 h. This cycle was repeated as required.

SANS experiments were performed on the NG7 beamline at the National Institute of Standards and Technology (NIST) in Gaithersburg, MD [22]. Three sample-to-detector distance (SDD) and wavelength (λ) combinations were used to cover a scattering vector (q) range from 0.0011–0.54 Å⁻¹, as shown in Table 4.1. The corresponding length-scales $r = 2\pi/q$ range from 1.2–570 nm. At each SDD configuration, the detector was offset 20 cm from centre to achieve a larger q -range. At the longest SDD configuration, a focusing lens system consisting of concave MgF₂ lenses was used to provide better low- q resolution and higher flux than could be attained using a conventional pinhole collimation system [23, 24]. Data were collected for isotropic samples prepared with one, two, three, four, six, and ten thermal cycles.

Differential scattering cross-sections ($d\Sigma/d\Omega(\mathbf{q})$) were extracted from the SANS data in Igor Pro (WaveMetrics, Inc., Portland, OR), using routines provided by NIST [25]. The data were corrected for background and empty sample cell scattering, divided by the sensitivity of the detector, and converted to absolute scaling in units of cm⁻¹. One-dimensional differential scattering cross-sections were extracted by circularly averaging the isotropic

data about the $q = 0$ position. For each sample, data from the three q -ranges were combined into a single SANS data set spanning a range of $0.0011 < q < 0.54 \text{ \AA}^{-1}$.

4.2.2 Mechanical Testing

10% (w/w) PVA solution was prepared by dissolving PVA from the same batch used in Section 4.2.1 in distilled water. The solution was held at 90 °C while stirring for 3 h to fully dissolve the PVA, similar to the procedures reported previously [9–11].

PVA hydrogels were prepared by filling aluminum moulds with cooled PVA solution and thermal cycling the moulds in a heated/refrigerated circulator (VWR Model 1180S). For each thermal cycle, the temperature was ramped from 20 °C to –20 °C at 0.1 °C/ min, held at –20 °C for 1 h, and ramped to 20 °C at 0.1 °C/ min. Samples were moulded into sheets 1.6 mm thick. Anisotropic gels were made by stretching cycle-one sheets to 75% strain and securing them in modified aluminum moulds with clamps. While stretched, these sheets were subjected to 1–5 additional thermal cycles.

Uniaxial extension testing was performed with a servo-hydraulic INSTRON 8872 testing system (Norwood, MA) with samples mounted inside a Plexiglas tank filled with distilled water. Unless stated otherwise, the temperature of the water bath was maintained at 310 K (37 °C). Strips of gel of width 5 mm were punched out of the hydrogel sheets and secured in a custom-designed tissue grip with initial grip-to-grip distance of 10 mm and attached to the 1 kg load cell of the material testing system. All samples were preconditioned with 10 loading and unloading cycles between 0 and 65% strain before load-extension data were acquired at an extension rate of 40 mm/s to 65% strain.

To test the temperature dependence of stress versus strain, uniaxial extension tests were made repeatedly on isotropic cycle-two and -six hydrogels while slowly heating a pre-chilled bath from 277 K (4 °C) to 314 K (41 °C) over a period of 3 h. The bath was stirred between measurements and small amounts of water were frequently added to maintain the water level in the bath.

In all cases, sample dimensions were measured using a Mitutoyo thickness tester and deformation versus load data were converted to engineering stress versus engineering strain. Engineering stress is defined as the tension in the sample divided by the initial cross-sectional area of the sample and engineering strain is defined as the change in length of the sample divided by the equilibrium length of the sample.

4.3 Theory and Data Analysis

4.3.1 Neutron Scattering

The largest length-scales of the fractal aggregates, ξ_1 and D_m , are beyond the range of the SANS data and, without ultra small-angle neutron scattering (USANS) data, cannot be determined by fitting Eq. 4.1. From the previous neutron scattering study, it was determined that the aggregate size has a minimum of 0.9 μm for cycle one and that D_m has an average value of 2.2 ± 0.2 [11]. With these values, the SANS data satisfy $q\xi_1 \gg 1$ over the full q -range and the structure factor (Eq. 4.3) is accurately approximated by [11]

$$S(q) = 1 + \frac{1.92}{(qR)^{2.2}}. \quad (4.6)$$

With Eq. 4.6 as the structure factor, Eq. 4.1 was fit to the reduced SANS data, allowing the PVA blob size (R), blob surface fractal dimension (d_s), fixed polymer gel length-scale (ξ_{fixed}), fixed polymer gel exponent (p), and free polymer length-scale (ξ_{free}) to be determined. Reduced data and fits of the model from cycle-one and cycle-ten gels are shown in Fig. 4.1.

Values of the polymer blob size, R , versus the number of thermal cycles, N , is shown in Table 4.2. The blob size jumps between thermal cycle one and two, but remains constant thereafter with a weighted mean and variance of 46.8 ± 0.8 nm. The surface fractal dimension of the blobs, d_s , does not have a significant dependence on N , as the slight trend

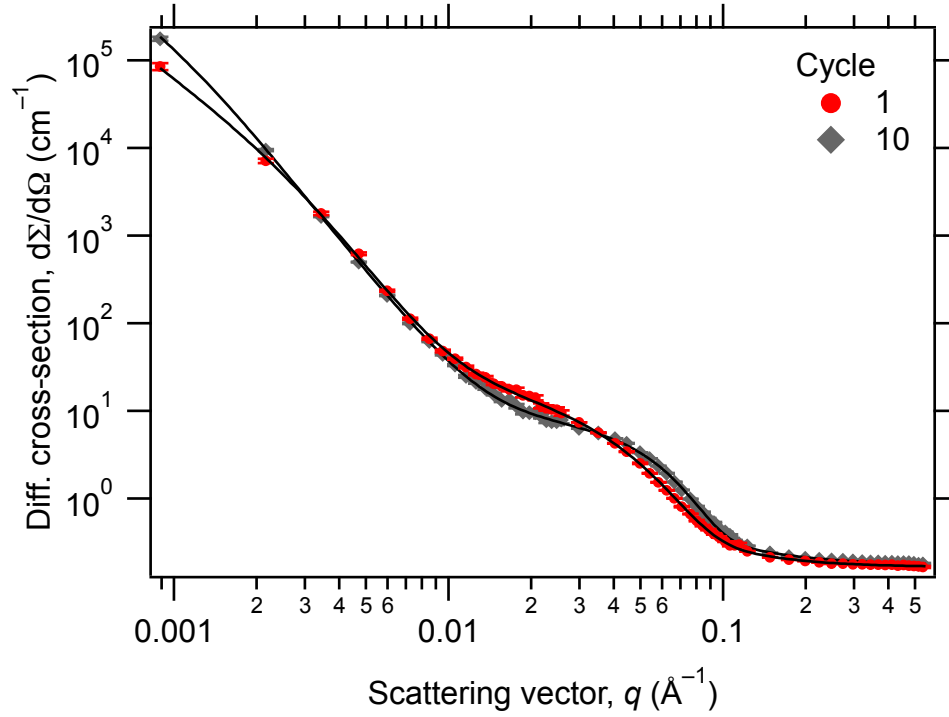


Figure 4.1: Differential scattering cross-sections from cycle-one and cycle-ten hydrogels. The solid lines are the model fit to the data. Four-fifths of the data points have been omitted for clarity.

observed had probabilities of 16% or more of occurring by chance. The weighted mean and variance of the surface fractal dimension is 2.140 ± 0.002 .

4.3.2 Stress of Entropic Polymer Networks

To determine elastic properties arising from entropy, a model network is constructed from entropic chains and the total entropy of the network, S , is found as a function of the network's configuration. The entropy of a network of cross-linked polymer strands can be found by summing the entropies of individual strands. At constant temperature T and with negligible change in internal energy during deformation, the engineering stress of a sample deformed along axis α is

$$\sigma_{\alpha} = -T \frac{\partial S}{\partial \lambda_{\alpha}}. \quad (4.7)$$

Table 4.2: Blob size R versus the number of thermal cycles.

Number of thermal cycles, N	Blob size, R (nm)
1	21.4 ± 0.7
2	54 ± 6
2	47 ± 3
3	48 ± 2
4	46 ± 1
6	46 ± 2
10	47 ± 2

where λ_α is the fractional deformation along axis α . The fractional deformation is defined as sample length divided by equilibrium length and is related to the engineering strain, ε_α , by

$$\lambda_\alpha = \varepsilon_\alpha + 1. \quad (4.8)$$

PVA chains have short persistence lengths and can be adequately modelled as freely-jointed chains. A freely-jointed polymer chain experiences a tension that pulls its ends together because the entropy of the chain increases as the end separation decreases. The entropy of a single freely-jointed chain is

$$s = c - k_B n \left[\frac{r}{nl} \mathcal{L}^{-1} \left(\frac{r}{nl} \right) + \ln \frac{\mathcal{L}^{-1} (r/nl)}{\sinh \mathcal{L}^{-1} (r/nl)} \right]$$

where c is a constant, k_B is the Boltzmann constant, n is the number of steps in the idealized, freely jointed chain, r is the distance between the endpoints of the chain, l is the link or step size of the chain, and \mathcal{L}^{-1} is the inverse Langevin function [13]. The product nl is the contour length of the polymer chain and determines the maximum separation of the endpoints. Hence the fraction r/nl is referred to as the fractional extension of the chain.

Letting $x = r/nl$,

$$s(x) = c - k_B n \left[x \mathcal{L}^{-1}(x) + \ln \frac{\mathcal{L}^{-1}(x)}{\sinh \mathcal{L}^{-1}(x)} \right]. \quad (4.9)$$

Entropy is maximized when each strand has zero end-to-end length, so an unconstrained network will collapse to a single point. This behaviour is commonly avoided by constraining the network to have fixed non-zero volume [13, 14]. Since the compressibility of water is negligible and extrusion of water from the hydrogel during extension is not observed, volume conservation is employed here. To honour the volume conservation constraint, the fractional deformations must satisfy

$$\lambda_x \lambda_y \lambda_z = 1. \quad (4.10)$$

For isotropic PVA hydrogels, the utility of the isotropic 3-chain model of Treloar [13] and the 8-chain model of Arruda and Boyce [14] for modelling uniaxial extension is evaluated. Both models are considered because they have fundamental differences. Polymer strands in the 3-chain model undergo affine deformation, meaning that the fractional deformation of each chain equals the fractional deformation of the bulk sample, λ_α , in the corresponding direction α , and may have different fractional extensions in different directions. Strands in the 8-chain model do not undergo affine deformation and all have the same fractional extension. For anisotropic PVA hydrogels, anisotropic versions of the 3-chain and 8-chain models are developed. Finally, the temperature dependence of the elasticity is tested to verify that entropy dominates the mechanical behaviour.

4.3.3 Uniaxial Extension of Isotropic Hydrogels

3-Chain Model

The simplest polymer network model is the 3-chain model which is constructed by repeating a cubic unit cell containing three polymer chains. The chains are placed on three

edges of the unit cell with one strand parallel to each of the Cartesian coordinate axes and cross-linked at the vertices of the cube as shown in Fig. 4.2 [13]. In order to solve for stress versus fractional deformation, the network is deformed in the x -direction, making the fractional deformation parallel to the x axis, λ_x , the independent variable. The network responds to elongations in the x -directions by contracting in the other two directions by fractional deformations λ_y and λ_z . λ_y and λ_z are dependent variables that assume the values that maximize the entropy, subject to the volume conservation constraint of Eq. 4.10.

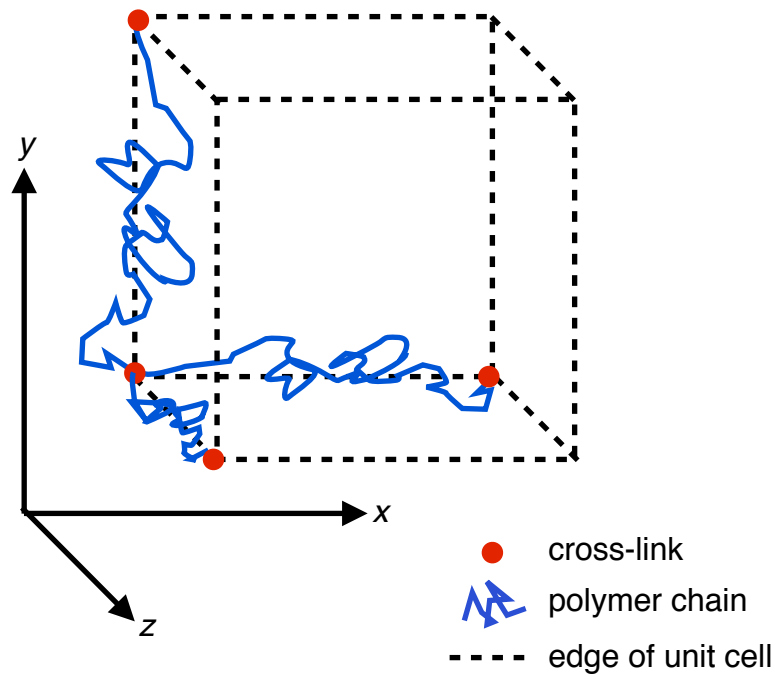


Figure 4.2: Unit cell of the isotropic 3-chain network model.

The entropy per cubic metre of the isotropic 3-chain network is

$$S = \frac{N}{3} [s(x_x) + s(x_y) + s(x_z)], \quad (4.11)$$

where N is the total number of strands per cubic metre and $s(x_\alpha)$ is the entropy of a single strand parallel to axis α with fractional extension x_α . In the isotropic case, all chains start

with the same equilibrium chain length, r_0 , and equilibrium fractional extension, x_0 . As a result of affine deformation, the fractional extension of chains along axis α in the deformed network is $x_\alpha = \lambda_\alpha x_0$.

Due to symmetry, an isotropic network contracts equally in the y and z directions when elongated in the x direction so

$$\lambda_z = \lambda_y = \frac{1}{\sqrt{\lambda_x}}$$

when volume is conserved. The entropy of the deformed network from Eq. 4.11 is then

$$S = \frac{N}{3} \left[s(\lambda_x x_0) + 2s\left(\frac{x_0}{\sqrt{\lambda_x}}\right) \right]. \quad (4.12)$$

Substitution of Eq. 4.12 into Eq. 4.7 gives [13], for the stress,

$$\sigma_x(\lambda_x) = \frac{Nk_B T n x_0}{3} \left[\mathcal{L}^{-1}(\lambda_x x_0) - \lambda_x^{-3/2} \mathcal{L}^{-1}\left(\frac{x_0}{\sqrt{\lambda_x}}\right) \right]. \quad (4.13)$$

Before fitting the experimental data, it is noted that only two of three parameters N , n , and x_0 are independent and none are independently known in the material.

To proceed, Eq. 4.13 is expanded to first order in λ_x using $\mathcal{L}^{-1}(x) \approx 3x$ to obtain

$$\sigma_x(\lambda_x) = Nk_B T n x_0^2 (\lambda_x - \lambda_x^{-2}).$$

This is equivalent to replacing finitely extensible Langevin chains with infinitely extensible Gaussian chains. At large fractional extension, stress is proportional to fractional extension with elastic modulus

$$G = Nk_B T n x_0^2. \quad (4.14)$$

Further, it is noted that if the equilibrium length of the chains is assumed to be their random walk length as Treloar did, the result is $r_0 = \sqrt{nl}$ and $n x_0^2 = 1$ and the elastic modulus of $Nk_B T$ for a network of Gaussian chains is recovered [13]. Using Eq. 4.14, Eq. 4.13 is

rewritten as

$$\sigma_x(\lambda_x) = \frac{G}{3x_0} \left[\mathcal{L}^{-1}(\lambda_x x_0) - \lambda_x^{-3/2} \mathcal{L}^{-1}\left(\frac{x_0}{\sqrt{\lambda_x}}\right) \right] \quad (4.15)$$

which has two independent free parameters: x_0 and an effective elastic modulus, G .

Fits of Eq. 4.15 to engineering stress versus engineering strain for isotropic PVA hydrogels produced with one through six thermal cycles are shown in Fig. 4.3. The model describes the data well, but tends to slightly overestimate the stress at small strains.

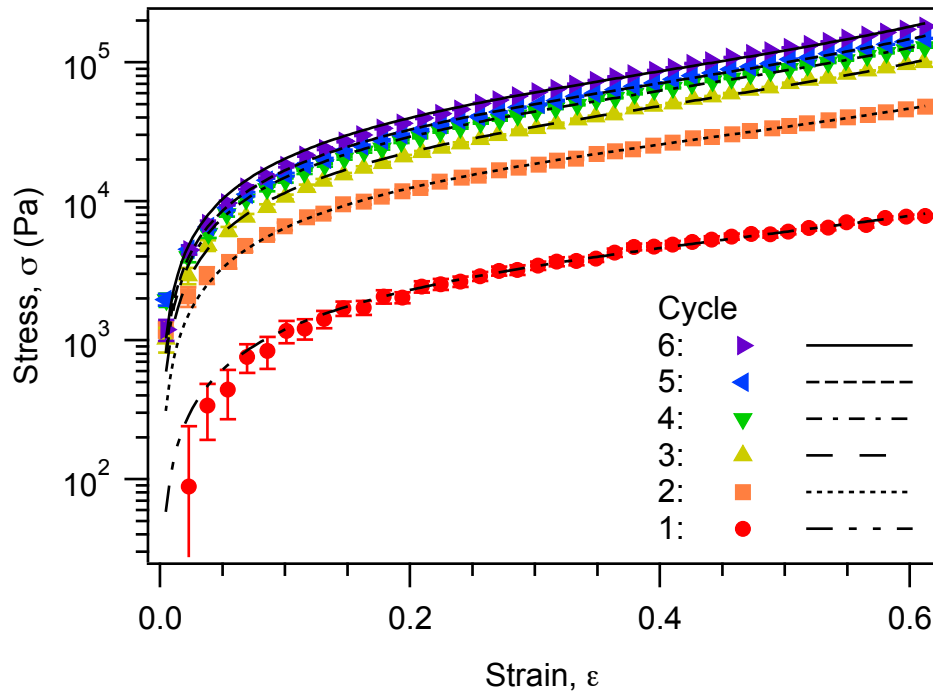


Figure 4.3: Engineering stress versus engineering strain for isotropic hydrogels produced with one through six thermal cycles. Points are experimental data and lines are fits of the isotropic 3-chain model to the data.

8-Chain Model

The unit cell of the 8-chain model of Arruda and Boyce [14, 15] is constructed by connecting a polymer strand from each of the eight corners of a rectangular prism to a central node as shown in Fig. 4.4. Each chain has the same fractional extension regardless of deforma-

tion state because the equilibrium position of the central node is at the centroid of the unit cell [14]. For fractional deformations λ_x , λ_y , λ_z of the network, the fractional deformation of polymer strands is

$$\lambda_{\text{chain}} = \sqrt{\frac{1}{3}(\lambda_x^2 + \lambda_y^2 + \lambda_z^2)}$$

and the entropy of the network is

$$S = Ns(\lambda_{\text{chain}}x_0).$$

For uniaxial extension in the x direction,

$$\lambda_{\text{chain}} = \sqrt{\frac{1}{3}\left(\lambda_x^2 + \frac{2}{\lambda_x}\right)}$$

and the engineering stress is

$$\sigma_x(\lambda_x) = \frac{Nk_B T n x_0}{3} \frac{\mathcal{L}^{-1}(\lambda_{\text{chain}}x_0)(\lambda_x - \lambda_x^{-2})}{\lambda_{\text{chain}}}. \quad (4.16)$$

Using Eq. 4.14 as for the 3-chain model,

$$\sigma_x(\lambda_x) = \frac{G}{3x_0} \frac{\mathcal{L}^{-1}(\lambda_{\text{chain}}x_0)(\lambda_x - \lambda_x^{-2})}{\lambda_{\text{chain}}}. \quad (4.17)$$

Fits of Eq. 4.17 to engineering stress versus engineering strain for isotropic PVA hydrogels produced with one through six thermal cycles are shown in Fig. 4.5. The 8-chain model, much like the 3-chain model, matches the data well but also tends to slightly overestimate the stress at small strains.

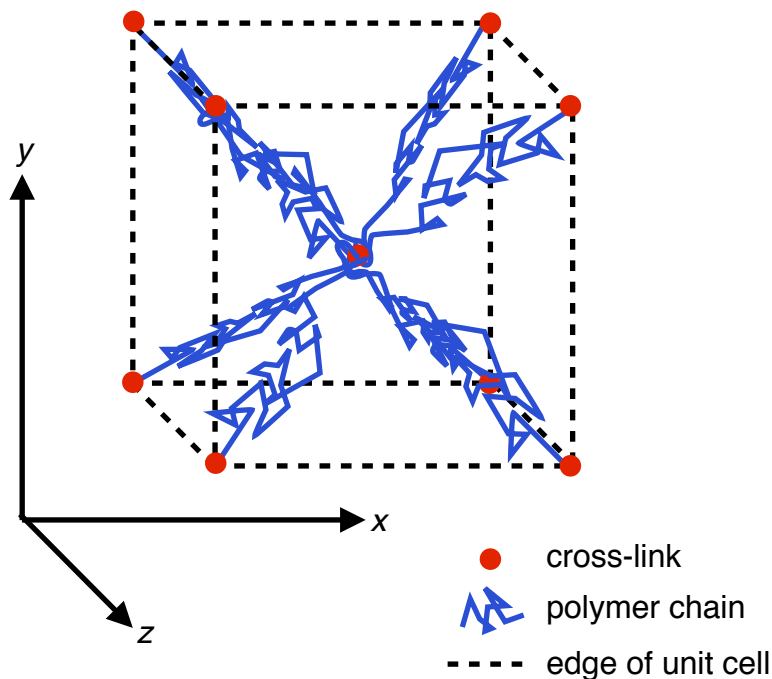


Figure 4.4: Unit cell of the isotropic 8-chain network model.

4.3.4 Uniaxial Extension of Anisotropic Hydrogels

Examples of engineering stress versus engineering strain for uniaxial extension of isotropic and anisotropic cycle-two samples are shown in Fig. 4.6. The isotropic sample underwent two consecutive thermal cycles: once to form a weak gel, and once more with the gel under tension. The resulting anisotropic sample was tested in directions parallel and perpendicular to the direction of the processing tension. Relative to the isotropic sample, the anisotropic sample is much stronger in the parallel direction and slightly weaker in the perpendicular direction.

The anisotropic network is modelled by stretching and clamping an isotropic “base” network model and superimposing a second isotropic “reinforcement” network model onto the stretched network. The deformation of the base network is made equal to the fractional deformation λ_p by which real anisotropic hydrogels were stretched during produc-

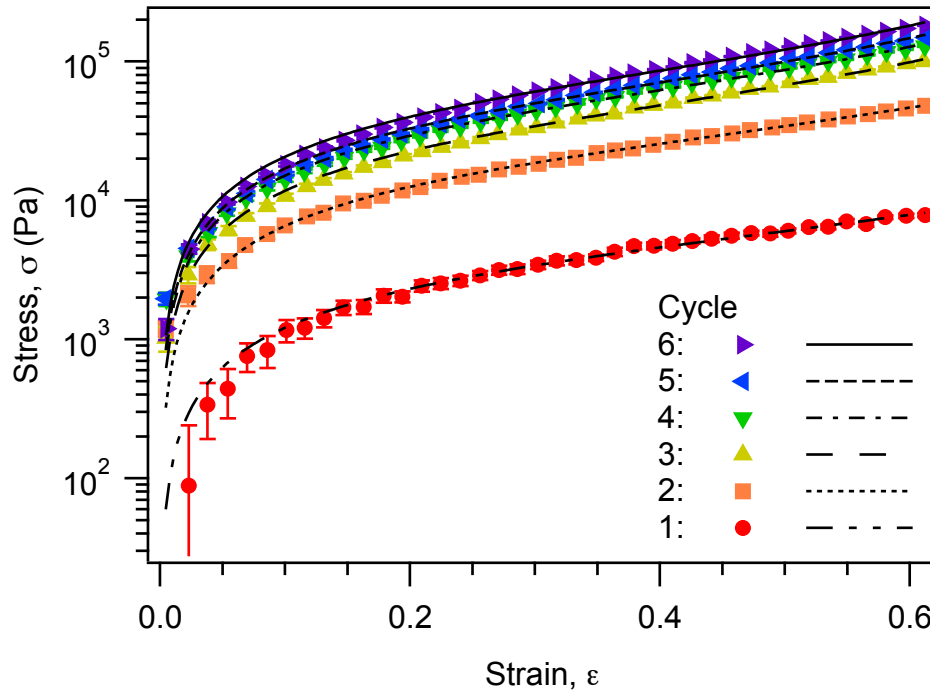


Figure 4.5: Engineering stress versus engineering strain for isotropic hydrogels produced with one through six thermal cycles. Points are experimental data and lines are fits of the isotropic 8-chain model to the data.

tion. Once superimposed, the two isotropic networks deform in conjunction and behave as a single anisotropic network. Additional thermal cycles after the second thermal cycle are assumed to further strengthen the base and reinforcement networks and not to introduce additional networks. Once unclamped, the anisotropic network relaxes to equilibrium by fractional deformation λ_r , which is determined by maximizing the total entropy.

Below, the mechanical properties for such a compound network is determined when deformed in the directions along, and perpendicular to, the direction of the strain applied during processing.

3-Chain Model

Prior to elongation and addition of the reinforcement network, the base network is isotropic. It is assumed that the reinforcement network, which forms after the base network is stretched,

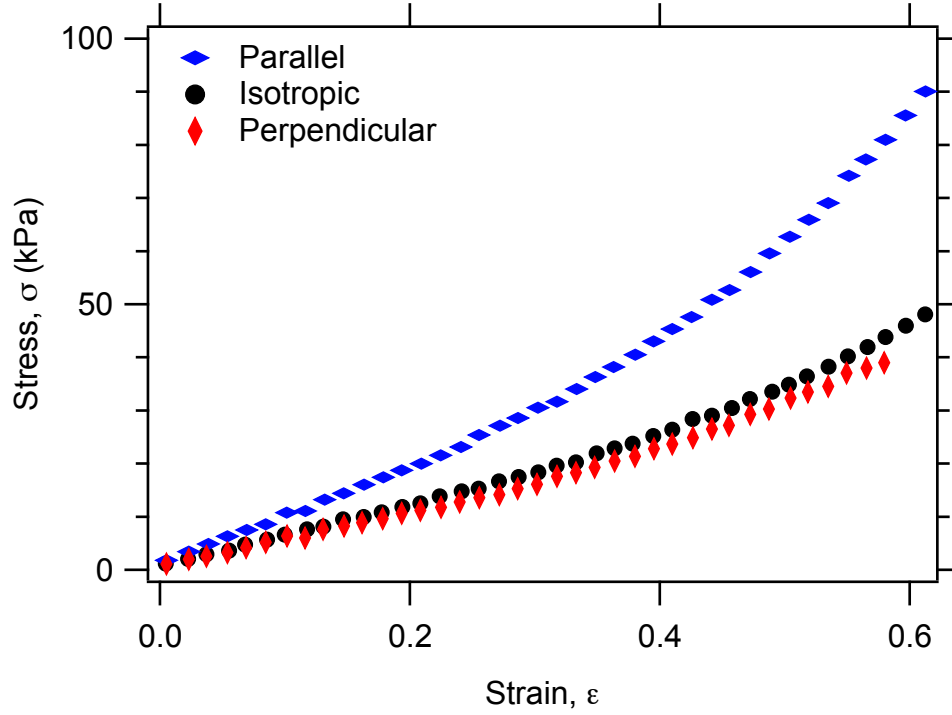


Figure 4.6: Engineering stress versus engineering strain for isotropic and anisotropic hydrogels produced with two thermal cycles.

is isotropic prior to relaxation. However, once the two networks are joined to act as an anisotropic network, neither appears isotropic after the compound anisotropic network is relaxed to equilibrium.

If $x_{1,0}$ is let to be the equilibrium fractional extension of strands in the isotropic base network prior to elongation, the equilibrium fractional extension of strands along the x direction after elongation by factor λ_p and relaxation by factor λ_r will be $u_{1,0} = \lambda_r \lambda_p x_{1,0}$. If $x_{2,0}$ is let to be the equilibrium fractional extension of strands in the reinforcement network prior to relaxation, the fractional extension of strands along the x direction after relaxation by factor λ_r , will be $u_{2,0} = \lambda_r x_{2,0}$. Due to symmetry, when the compound network is elongated or contracted in the x direction, it will contract or elongate equally in the y and z directions. Applying Eq. 4.10, the equilibrium fractional extension of strands in the y and z directions in the base network after elongation and relaxation is $v_{1,0} = x_{1,0} / \sqrt{\lambda_r \lambda_p}$ and the

equilibrium fractional extension of strands in the reinforcement network after relaxation is

$$v_{2,0} = x_{2,0} / \sqrt{\lambda_r}.$$

Therefore, the entropy of an anisotropic network constructed from two 3-chain networks is

$$\begin{aligned} S = & \frac{N_1}{3} \left[s(\lambda_x u_{1,0}) + s(\lambda_y v_{1,0}) + s(\lambda_z v_{1,0}) \right] \\ & + \frac{N_2}{3} \left[s(\lambda_x u_{2,0}) + s(\lambda_y v_{2,0}) + s(\lambda_z v_{2,0}) \right] \end{aligned} \quad (4.18)$$

where N_1 and N_2 are the number of polymer strands per cubic metre in the base and reinforcement networks, respectively. For deformations in the x direction, the strand entropies in the y and z directions are the same, and the engineering stress found using Eq. 4.7 is

$$\begin{aligned} \sigma_x = & -\frac{N_1 T}{3} \left[\frac{\partial s(x_{1,x})}{\partial x_{1,x}} \frac{\partial x_{1,x}}{\partial \lambda_x} + 2 \frac{\partial s(x_{1,y})}{\partial x_{1,y}} \frac{\partial x_{1,y}}{\partial \lambda_y} \frac{\partial \lambda_y}{\partial \lambda_x} \right] \\ & - \frac{N_2 T}{3} \left[\frac{\partial s(x_{2,x})}{\partial x_{2,x}} \frac{\partial x_{2,x}}{\partial \lambda_x} + 2 \frac{\partial s(x_{2,y})}{\partial x_{2,y}} \frac{\partial x_{2,y}}{\partial \lambda_y} \frac{\partial \lambda_y}{\partial \lambda_x} \right] \end{aligned}$$

where $x_{1,\alpha} = \lambda_x u_{1,0}$, $x_{1,y} = \lambda_y v_{1,0}$, $x_{2,\alpha} = \lambda_x u_{2,0}$, and $x_{2,y} = \lambda_y v_{2,0}$. The partial derivatives needed are

$$\begin{aligned} \frac{\partial s(x_{i,\alpha})}{\partial x_{i,\alpha}} &= -k_B n_i \mathcal{L}^{-1}(x_{i,\alpha}), \\ \frac{\partial x_{i,x}}{\partial \lambda_x} &= u_{i,0}, \\ \frac{\partial x_{i,y}}{\partial \lambda_y} &= v_{i,0}, \text{ and} \\ \frac{\partial \lambda_y}{\partial \lambda_x} &= \frac{\partial}{\partial \lambda_x} \left(\frac{1}{\sqrt{\lambda_x}} \right) = -\frac{1}{2\lambda_x^{3/2}}. \end{aligned}$$

Also, note that

$$v_{1,0} = \frac{u_{1,0}}{(\lambda_r \lambda_p)^{3/2}}$$

and

$$v_{2,0} = \frac{u_{2,0}}{\lambda_r^{3/2}}.$$

After substitution of the partial derivatives, the engineering stress for deformations parallel to the x direction is

$$\begin{aligned} \sigma_x(\lambda_x) = & \frac{N_1 k_B T n_1 u_{1,0}}{3} \left[\mathcal{L}^{-1}(\lambda_x u_{1,0}) - (\lambda_x \lambda_r \lambda_p)^{-3/2} \mathcal{L}^{-1}\left(\frac{v_{1,0}}{\sqrt{\lambda_x}}\right) \right] \\ & + \frac{N_2 k_B T n_2 u_{2,0}}{3} \left[\mathcal{L}^{-1}(\lambda_x u_{2,0}) - (\lambda_x \lambda_r)^{-3/2} \mathcal{L}^{-1}\left(\frac{v_{2,0}}{\sqrt{\lambda_x}}\right) \right]. \end{aligned} \quad (4.19)$$

As for the isotropic case, the sample is characterized by the fractional extension of strands at equilibrium and the effective modulus representing the limiting behaviour of a network made up of infinitely extensible Gaussian chains. The elastic moduli of the base and reinforcing networks, in the x direction, are

$$G_{1,x} = N_1 k_B T n_1 u_{1,0}^2 \quad (4.20)$$

and

$$G_{2,x} = N_2 k_B T n_2 u_{2,0}^2,$$

respectively. The elastic modulus of the combined anisotropic network, in the x direction, is $G_x = G_{1,x} + G_{2,x}$.

The y and z directions are equivalent for elongations perpendicular to the direction of the processing strain. In the following, the y direction is taken to be the direction of an applied stress. When the sample is extended in the y direction, it does not contract equally in the x and z directions. The dependent variables λ_x and λ_z could not be solved for analytically. Instead, λ_z is constrained using Eq. 4.10, the engineering stress is calculated by numerically differentiating Eq. 4.18, and λ_x is determined by numerically minimizing the stress for each

value of the independent variable λ_y . The elastic modulus for elongations in the y direction is $G_y = G_{1,y} + G_{2,y}$ where

$$G_{1,y} = N_1 k_B T n_1 v_{1,0}^2$$

and

$$G_{2,y} = N_2 k_B T n_2 v_{2,0}^2. \quad (4.21)$$

The two moduli of the base network, $G_{1,x}$ and $G_{1,y}$, and of the reinforcement network, $G_{2,x}$ and $G_{2,y}$, are not independent of each other. They may be written in terms of the independent moduli $G_1 = N_1 k_B T n_1 x_{1,0}^2$ and $G_2 = N_2 k_B T n_2 x_{2,0}^2$ of the base and reinforcing networks, respectively, that would be found were the two networks decoupled and allowed to relax to equilibrium. The relationships are $G_{1,x} = (\lambda_r \lambda_p)^2 G_1$, $G_{2,x} = \lambda_r^2 G_2$, $G_{1,y} = G_1 / \lambda_r \lambda_p$, $G_{2,y} = G_2 / \lambda_r$.

The anisotropic 3-chain model is simultaneously fit to experimental data for elongations parallel and perpendicular to the x direction to determine the four free parameters G_1 , G_2 , $x_{1,0}$, and $x_{2,0}$. After fitting, these parameters were used to calculate the moduli G_x , G_y , $G_{1,x}$, $G_{1,y}$, $G_{2,x}$, and $G_{2,y}$ and the equilibrium fractional extensions $u_{1,0}$, $v_{1,0}$, $u_{2,0}$, and $v_{2,0}$ given above. Engineering stress versus engineering strain, where points to the left of zero are perpendicular data and points to the right of zero are parallel data, and fits of the anisotropic 3-chain model are shown in Fig. 4.7.

8-Chain Model

The anisotropic 8-chain derivation is similar to the 3-chain derivation. As before, a base isotropic network is extended by factor λ_p , a reinforcement isotropic network is superimposed, and the compound anisotropic network is relaxed by factor λ_r parallel to the x direction. The entropy of the anisotropic network in this case is

$$S = N_1 s(\lambda_{1,\text{chain}} x_{1,0}) + N_2 s(\lambda_{2,\text{chain}} x_{2,0}) \quad (4.22)$$

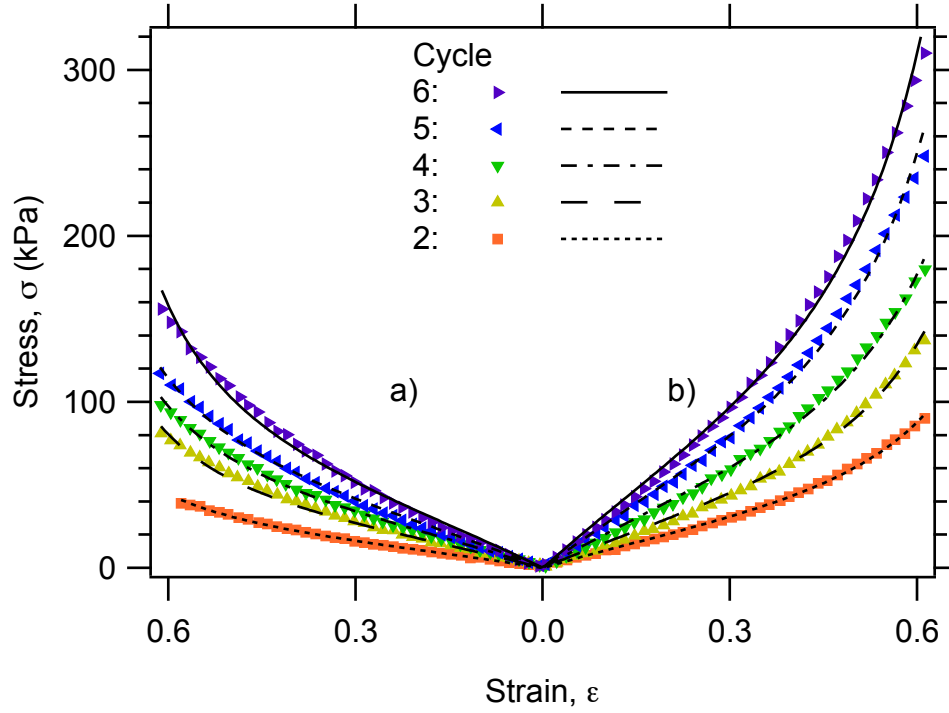


Figure 4.7: Engineering stress versus engineering strain for anisotropic hydrogels for uniaxial extension a) perpendicular and b) parallel to the processing strain with solid and dashed curves showing fits of the anisotropic 3-chain model. Points to the left of zero are perpendicular data (σ_y vs. ε_y) and points to the right of zero are parallel data (σ_x vs. ε_x).

where subscript indices 1 and 2 denote parameters belonging to the base and the reinforcement networks, respectively. The relationships between the fractional extension of the sample in the x direction, λ_x , and the fractional extensions of chains are

$$\lambda_{1,\text{chain}} = \sqrt{\frac{1}{3} \left[(\lambda_r \lambda_p \lambda_x)^2 + \frac{\lambda_y^2}{\lambda_r \lambda_p} + \frac{\lambda_z^2}{\lambda_r \lambda_p} \right]}$$

and

$$\lambda_{2,\text{chain}} = \sqrt{\frac{1}{3} \left[(\lambda_r \lambda_x)^2 + \frac{\lambda_y^2}{\lambda_r} + \frac{\lambda_z^2}{\lambda_r} \right]}.$$

The stress for deformations parallel to the x direction is

$$\sigma_x = -N_1 T \frac{\partial s(x_{1,\text{chain}})}{\partial x_{1,\text{chain}}} \frac{\partial x_{1,\text{chain}}}{\partial \lambda_{1,\text{chain}}} \frac{\partial \lambda_{1,\text{chain}}}{\partial \lambda_x} - N_2 T \frac{\partial s(x_{2,\text{chain}})}{\partial x_{2,\text{chain}}} \frac{\partial x_{2,\text{chain}}}{\partial \lambda_{2,\text{chain}}} \frac{\partial \lambda_{2,\text{chain}}}{\partial \lambda_x}.$$

In this case, each network contracts equally in the y and z directions so

$$\lambda_{1,\text{chain}} = \sqrt{\frac{1}{3} \left[(\lambda_r \lambda_p \lambda_x)^2 + \frac{2}{\lambda_r \lambda_p \lambda_x} \right]},$$

$$\lambda_{2,\text{chain}} = \sqrt{\frac{1}{3} \left[(\lambda_r \lambda_x)^2 + \frac{2}{\lambda_r \lambda_x} \right]}$$

and the stress is

$$\begin{aligned} \sigma_x = & \frac{N_1 k_B T n_1 \lambda_r \lambda_p x_{1,0}}{3} \frac{\mathcal{L}^{-1}(\lambda_{1,\text{chain}} x_{1,0}) \left[\lambda_r \lambda_p \lambda_x - (\lambda_r \lambda_p \lambda_x)^{-2} \right]}{\lambda_{1,\text{chain}}} \\ & + \frac{N_2 k_B T n_2 \lambda_r x_{2,0}}{3} \frac{\mathcal{L}^{-1}(\lambda_{2,\text{chain}} x_{2,0}) \left[\lambda_r \lambda_x - (\lambda_r \lambda_x)^{-2} \right]}{\lambda_{2,\text{chain}}}. \end{aligned} \quad (4.23)$$

Elongations perpendicular to the direction of the processing strain are chosen to be parallel to the y direction and, as for the 3-chain model, the sample does not contract by the same amounts in the x and z directions, preventing us from solving for the stress analytically. The numerical routines used for the 3-chain model are used to constrain λ_z using Eq. 4.10, find λ_x by maximizing the entropy, and differentiate the entropy to find stress.

The modulus coefficients in the 8-chain model are identical to those in the 3-chain model and the experimental data are again fit with four free parameters. The final analysis differs slightly from the 3-chain analysis because all of the chains in the base and reinforcing portions of the compound network have equilibrium fractional extensions

$$u_{1,0} = \sqrt{\frac{1}{3} \left[(\lambda_r \lambda_p)^2 + \frac{2}{\lambda_r \lambda_p} \right]} x_{1,0}$$

and

$$u_{2,0} = \sqrt{\frac{1}{3} \left[\lambda_r^2 + \frac{2}{\lambda_r} \right]} x_{2,0},$$

respectively. $G_{1,x}$, $G_{2,x}$, $G_{1,y}$, $G_{2,y}$, $u_{1,0}$, and $u_{2,0}$ are calculated after fitting. As for the 3-chain model, engineering stress versus engineering strain and fits of the anisotropic 8-chain model are shown with perpendicular data on the left and parallel data on the right in Fig. 4.8. Both the 3-chain and 8-chain anisotropic models are capable of simultaneously fitting the stress versus strain data for deformations parallel and perpendicular to the direction of the processing strain. Much like the isotropic models, the anisotropic models slightly over estimate the stress at small strains. At high strain, particularly for higher numbers of thermal cycles, both models have higher curvature than do the experimental data.

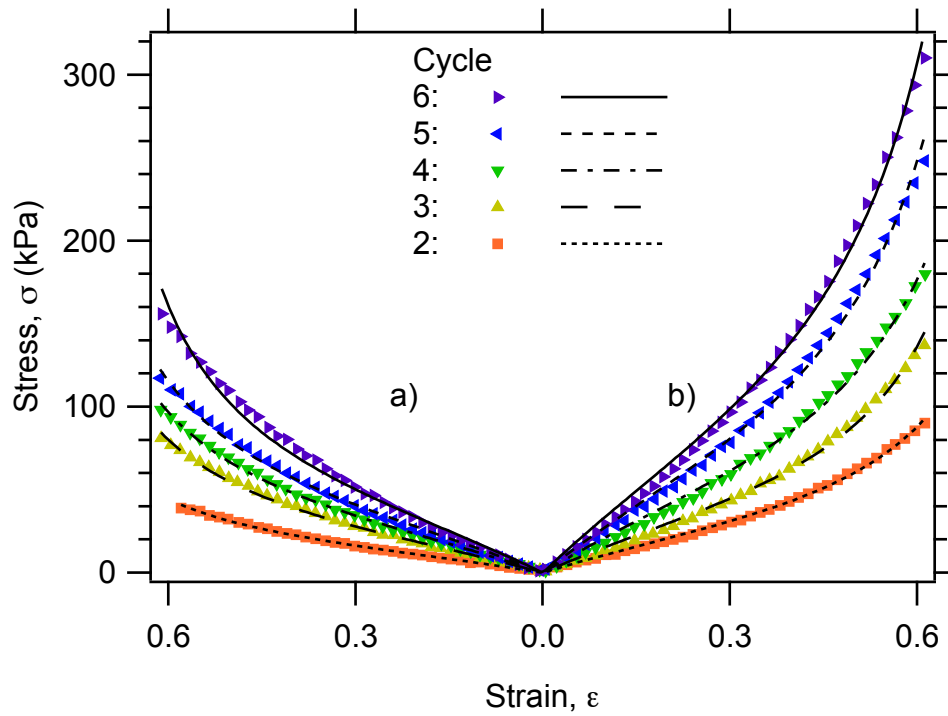


Figure 4.8: Engineering stress versus engineering strain for anisotropic hydrogels for uniaxial extension a) perpendicular and b) parallel to the processing strain with solid and dashed curves showing fits of the anisotropic 8-chain model. Points to the left of zero are perpendicular data (σ_y vs. ε_y) and points to the right of zero are parallel data (σ_x vs. ε_x).

4.3.5 Temperature Dependence of Stress Versus Strain

Eq. 4.14 predicts an effective modulus that is proportional to temperature. To test this dependence, 3-chain and 8-chain isotropic models were fit to uniaxial extension data obtained as a function of temperature to determine effective elastic moduli and equilibrium fractional extension versus temperature. The effective elastic moduli for the 3-chain and 8-chain models, together with solid lines which are proportional to temperature and fit to the data, are shown in Figs. 4.9 and 4.10, respectively. The equilibrium fractional extensions for the 3-chain and 8-chain models are shown in Figs. 4.11 and 4.12, respectively.

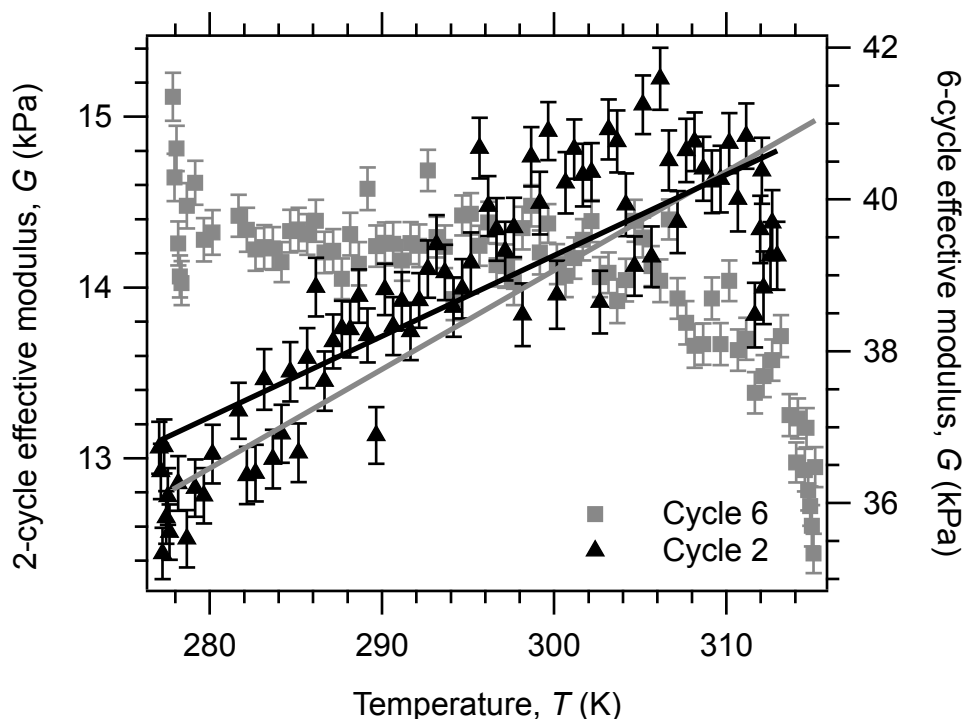


Figure 4.9: Effective elastic moduli of cycle-two and cycle-six PVA hydrogels as a function of temperature. Moduli were found by fitting the 3-chain isotropic model to uniaxial extension engineering stress versus engineering strain data. The black and grey solid lines are fits of a modulus proportional to temperature for the cycle-two and cycle-six data, respectively.

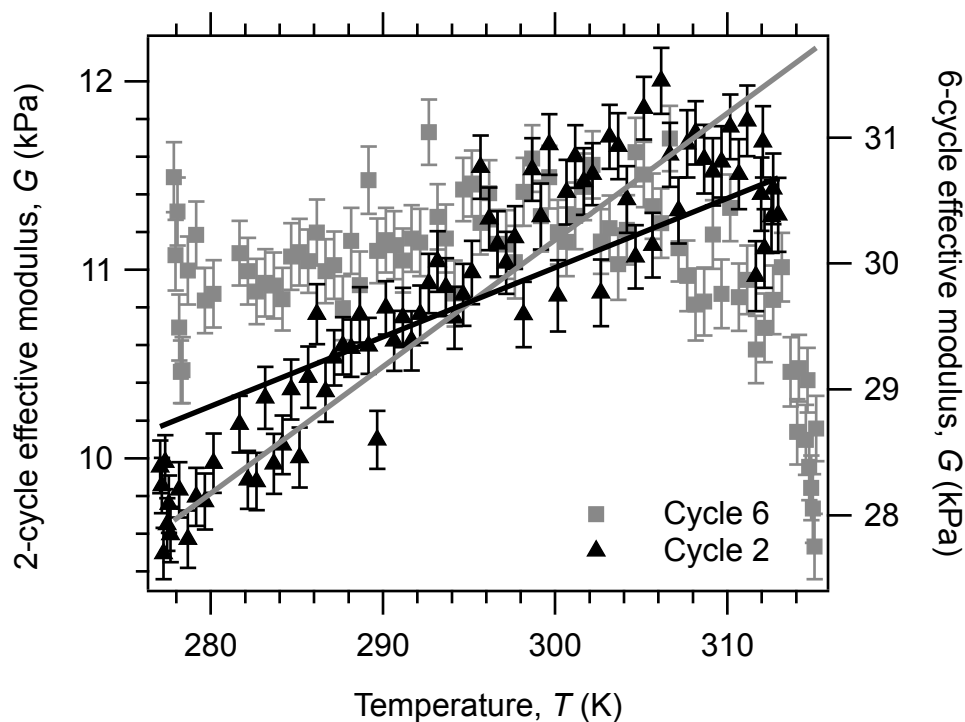


Figure 4.10: Effective elastic moduli of cycle-two and cycle-six PVA hydrogels as a function of temperature. Moduli were found by fitting the 8-chain isotropic model to uniaxial extension engineering stress versus engineering strain data. The black and grey solid lines are fits of a modulus proportional to temperature for the cycle-two and cycle-six data, respectively.

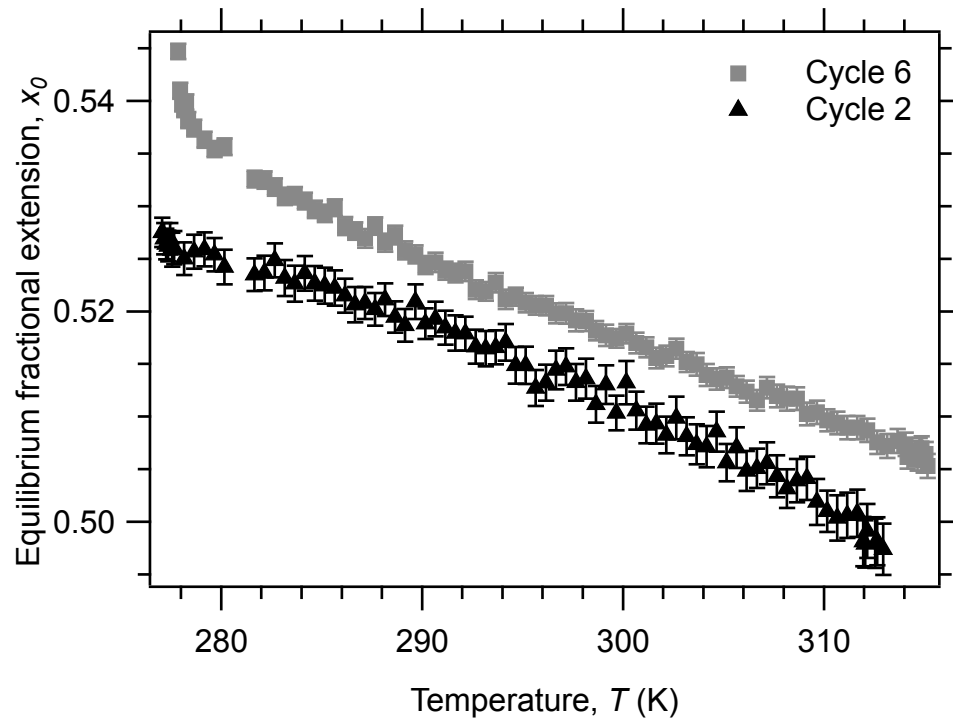


Figure 4.11: Equilibrium fractional extension of polymer strands in cycle-two and cycle-six PVA hydrogels as a function of temperature determined by fitting the 3-chain isotropic model to uniaxial extension engineering stress versus engineering strain data.

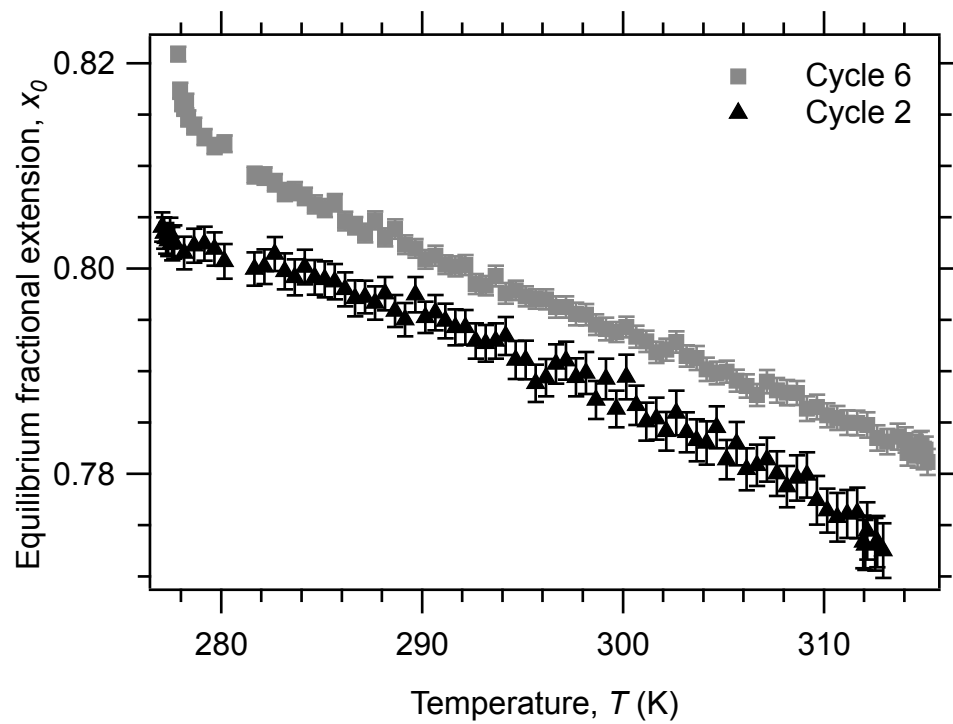


Figure 4.12: Equilibrium fractional extension of polymer strands in cycle-two and cycle-six PVA hydrogels as a function of temperature determined by fitting the 8-chain isotropic model to uniaxial extension engineering stress versus engineering strain data.

4.4 Discussion

4.4.1 Isotropic Hydrogels

Both the 3-chain and 8-chain models adequately fit the engineering stress versus engineering strain data of isotropic PVA hydrogels as shown in Figs. 4.3 and 4.5. The models perform best with fewer thermal cycles. At high strains, both models increase more rapidly than the experimental data.

One possible explanation for the difference is non-affine deformation of polymer strands with polydisperse lengths in the real hydrogel network. Though the 8-chain model features non-affine deformation of the polymer strands, they all have the same length and are forced to elongate at the same rate. In the real hydrogel, some strands will approach their maximum fractional extension sooner than others. When this occurs, these strands will henceforth deform by less than the assumed affine deformation. Meanwhile, strands that have not yet begun to stiffen will deform by more than the assumed affine deformation. As a result, the network as a whole will stiffen more gradually.

A second possible explanation is that as polymer strands become highly extended and their entropy decreases, it becomes energetically favourable for monomers to unreel from the crystallites at the ends of the strands [26–28]. This would increase the number of links in the strands and decrease their fractional extensions, resulting in strands that stiffen more gradually. Again, the entire network would stiffen more gradually.

The equilibrium fractional extensions of the polymer strands in the two models increase slightly during the first few thermal cycles as shown with black circles for the 3-chain and 8-chain models in Figs. 4.13 and 4.14, respectively. This may be caused by repeated thermal cycling inducing crystallites to consume some of the monomers comprising the strands between crystallites, increasing the size of crystallites produced by earlier cycles, without decreasing the distance between the crystallites.

Due to the non-affine extension of strands in the 8-chain model, strand equilibrium frac-

tional extensions increase more slowly as a function of strain. For strands in the isotropic 8-chain model to stiffen at low enough strain for the model to match the experimental data, they must start with a higher equilibrium fractional extension than the strands in the 3-chain model as seen in Figs. 4.13 and 4.14.

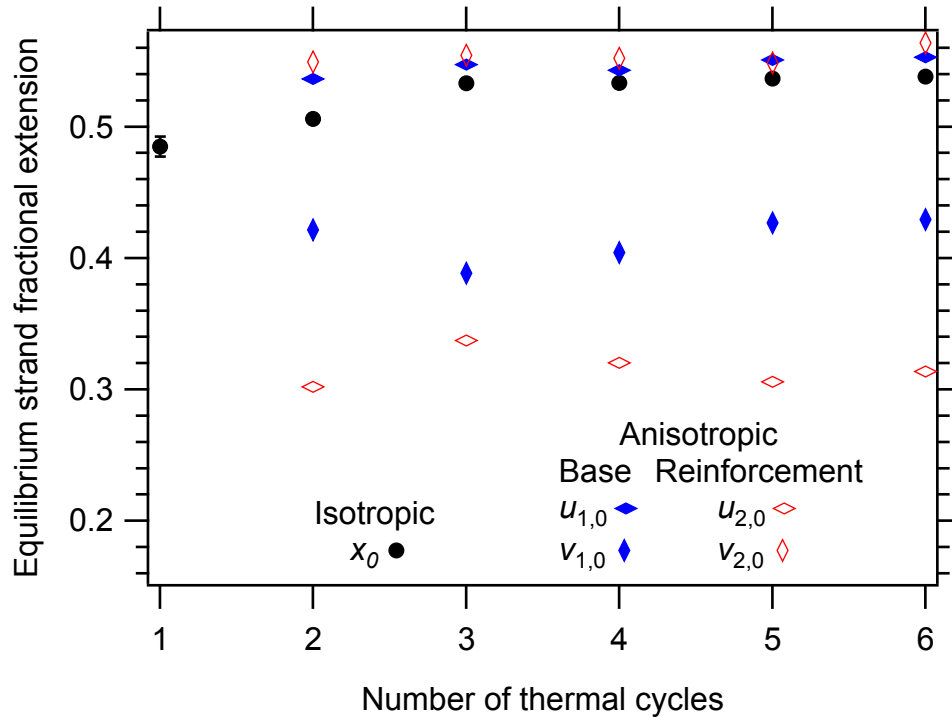


Figure 4.13: Equilibrium fractional extensions of strands for isotropic, x_0 , and anisotropic, $u_{1,0}$, $v_{1,0}$, $u_{2,0}$, and $v_{2,0}$, hydrogels determined by fitting the 3-chain model to experimental engineering stress versus engineering strain data. In the anisotropic model, $u_{1,0}$ and $v_{1,0}$ are fractional extensions of the base network and $u_{2,0}$ and $v_{2,0}$ are fractional extensions of the reinforcement network.

The effective elastic moduli obtained with the two models increase significantly with the number of thermal cycles as shown by the black circles for the 3-chain and 8-chain models in Figs. 4.15 and 4.16, respectively. The effective modulus depends on the number of strands per cubic metre, N , the number of random walk steps per strand, n , and the equilibrium fractional extension, x_0 , as given by Eq. 4.14. The slight increase in x_0 is

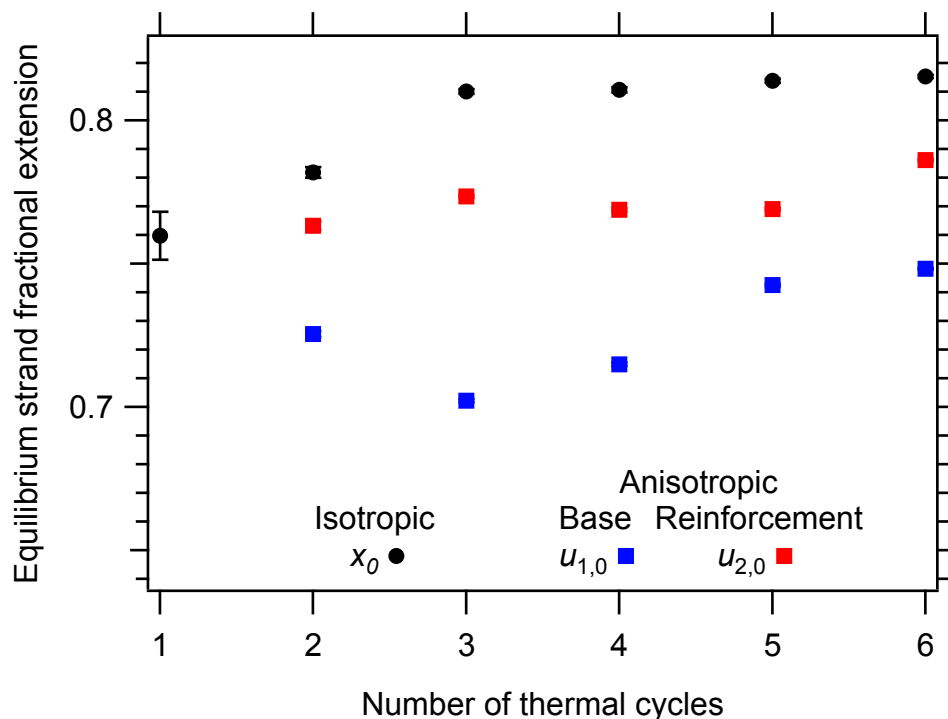


Figure 4.14: Equilibrium fractional extensions of strands for isotropic, x_0 , and anisotropic, $u_{1,0}$ and $u_{2,0}$, hydrogels determined by fitting the 8-chain model to experimental engineering stress versus engineering strain data.

insignificant and n for any given strand should decrease as crystallites grow, suggesting that the increase in effective modulus is almost entirely due to an increase in the number of strands per cubic metre participating in the network.

4.4.2 Anisotropic Hydrogels

Both models adequately fit the engineering stress versus engineering strain of anisotropic PVA hydrogels as shown in Figs. 4.7 and 4.8. As for the isotropic models, the fits are best at fewer thermal cycles and exhibit the same systematic error for higher numbers of thermal cycles as described above. To successfully fit the anisotropic data, the parameters characterizing the base networks of both models could not be fixed at the values obtained by fitting the corresponding isotropic models to cycle-one data. For both the 3-chain and

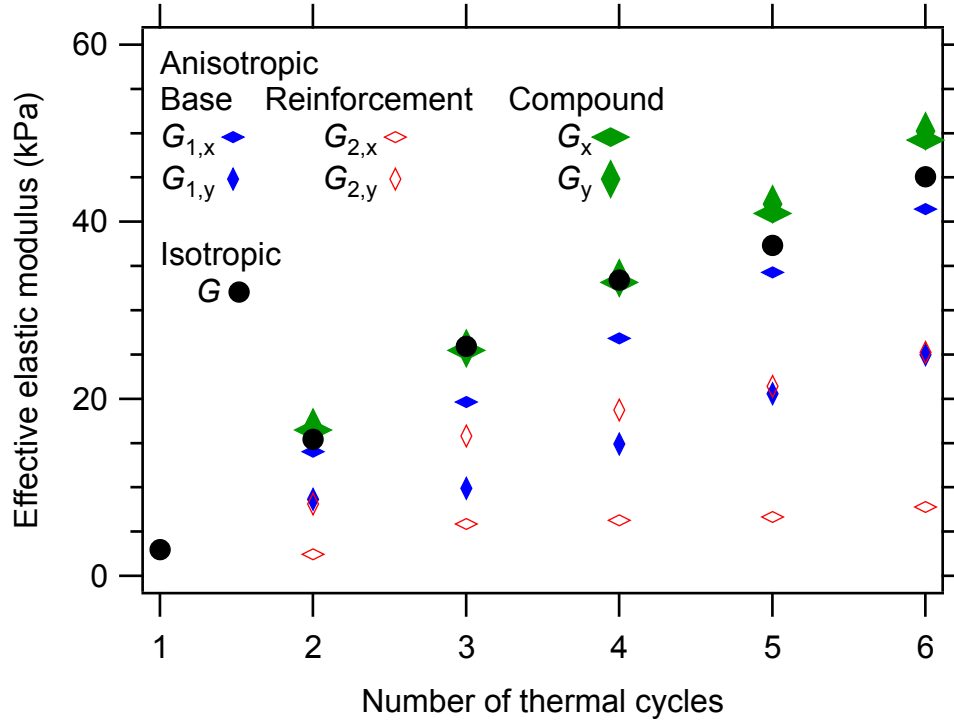


Figure 4.15: Effective elastic moduli for isotropic, G , and anisotropic hydrogels determined by fitting the 3-chain model to experimental engineering stress versus engineering strain data. In the anisotropic network, $G_{1,x}$ and $G_{1,y}$ are the moduli of the base network, $G_{2,x}$ and $G_{2,y}$ are the moduli of the reinforcement network, and G_x and G_y are the moduli of the compound network.

8-chain models, the effective moduli of the base and reinforcement networks increase with the number of thermal cycles as seen in Figs. 4.15 and 4.16. This suggests that the number of strands in the base network increases with the number of thermal cycles.

For both the 3-chain and 8-chain models, the effective elastic moduli in the x and y directions, G_x and G_y , are nearly identical as seen in Figs. 4.15 and 4.16. Therefore, the effective elastic moduli of the compound networks are not responsible for the anisotropy. It is noted that, by substituting the first order approximation $\mathcal{L}^{-1}(x) \approx 3x$ which is valid for small fractional extensions of strands into Eq. 4.19 or 4.23 at equilibrium, the relationship $G_x = G_y$ is obtained. Here, the equilibrium fractional extensions are less than, but not much

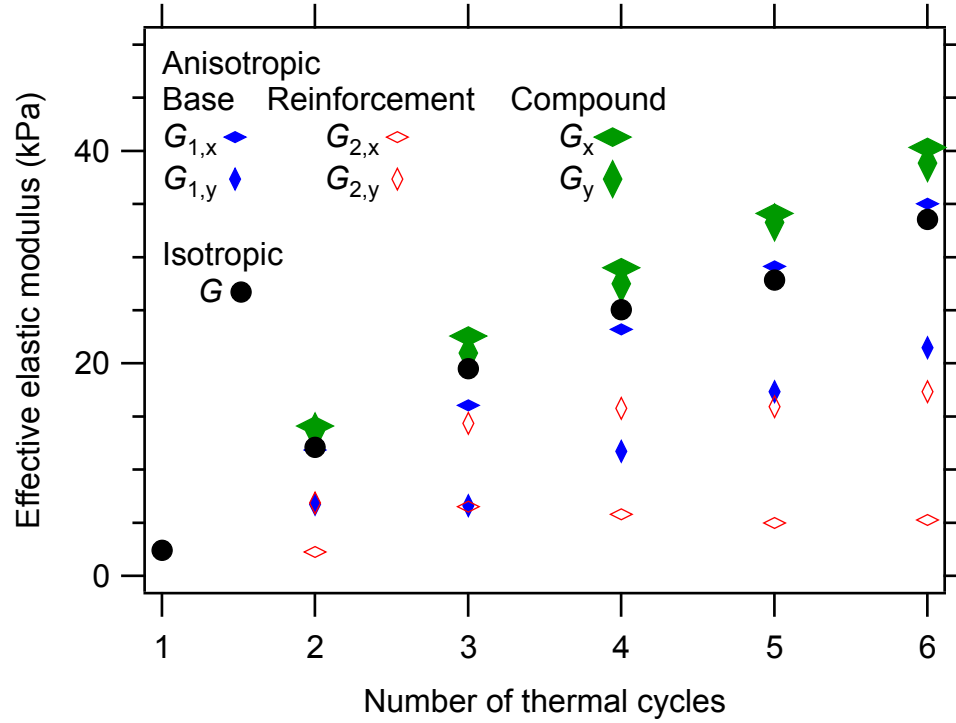


Figure 4.16: Effective elastic moduli for isotropic, G , and anisotropic hydrogels determined by fitting the 8-chain model to experimental engineering stress versus engineering strain data. In the anisotropic network, $G_{1,x}$ and $G_{1,y}$ are the moduli of the base network, $G_{2,x}$ and $G_{2,y}$ are the moduli of the reinforcement network, and G_x and G_y are the moduli of the compound network.

smaller than, one. Even so, the data show $G_x \approx G_y$.

As the 3-chain model is elongated, the importance of strands parallel to the direction of elongation increases as the strands stiffen and the importance of strands perpendicular to the direction of elongation diminishes as $1/\sqrt{\lambda}$. Therefore, the strands parallel to the x axis with equilibrium fractional extensions $u_{1,0}$ and $u_{2,0}$ are the most important for elongations in the x direction and the strands parallel to the y axis with equilibrium fractional extensions $v_{1,0}$ and $v_{2,0}$ are the most important for elongations in the y direction. Further, of strands aligned in the direction of elongation, those starting with higher equilibrium fractional extension will dominate the stress at high elongation because they stiffen first. Therefore, the

base network strands of equilibrium fractional extension $u_{1,0}$ dominate the stress for elongations along x and the reinforcement network strands of equilibrium fractional extension $v_{2,0}$ dominate the stress for elongations along y , as seen in Fig. 4.13. The figure also shows that the equilibrium fractional extensions of the dominant strands in the x and y directions, $u_{1,0}$ and $v_{2,0}$, are the same, and therefore not the source of the anisotropy. The compound network is anisotropic because the effective elastic modulus of the dominant strands in the x direction, $G_{1,x}$, is higher than the effective elastic modulus of the dominant strands in the y direction, $G_{2,y}$, as seen in Fig. 4.15. Since $u_{1,0}$ is approximately equal to $v_{2,0}$, Eqs. 4.20 and 4.21 show that $G_{1,x}$ is greater than $G_{2,y}$ because N_1 is greater than N_2 . There are more highly extended strands in the x direction than in the y direction.

In the 8-chain model, all strands in the base network have the same fractional extension and all strands in the reinforcement network have the same fractional extension. When the compound network is in equilibrium, the fractional extension of strands in the reinforcement network is slightly higher than in the base network as shown in Fig. 4.14. However, if the network begins to elongate in the x direction, the fractional extension of polymer strands in the base network will immediately begin to increase, while the fractional extension of polymer strands in the reinforcement network will decrease to a minimum at $\lambda_x = 1/\lambda_r$ before increasing. At this time, the strands in the base network will have higher fractional extension and will dominate the stress. Similarly, for elongations of the network in the y direction, the equilibrium fractional extension of strands will always increase in the reinforcement network and initially decrease before increasing in the base network. Therefore, the strands of the reinforcement network dominate the stress for elongations in the y direction. Similar to the 3-chain model, the network is stronger in the x direction because the modulus of the dominant strands for deformation in the x direction, $G_{1,x}$, is higher than for the dominant strands for deformations in the y direction, $G_{2,y}$, as seen in Fig. 4.16. Much like the 3-chain model, there are more highly extended strands that immediately elongate for deformations in the x direction than for the y direction.

4.4.3 Temperature Dependence of Stress Versus Strain

The effective moduli of the cycle-two hydrogel, as determined from the 3-chain and 8-chain models, increases with temperature at a rate equal to or greater than the expected proportional dependence, assuming the network is unaltered, as shown in Figs. 4.9 and 4.10, respectively. However, the effective moduli of the cycle-six hydrogel remain constant or increases at less than the expected rate. The equilibrium fractional extensions decrease slightly with increasing temperature as shown in Figs. 4.11 and 4.12. This could be caused by monomers leaving crystallites and increasing the average number of monomers per strand or by water leaving the network and decreasing the distance between cross-links. The decrease in the equilibrium fractional extension lowers the effective modulus but is not sufficient to explain the discrepancy between actual cycle-six moduli and the expected moduli. Eq. 4.14 predicts that the number of strands per cubic metre, N , and/or the number of links per strand, n , must also be decreasing with temperature. All hydrogels show a decrease in modulus at the warmest temperatures. This may be caused by partial melting of crystallites which reduces the number of cross-links and thus the number of polymer strands contributing to the entropy, weakening the network.

4.4.4 Connection Between Structural and Mechanical Models

In Chapter 3, the structure was modelled as a fractal aggregate composed of polymer blobs. Here, the compatibility of the previous isotropic structural model and this isotropic 3-chain mechanical model is evaluated. It is assumed that each blob contains one crystallite and dangling chains associated with it, that blobs are packed closely together, and that blobs connect to their immediate neighbours with one or more polymer strands. Under these assumptions, the equilibrium length of strands that connect blobs, r_0 , is comparable to the size of the blobs, R , which was earlier found to have the average value of 46.8 nm from Table 4.2. Finally, it is assumed that the blob size is smaller for cycle-one because the blobs

Table 4.3: Estimates of the number of links per strand n_K , the number of strands per cubic metre N , and the percentage of monomers contained in strands that contribute to network strength.

Number of thermal cycles	n_K	$N (\times 10^{23}/\text{m}^3)$	monomers in strands (%)
1	156	0.19	0.5
2	149	0.94	2.5
3	142	1.50	3.8
4	142	1.94	4.9
5	141	2.15	5.4
6	140	2.59	6.4

are not fully formed, and not that the strands are shorter than for later thermal cycles.

The statistical theory for the entropy of polymer strands assumes freely jointed links. PVA is not freely jointed due to the constraint on carbon-carbon bond angles. However, it is possible to divide a polymer chain into fewer, longer links such that the orientations of the links are uncorrelated and the links may be considered freely jointed. The length of each link at which a chain may be considered freely jointed is known as the Kuhn length and has been measured to be 6.2 \AA for PVA [29]. PVA strands are therefore replaced with equivalent freely jointed strands having n_K freely jointed links of Kuhn length $b_K = 6.2 \text{ \AA}$. It is now possible to estimate the number of links between the two ends of a polymer strand using $n_K = r_0/x_0 b_K$, the number of strands per cubic metre from Eq. 4.14, and the total number of Kuhn lengths per cubic metre from $N n_K$. Finally, each Kuhn length is equivalent to 2.47 monomers, allowing calculation of the number of monomers per cubic metre which make up the strands as a percentage of the total number of monomers per cubic metre in the hydrogel. The results obtained by using G and x_0 from the isotropic 3-chain model are shown in Table 4.3.

The modelling suggests that less than 10% of the polymer present in the sample contributes to the tensile strength. It is also estimated that, prior to cross-linking, there are 3.7×10^{23} polymer chains per cubic metre. Though each polymer chain could be cross-linked many times and be divided into multiple polymer strands, the number of polymer chains per cubic metre remains comparable to, but larger than, the number of strands per cubic metre as determined in Table 4.3. Therefore, the amount of polymer required to obtain the observed mechanical properties, as estimated from the structural and mechanical models, is compatible with the amount of polymer available in the hydrogels. Further, the models suggest that only a small percentage of the monomers in the sample are contained in the strands that contribute to mechanical strength via connections to neighbouring blobs.

To create a continuous, three-dimensional network, each blob must connect to several neighbouring blobs. The unit cell of the 3-chain model has volume r_0^3 and the volume fraction of the gel phase made of strands can be estimated from $(N/3)r_0^3$. This estimate yields a volume fraction increasing from 0.7 to 9 with the number of thermal cycles. Since the volume fraction must be less than one, strands in the real hydrogel must be packed more tightly than in the 3-chain unit cell. To achieve this without decreasing the average distance between PVA blobs requires multiple connections between connected crystallite pairs. In the case of the 3-chain network, connected pairs would require roughly a single connection for cycle-one and roughly twenty connections for cycle-six to achieve a volume fraction of 50% polymer-free pores.

4.5 Conclusion

The uniaxial extension behaviour of PVA hydrogels has been successfully modelled using the 3-chain model of Treloar [13] and the 8-chain model of Arruda and Boyce [14]. Anisotropic versions of the models were developed to provide insight into the origin of anisotropy in the stress-strain behaviour of PVA hydrogels produced by stretching a weak

cycle-one gel parallel to the x direction and performing additional thermal cycles. These anisotropic gels are stronger when elongated in the x direction than in the y or z directions.

The mechanical models are much simpler than structure observed by SANS and could be made to more closely resemble the structural model, but they exhibit nonlinear and anisotropic behaviour closely matching the experimental data. Although the large-scale fractal aggregate structure was not considered and was not needed to explain the stress-strain relationships or the anisotropy, the possibility that it plays a role has not been excluded. For each number of thermal cycles, there is more than sufficient polymer available for entropy to account for the measured mechanical strength.

The observed strain stiffening of the bulk material is adequately explained by the stiffening of polymer strands as they become highly extended. The stress of an anisotropic PVA hydrogel is dominated by the polymer strands parallel to the direction of the strain that have the highest equilibrium fractional extension. In the 3-chain model, the number of strands with high fractional extension in the x direction outnumber those in the y direction, making it stronger in the x direction than in the y direction. In the 8-chain model, strands undergo non-affine deformation, but similarly to the 3-chain model, there are more strands of high fractional extension for elongations in the x direction than in the y direction.

To test that entropy is the dominant source of elasticity, the effective moduli of cycle-two and cycle-six hydrogels were found as a function of temperature. According to both the 3-chain and 8-chain models, the effective modulus of the cycle-two hydrogel increased with temperature at or slightly above the expected rate. However, the effective modulus of the cycle-six hydrogel remains approximately constant through most of the temperature range and at the warmest temperatures, both hydrogels rapidly weaken. The lack of dependence on temperature for the cycle-six hydrogel and the weakening at high temperature for both hydrogels may be due to unreeling of monomers from the cross-links. As unreeling progresses, strands connecting cross-links may eventually detach.

4.6 Bibliography for Chapter 4

1. Peppas, N. A. "Turbidimetric studies of aqueous poly(vinyl alcohol) solutions." *Makromol. Chem.* **176**, 3433–3440 (1975).
2. Lozinsky, V. I. *et al.* "Study of cryostructurization of polymer systems VII. Structure formation under freezing of poly(vinyl alcohol) aqueous solutions." *Colloid. Polym. Sci.* **264**, 19–24 (1986).
3. Trieu, H. & Qutubuddin, S. "Poly(vinyl alcohol) hydrogels: 2. Effects of processing parameters on structure and properties." *Polym.* **36**, 2531–2539 (1995).
4. Yokoyama, F., Masada, I., Shimamura, K., Ikawa, T. & Monobe, K. "Morphology and structure of highly elastic poly(vinyl alcohol) hydrogel prepared by repeated freezing-and-melting." *Coll. Polym. Sci.* **264**, 595–601 (1986).
5. Millon, L. E. & Wan, W. K. "The Polyvinyl Alcohol-Bacterial Cellulose System As a New Nanocomposite for Biomedical Applications." *J. Biomed. Mater. Res. Part B: Appl. Biomater.* **79B**, 245–253 (2006).
6. Tong, X., Zheng, J., Lu, Y., Zhang, Z. & Cheng, H. "Swelling and mechanical behaviors of carbon nanotube/poly (vinyl alcohol) hybrid hydrogels." *Mater. Lett.* **61**, 1704–1706 (2007).
7. Millon, L. E., Guhados, G. & Wan, W. "Anisotropic Polyvinyl Alcohol – Bacterial Cellulose Nanocomposite for Biomedical Applications." *J. Biomed. Mater. Res. B: Appl. Biomater.* **86B**, 444–452 (2008).
8. Wan, W. K., Campbell, G., Zhang, Z. F., Hui, A. J. & Boughner, D. R. "Optimizing the Tensile Properties of Polyvinyl Alcohol Hydrogel for the Construction of a Bioprosthetic Heart Valve Stent." *J. Biomed. Mater. Res.* **63**, 854–861 (2002).
9. Millon, L. E., Mohammadi, H. & Wan, W. K. "Anisotropic Polyvinyl Alcohol Hydrogel for Cardiovascular Applications." *J. Biomed. Mater. Res. Part B: Appl. Biomater.* **79B**, 305–311 (2006).
10. Millon, L. E., Nieh, M.-P., Hutter, J. L. & Wan, W. "SANS Characterization of an Anisotropic Poly(vinyl alcohol) Hydrogel with Vascular Applications." *Macromol.* **40**, 3655–3662 (2007).
11. Hudson, S. D. *et al.* "Characterization of anisotropic poly(vinyl alcohol) hydrogel by small- and ultra-small-angle neutron scattering." *J. Chem. Phys.* **130**, 034903:1–9 (2009).

12. Landau, L. D. & Lifshitz, E. M. *Theory of elasticity, 2nd Ed.* (Pergamon Press, 1970).
13. Treloar, L. R. G. *The physics of rubber elasticity* (Oxford University Press, USA, 2005).
14. Arruda, E. M. & Boyce, M. C. "A Three-dimensional constitutive model for the large stretch behavior of rubber elastic materials." *J. Mech. Phys. Solids* **41**, 389–412 (1993).
15. Boyce, M. C. & Arruda, E. M. "Constitutive Models of Rubber Elasticity: A Review." *Rubber Chem. Technol.* **73**, 504–523 (2000).
16. Mohammadi, H., Boughner, D., Millon, L. E. & Wan, W. K. "Design and simulation of a poly(vinyl alcohol) bacterial cellulose nanocomposite mechanical aortic heart valve prosthesis." *P. I. Mech. Eng. H* **223**, 697–711 (2009).
17. Mooney, M. "A Theory of Large Elastic Deformation." *J. Appl. Phys.* **11**, 582–592 (1940).
18. Rivlin, R. S. "Large Elastic Deformations of Isotropic Materials. IV. Further Developments of the General Theory." *Phil. Trans. R. Soc. Lond. A* **241**, 379–397 (1948).
19. Shibayama, M. *et al.* "Small-angle neutron scattering from poly(vinyl alcohol)-borate gels." *Polym.* **33**, 2883–2890 (1992).
20. Chen, S.-H. & Teixeira, J. "Structure and Fractal Dimension of Protein-Detergent Complexes." *Phys. Rev. Lett.* **57**, 2583–2586 (1986).
21. Horkay, F., Hecht, A.-M., Mallam, S., Geissler, E. & Rennie, A. R. "Macroscopic and Microscopic Thermodynamic Observations in Swollen Poly(vinyl acetate) Networks." *Macromol.* **24**, 2896–2902 (1991).
22. Glinka, C. J. *et al.* "The 30 m Small-Angle Neutron Scattering Instruments at the National Institute of Standards and Technology." *J. Appl. Cryst.* **31**, 430–445 (1998).
23. Choi, S.-M., Barker, J. G., Glinka, C. J., Cheng, Y. T. & Gammel, P. L. "Focusing cold neutrons with multiple biconcave lenses for small-angle neutron scattering." *J. Appl. Cryst.* **33**, 793–796 (2000).
24. Mildner, D. F. R., Hammouda, B. & Kline, S. R. "A refractive focusing lens system for small-angle neutron scattering." *J. Appl. Cryst.* **38**, 979–987 (2005).
25. Kline, S. R. "Applied Reduction and analysis of SANS and USANS data using IGOR Pro." *J Appl. Cryst.* **39**, 895 (2006).
26. Nishinari, K., Koide, S. & Ogino, K. "On the temperature dependence of elasticity of thermo-reversible gels." *J. Phys. France* **46**, 793–797 (1985).

27. Higgs, P. G. & Ball, R. C. "Some Ideas Concerning the Elasticity of Biopolymer Networks." *Macromolecules* **22**, 2432–2437 (1989).
28. Kawai, S., Nitta, Y. & Nishinari, K. "Model study for large deformation of physical polymeric gels." *J. Chem. Phys.* **128**, 134903:1–9 (2008).
29. Li, H. *et al.* "Single molecule force spectroscopy on poly(vinyl alcohol) by atomic force microscopy." *Macromol. Rapid Commun.* **19**, 609–611 (1998).

Chapter 5

Measurement of the Elastic Modulus of Spider Mite Silk Fibres Using the Atomic Force Microscope

5.1 Introduction

Silk is an exceptionally strong natural material produced by spiders, silkworms, spider mites, and many other creatures. Natural silkworm silk has long been exploited for textiles and, more recently, suture materials [1–3]. Silk also shows promise as a scaffold material for tissue repair and for generation of artificial tissue [2–4]. For this reason, there is great interest in characterizing the physical, chemical, and biological properties of silk, and in producing synthetic silk fibres. However, the properties of artificially produced fibres are usually inferior to those of their natural counterparts [5]. Further, the properties of natural and artificial silk fibres vary considerably and depend on the silk proteins utilized, temperature, degree of hydration, and rate of deformation [6].

Due to the scale of lengths and magnitude of forces involved, atomic force microscopy (AFM) is well suited to measuring the mechanical properties of silk fibres. The atomic

force microscope can be used to measure the mechanical properties of nanofibres by suspending the fibres over trenches and pushing on them laterally or vertically with the tip of an atomic force microscope cantilever, thus performing a three-point bending test. This technique has been used on a variety of materials including Au, Si, SiO₂, TiO₂, and ZnO nanowires [7–11]; carbon nanotubes [12–14]; and cellulose and assorted polymer nanofibres [7, 15–18]. In some cases, elastic moduli that increased with decreasing nanofibre or nanowire diameter were reported [17, 19]. However, Heidelberg *et al.* showed that tensile stress, due to elongation of a deformed fibre, must be considered when the lateral displacement of the fibre is comparable to or larger than its radius [9]. In the cases of Si and ZnO nanowires, deformation-induced tensile stress could fully explain the apparent increase in modulus with decreasing nanowire diameter, and the moduli were found to equal the bulk moduli of Si and ZnO [9, 11].

Recently, the *Tetranychus urticae* spider mite genome was fully sequenced, the proteins involved in silk production were identified, and a summary of the mechanical results presented here were published, clearing the way for production and characterization of spider mite silks with genetically tailored mechanical properties [20]. To model the AFM data and determine the Young's modulus of the fibres, the model of Heidelberg *et al.* described above had to be modified to account for an initial axial tension which is present in the absence of applied forces from the AFM cantilever tip. Here, a detailed account of the AFM technique used and the derivation of the model used to determine the Young's modulus from force versus lateral displacement of suspended fibres.

5.2 Materials and Methods

Trenches were fabricated on silicon substrates, using a custom-designed mask produced at the University of Alberta NanoFab facility (Edmonton, Canada), by photolithography and reactive ion etching at the Western Nanofabrication Facility (London, Canada). Silk fibres

were deposited by allowing adult and larval *Tetranychus urticae* spider mites to walk on the silicon wafers for two to eight hours. Before performing measurements on the fibres, spider mites were removed from the silicon wafers with a fine brush. To reduce the time needed to find single fibres crossing trenches, areas of spider mite activity were located by searching for bundles of fibres using an optical microscope.

AFM measurements were made using a Multimode atomic force microscope with a Nanoscope IIIa controller using control software version 5.30 (Digital Instruments, Santa Barbara, CA). NP-S silicon nitride cantilevers (Veeco, Plainview, NY) with nominal spring constants of 0.06 N/m and 0.35 N/m were used for measurements on larval and adult fibres, respectively. Actual spring constants of 0.083 ± 0.003 N/m and 0.347 ± 0.009 N/m were measured using the thermal noise method [21–24]. Measurements were performed at an ambient atomic force microscope temperature of approximately 32 °C and relative humidities of 14–30%, though the relative humidity was usually less than 20%.

Single silk fibres and bundles of several fibres were located by performing large-area, high-speed contact AFM imaging on flat areas in the vicinity of the large fibre bundles located with the optical microscope. Contact imaging was used to track fibres to trenches, to verify that each fibre was firmly stuck to the plateau on each side of the trench, to measure the fibre lengths and diameters, and, in a few cases, to deliberately break fibres after acquiring force-volume data.

Once located, mechanical testing of fibres was performed by measuring force curves. A force curve records cantilever deflection versus the vertical position of the sample under the cantilever. Force-volume (FV) data are comprised of a matrix of force curves acquired over an area. For each force curve, a relative trigger instructs the atomic force microscope to retract the sample when the cantilever deflection reaches a trigger threshold value, ensuring a consistent range of forces at each point. Here, FV data of 64×64 force curves were captured where fibres crossed the gratings. Image sizes large enough to capture force curves over the entire length of suspended fibres and on the plateaus at both ends were selected.

Each force curve was acquired using a vertical ramp of $1\ \mu\text{m}$, a scan rate of 4 Hz, and a relative trigger threshold of approximately 250 nm or less. Height images can be created from FV data by constructing a map of the vertical piezoelectric scanner position at which each force spectrum reaches the trigger threshold value. Example contact and FV height images of the same fibre are shown in Figs. 5.1 and 5.2, respectively.

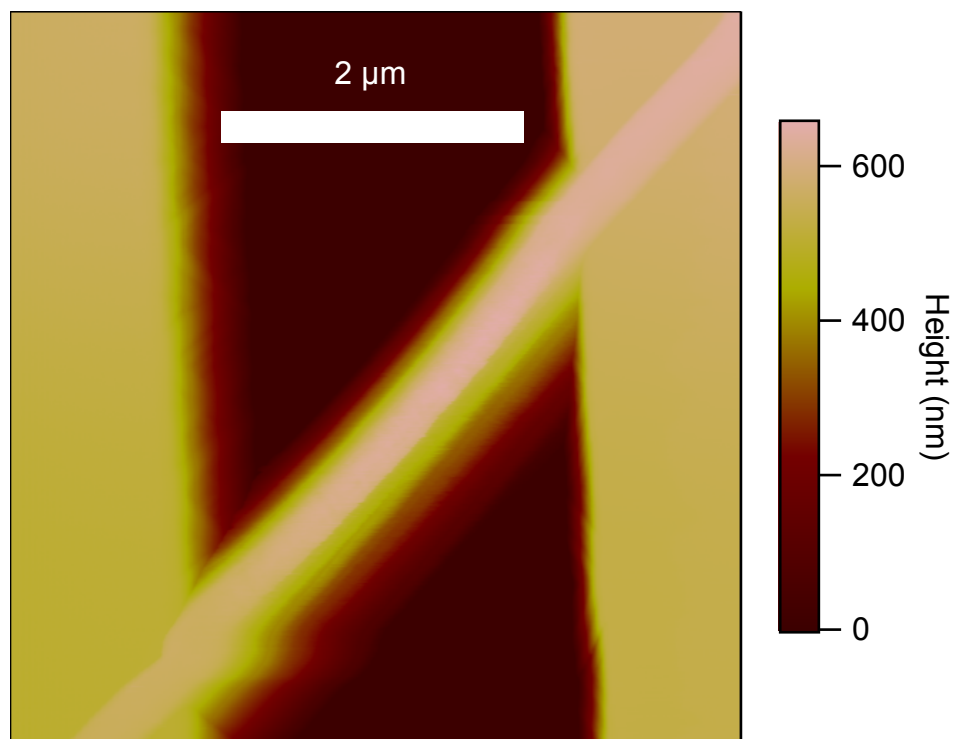


Figure 5.1: $5.3\ \mu\text{m} \times 5.3\ \mu\text{m}$ contact AFM image of a spider mite silk fibre suspended over a trench. The bottom of the trench has been moved off-scale in order to highlight the edges of the trench and the fibre. The fibre appears much wider than its true diameter due to convolution with the pyramidal AFM tip.

5.3 Theory and Data Analysis

An AFM three-point bending test measures fibre restoring force versus fibre deflection at the point where the cantilever tip touches the fibre. These data are modelled by finding the

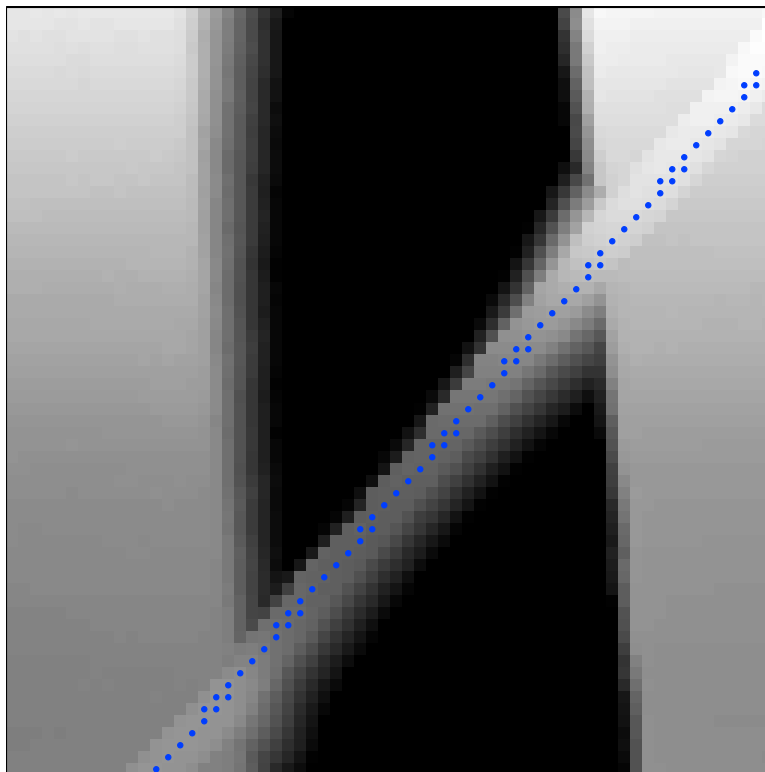


Figure 5.2: AFM FV height image of the same spider mite silk fibre shown in Fig. 5.1. The bottom of the trench has been moved off-scale in order to highlight the edges of the trench and the fibre. The grey scale for each pixel represents the trigger point of the force curve recorded at that location. The circles indicate the locations of force curves on the fibre chosen for analysis.

mechanical equilibrium of model fibres and calculating the expected restoring force versus displacement. The restoring force results from a combination of bending, shear, and tensile stresses. However, when the aspect ratio (length divided by diameter) of a fibre is much greater than one, the shear stress is negligible in comparison to the bending stress [25]. As this is the case here, shear stress is not considered in the analysis below.

The material is assumed to be linearly elastic for axial strains. Further, the radius of curvature due to deformation is assumed to be large relative to the fibre diameter everywhere on the fibre, which is satisfied for fibre displacements much smaller than the length of the fibre. To simplify the analysis, only the case when the cantilever tip pushes at the

centre of the fibre is considered. Below, the models which account for bending only and bending with deformation-induced tension are reviewed, and a model which accounts for bending, deformation-induced tension, and an initial tension is derived.

5.3.1 Pure Bending

For deformations much smaller than the radius of the fibre, tensile stress caused by elongation may be neglected [9] and, in the absence of an initial tension, deformation can be adequately modelled by considering bending alone, so that

$$EI \frac{d^3 \delta(x)}{dx^3} = -\frac{F_{\text{centre}}}{2}, \quad (5.1)$$

where x is the position along the fibre, E is the Young's modulus of the fibre, and I is the area moment of inertia of the fibre [26]. With clamped boundary conditions, and noting that the solution must be symmetric about the centre, the solution must satisfy

$$\delta(0) = 0$$

and

$$\delta'(0) = \delta'(L_0/2) = 0,$$

where L_0 is the length of fibre between the clamped boundaries. The solution, after isolation of the magnitude of the force at the centre, F_{centre} , is

$$F_{\text{centre}} = \frac{192EI}{L_0^3} \delta_{\text{centre}} \quad (5.2)$$

where δ_{centre} is the displacement of the fibre at the centre [26]. The fibre is shown in Fig. 5.3. Here, in the absence of an initial tension, $T_0 = 0$, $L_{\text{eq}} = L_0$, and the deformation induced tension T is assumed to be negligible.

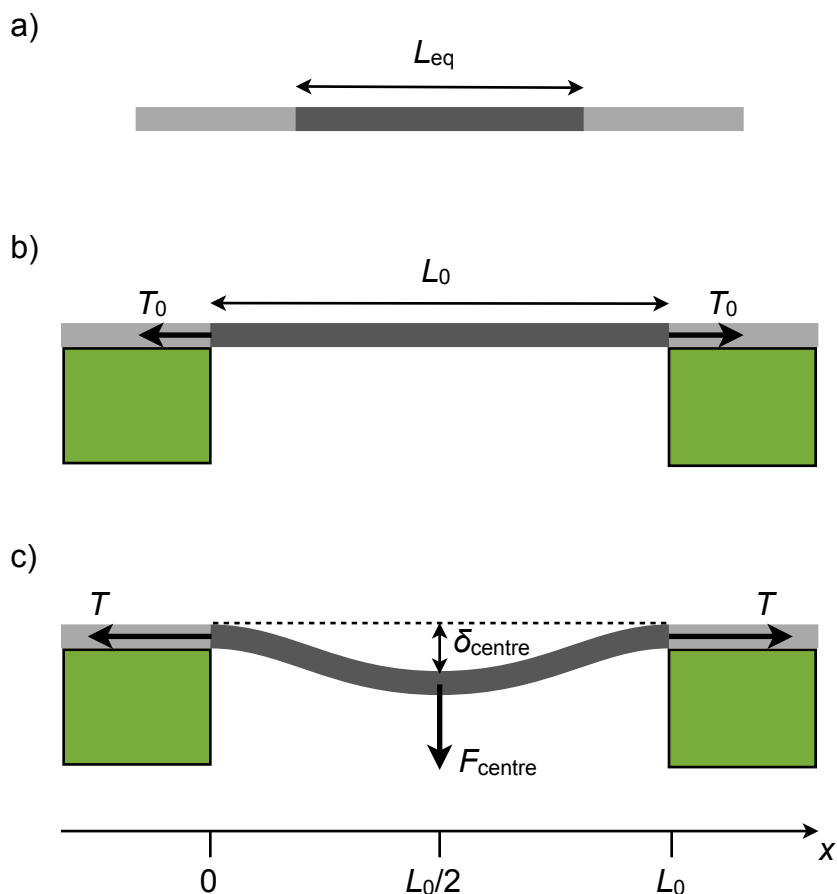


Figure 5.3: Diagram of the segment of fibre under analysis a) before clamping and without initial tension, b) after application of initial tension and clamping to grating but before contact with AFM cantilever tip, and c) after contact with AFM cantilever tip. The fibre is shown in grey and the segment under analysis is dark grey. L_{eq} is the equilibrium length before application of an initial tension. L_0 is the distance between the clamping points. T_0 is the magnitude of the initial tension. T is the sum of the initial tension and the tension due to elongation of the fibre. δ_{centre} is the displacement of the centre of the fibre when the cantilever tip exerts a force of magnitude F_{centre} at the centre.

5.3.2 Bending With Deformation-Induced Tension

For deformations comparable to or larger than the fibre radius, the tensile stress caused by elongation becomes significant [9]. When an axial tension of magnitude T is present, the vertical components of the tension in infinitesimal elements of the fibre act as shear forces on the ends of the elements. In the small deflection limit where the slope of the fibre remains small, the vertical component of the tension at position x is $Td\delta(x)/dx$ and new equation for equilibrium of the fibre becomes [26]

$$EI \frac{d^3 \delta(x)}{dx^3} = -\frac{F_{\text{centre}}}{2} + T \frac{d\delta(x)}{dx}. \quad (5.3)$$

Heidelberg *et al.* solved Eq. 5.3 for clamped boundary conditions and obtained the relationship

$$F_{\text{centre}} = \frac{192EI}{L_0^3} f(\alpha) \delta_{\text{centre}} \quad (5.4)$$

where

$$f(\alpha) = \frac{\alpha}{48 - \frac{192 \tanh(\sqrt{\alpha}/4)}{\sqrt{\alpha}}} \quad (5.5)$$

and α is defined by

$$\alpha = \frac{TL_0^2}{EI}. \quad (5.6)$$

The tension due to stretching is given by [26]

$$T_s = EA \frac{L - L_0}{L_0} = \frac{EA}{2L_0} \int_0^{L_0} \left(\frac{d\delta}{dx} \right)^2 dx = \frac{EA}{L_0} \int_0^{L_0/2} \left(\frac{d\delta}{dx} \right)^2 dx,$$

which yields the relationship between α and δ_{centre} :

$$\frac{\alpha \cosh^2(\sqrt{\alpha}/4)}{2 + \cosh(\sqrt{\alpha}/2) - 6 \frac{\sinh(\sqrt{\alpha}/2)}{\sqrt{\alpha}}} \left(1 - 4 \frac{\tanh(\sqrt{\alpha}/4)}{\sqrt{\alpha}} \right)^2 = \frac{A}{I} \delta_{\text{centre}}^2 \quad (5.7)$$

where A is the cross-sectional area of the fibre and $T = T_s$ is the magnitude of the tension

due to stretching of the fibre [9]. The function $f(\alpha)$, which is greater than or equal to one, is the factor by which tensile stress increases the fibre's resistance to deformation relative to Eq. 5.2 which considers only bending stress. An analytic expression for α cannot be found from Eq. 5.7, but α may be solved for numerically or approximated using a Padé approximant [9]. This model is described by Fig. 5.3 in the case that $T_0 = 0$, $L_{\text{eq}} = L_0$, and $T = T_s$ which is not negligible.

5.3.3 Bending With Both Deformation-Induced Tension and an Initial Tension

The model of Heidelberg *et al.* is extended by considering a constant initial tension, T_0 , applied to the fibre. Equation 5.3 defines the equilibrium shape of the fibre with $T = T_0 + T_s$. A fibre clamped between $x = 0$ and $x = L_0$ is symmetric about the centre. The solution for the displacement of the fibre between $x = 0$ and $x = L_0/2$ was found with assistance from Maple (Maplesoft, Waterloo, Canada), and is

$$\delta(x) = \frac{F_{\text{centre}}}{2T} \left[x - \frac{L_0}{\sqrt{\alpha}} \frac{\sinh \left[\sqrt{\alpha}(x/L_0 - 1/4) \right] + \sinh(\sqrt{\alpha}/4)}{\cosh(\sqrt{\alpha}/4)} \right]. \quad (5.8)$$

Restoring force versus deformation can still be expressed using Eqs. 5.4–5.6. However, the relationship between α and δ_{centre} has changed as is found below. Since the suspended fibre segment of length L_0 is under tension, its relaxed equilibrium length, L_{eq} , is less than L_0 . The tension due to stretching, relative to the relaxed equilibrium length, is given by [26]

$$T_s = EA \frac{L - L_0}{L_{\text{eq}}} = \frac{EA}{2L_{\text{eq}}} \int_0^{L_0} \left(\frac{d\delta}{dx} \right)^2 dx = \frac{EA}{L_{\text{eq}}} \int_0^{L_0/2} \left(\frac{d\delta}{dx} \right)^2 dx. \quad (5.9)$$

Substitution of Eq. 5.8 into Eq. 5.9 yields

$$\frac{T_s}{T} \frac{L_{\text{eq}}}{L_0} \left[\frac{\alpha \cosh^2(\sqrt{\alpha}/4)}{2 + \cosh(\sqrt{\alpha}/2) - 6 \frac{\sinh(\sqrt{\alpha}/2)}{\sqrt{\alpha}}} \left(1 - 4 \frac{\tanh(\sqrt{\alpha}/4)}{\sqrt{\alpha}} \right)^2 \right] = \frac{A}{I} \delta_{\text{centre}}^2. \quad (5.10)$$

By definition

$$T_0 = EA \frac{L_0 - L_{\text{eq}}}{L_{\text{eq}}}$$

so

$$L_{\text{eq}} = L_0 \left(\frac{EA}{T_0 + EA} \right). \quad (5.11)$$

Using Eq. 5.11 and $T_s = T - T_0$, Eq. 5.10 may be written as

$$\left(1 - \frac{T_0}{T}\right) \left(\frac{EA}{T_0 + EA}\right) \left[\frac{\alpha \cosh^2(\sqrt{\alpha}/4)}{2 + \cosh(\sqrt{\alpha}/2) - 6 \frac{\sinh(\sqrt{\alpha}/2)}{\sqrt{\alpha}}} \left(1 - 4 \frac{\tanh(\sqrt{\alpha}/4)}{\sqrt{\alpha}}\right)^2 \right] = \frac{A}{I} \delta_{\text{centre}}^2, \quad (5.12)$$

providing a relationship between α and δ_{centre} different from that of Eq. 5.7 in the previous model. Note that when $T_0 = 0$, Eq. 5.7 is recovered. The important quantities are indicated in Fig. 5.3.

5.3.4 Analysis of Force Curves

Data were imported into Igor Pro (WaveMetrics, Portland, USA) for analysis. Force curves were calibrated by dividing by the magnitude of the mean slope of force curves acquired on the hard substrate where the cantilever deflection equals the piezo displacement. A force curve on the substrate exhibits a linear relationship between piezo position and cantilever deflection after contact is made and, after normalization, has a slope of minus one. In contrast, a force curve on the fibre requires a larger piezo displacement, Δz , to reach the same cantilever deflection, Δy , due to the displacement of the fibre. In many AFM studies of other fibres, force curves on the fibre are linear, corresponding to deflection due to bending and/or shear. In this case, force curves on the fibre are found to be non-linear, indicating a need to include tensile stress. Example force curves from the substrate and the fibre are shown in Fig. 5.4.

For each force curve, the point at which the cantilever tip makes contact with the fibre was manually found and the flat baseline was truncated to obtain only the portion of the

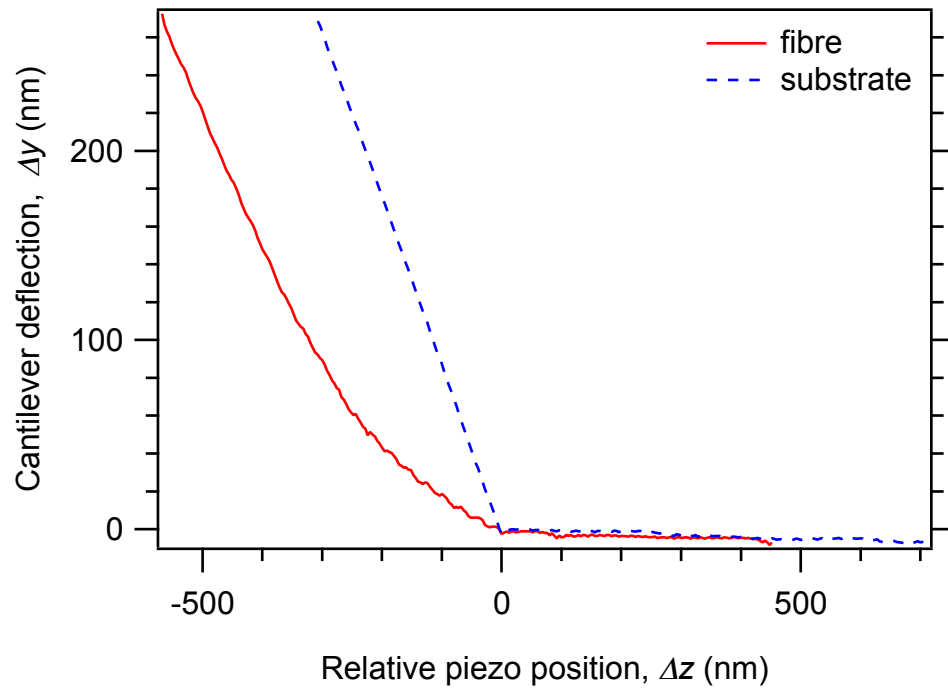


Figure 5.4: AFM force curves obtained by pushing against a fibre (solid curve) and a hard substrate (dashed curve). The sample approaches the cantilever with decreasing piezo position and the positions have been offset to place the points of contact at zero.

curve in which the tip and the fibre are in contact. After truncation, the curves of cantilever deflection versus piezo position were converted to fibre restoring force versus fibre displacement. The restoring force is equal to the cantilever deflection multiplied by the effective spring constant of the cantilever, and the fibre displacement is equal to the difference between the piezo displacement and the cantilever deflection. Fibres were assumed to have circular cross-sections for which $I = \pi d^4/64$ and $A = \pi d^2/4$ where d is the diameter of the fibre. The system of equations, Eqs. 5.4, 5.5, and 5.12, was fit to force-versus-displacement curves with only the Young's modulus, E , and the initial tension, T_0 , as free parameters. Example force versus displacement curves, one with low initial tension and one with high initial tension, and least-squares fits of the model are shown in Fig. 5.5. For comparison, fits to both the pure bending model and the model including bending and stretching without

an initial tension are shown. The range of the pure bending fits was restricted to δ_{centre} less than 50 nm to fit only the linear region. Fits of the other two models were restricted to less than 150 nm in the case of high initial tension to fit only the region of elastic deformation.

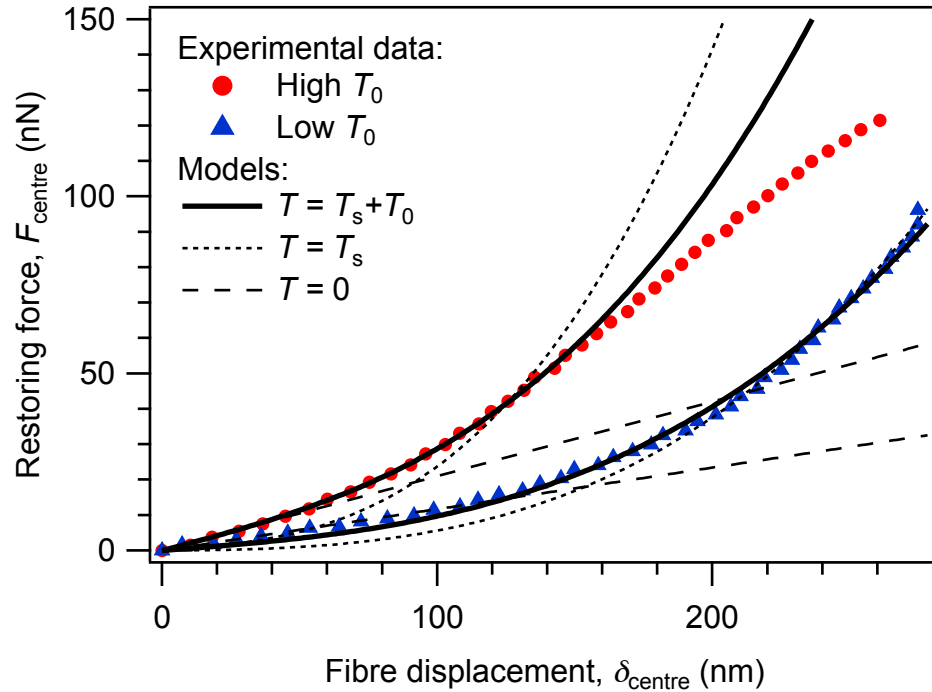


Figure 5.5: Experimental force versus displacement curves of single silk fibres with relatively low and relatively high initial tensions. For clarity, two-thirds of the points have been omitted. Fits of the model which accounts for bending, stretching, and an initial tension are shown with solid curves. For comparison, fits of the pure bending and bending plus stretching models are shown with dashed and dotted curves, respectively. The range of the pure bending fits was restricted to δ_{centre} less than 50 nm. Fits of the other two models were restricted to less than 150 nm in the case of high initial tension.

Though the model was developed for loads applied at the centre of the fibre, the moduli given by the model are fairly constant for at least the middle 20% of force curves as shown in Fig. 5.6. The modulus of the fibre is found by averaging values obtained from force curves located within $\pm 10\%$ of the centre of the fibre. The Young's moduli and initial

tensions of fibres and fibre bundles, obtained using the method described above for samples prepared with a mixture of adults and larvae, adults only, and larvae only, are recorded in Table 5.1. The diameters suggest three cases in which a measurement was made on a small bundle with a few fibres and four cases in which a measurement was made on a larger fibre bundle with a height above the substrate greater than 100 nm. In a few cases, consecutive measurements were made to test the repeatability of the experiments. Averages of the results for repeated measurements are recorded.

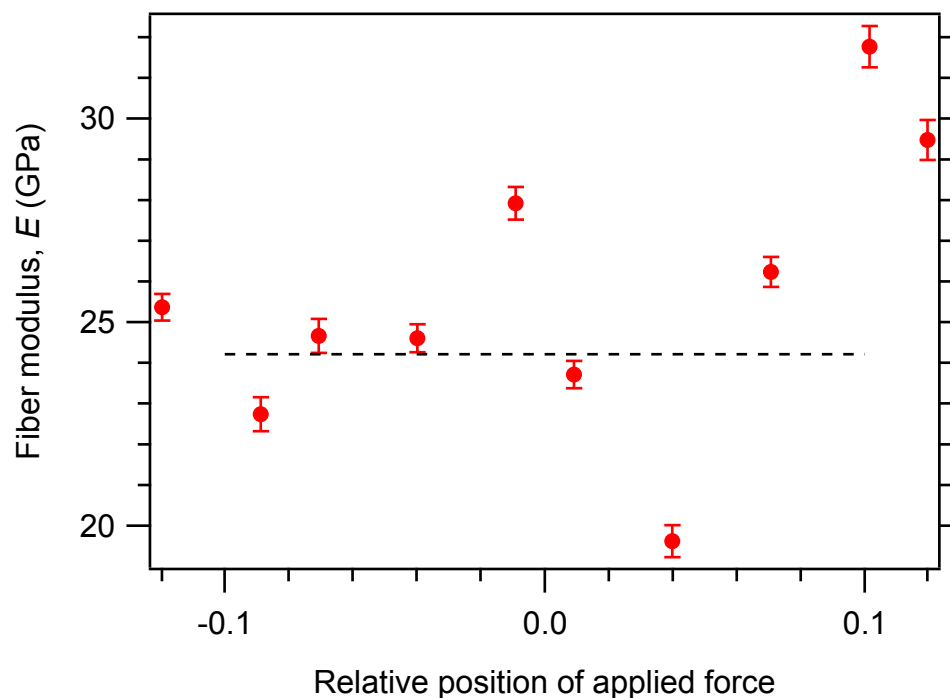


Figure 5.6: The Young's Modulus, obtained from fitting individual force curves, displayed versus the position of the force curve on the fibre as a fraction of the fibre length. The modulus of the fibre was determined by averaging the middle 20% of measurements. The dashed line indicates the average modulus.

Table 5.1: Silk fibre lengths, diameters, moduli, and initial tensions for samples prepared with adults and larvae, adults only, and larvae only.

Sample Type	Fibre	Location	L (μm)	d (nm)	E (GPa)	T_0 (nN)	
Mixed	1	a	4.2	57	27.4 ± 7.6	486 ± 40	
		b	4.1	59	27.6 ± 4.1	205 ± 10	
		c	3.9	51	40.6 ± 3.3	80 ± 12	
		d	4.1	59	15.7 ± 0.7	255 ± 5	
	2	a	6.8	75^a	39.9 ± 5.8	628 ± 39	
	3	a		4.2	170^b	26.5 ± 1.0	201 ± 86
				4.4	190^b	19.3 ± 2.3	0.7 ± 0.5
				4.4	200^b	25.3 ± 0.9	510 ± 100
	4	a		18	92^a	25.4 ± 4.3	621 ± 28
				b^c	16	78^a	31.6 ± 2.9
Adult	5	a	3.8	33	24.2 ± 1.0	9 ± 4	
	6	a	3.4	108^b	26.0 ± 1.2	231 ± 35	
	7	a		4.4	65	15.2 ± 1.1	91 ± 14
				b	4.4	54	20.5 ± 0.5
	8	a^d	4.0	54	19.6 ± 0.3	238 ± 2	
Larval	9	a	3.6	23	20.3 ± 4.0	14 ± 4	
	10	a^c	6.0	25	9.55 ± 0.48	32 ± 2	
	11	a^e	4.3	22	15.16 ± 0.56	90 ± 2	

^a Likely multiple fibres

^b Large fibre bundle

^c Average of four consecutive measurements

^d Average of three consecutive measurements

^e Average of two consecutive measurements

5.4 Discussion

Typical force versus displacement curves exhibit non-linear behaviour and a range of initial slopes as shown in Fig. 5.5. Though the force versus displacement curves are non-linear, agreement between the data and the model presented here, which assumes linear elastic response, indicates that the silk initially behave as a linear elastic material. The fibre under relatively high initial tension behaves linearly up to approximately 150 nm and the fibre under relatively low initial tension behaves linearly through the full range of displacements. In the examples shown, the pure bending model yields moduli of 167 ± 2 and 580 ± 20 GPa and the model of Heidelberg *et al.* yields moduli of 46.7 ± 0.9 and 32 ± 0.2 GPa. Both models significantly overestimate the modulus of the silk and provide inconsistent results. Further, when an initial tension is present, the pure bending model may not be used, even for very small deformations where the tension due to stretching is negligible. As shown by Eqs. 5.4–5.6, an initial tension results in α greater than zero, $f(\alpha)$ greater than one, and an increased slope of F_{centre} versus δ_{centre} .

From contact imaging on the substrate, adult fibres were found to have a diameter of approximately 55 nm. Several of the fibres from the mixed adult and larval samples have diameters matching those from the adult only samples. Fibres 1, 5, 7, and 8 from Table 5.1 are therefore classified as individual adult fibres. Their average diameter is 54 ± 3 nm. The larval fibres, fibres 9, 10, and 11, have a significantly smaller average diameter of 23.3 ± 0.9 nm. The remaining fibres have diameters greater than 70 nm and are considered to be bundles of fibres. These spider mite silk fibres have much smaller diameters than typical spider silk fibres which have diameters of several microns [27].

The initial tensions of the strands vary from negligibly small to hundreds of nanonewtons. These tensions may arise from mites pulling on the silk as they lay it down or from shrinkage of the silk after it has been deposited. The average of the moduli of the adult fibres is 24 ± 3 GPa and the average of the moduli of the larval fibres is 15 ± 3 GPa.

In cases of high initial tension, such as that shown in Fig. 5.5, the fibre was deformed beyond its elastic limit. In these cases, the force versus displacement curves were converted to stress versus strain and an estimate of the ultimate strength was made in cases where the stress became flat. Both adult and larval fibres had ultimate strengths of approximately 200–300 MPa. The ultimate strength was typically reached at 1–1.5% strain. To obtain an estimate of the toughness, several fibres were broken by repeating contact imaging with gradually increasing imaging force. An estimate of the lateral deformation of the centre of a fibre was made from the last contact image obtained before the fibre broke, allowing us to estimate a maximum strain of 4%. The stress is assumed to increase linearly from 0 to 250 MPa between 0% and 1% strain and to remain constant thereafter until the fibre breaks at 4% strain. This allows an order of magnitude estimate of 9 MJ/m^3 for the toughness.

The elastic modulus, tensile strength, breaking strain, and toughness of the spider mite silk fibres is compared to those of the *Nephila clavipes* spider and the *Bombyx mori* silk worm silks in Table 5.2. The spider mite silk has a higher modulus than the spider and silk worm silks. However, the tensile strength, breaking strain, and toughness of the spider mite silk are lower than those of the spider and silk worm silks.

A technique where force measurements were recorded at many positions along the length of the fibres was employed. In cases where the pure bending model applies, this offers the potential to more accurately determine the modulus and to justify the use of the pure bending model [16]. Here, applying the pure bending model to the small deformation limit yielded unreasonably large and inconsistent values for the modulus. Also, the position dependence of the slopes of the AFM force curves did not agree with the predictions of the pure bending model [16], further indicating that the pure bending model was insufficient, even for very small deformations. The disadvantage of this approach is that it may not be sufficient for determining the ultimate strength and toughness of a material.

To obtain good estimates of the modulus, ultimate strength, and toughness, the technique of breaking a fibre by performing a single, large deformation measurement at the fi-

Table 5.2: Comparison of the elastic modulus, tensile strength, breaking strain, and toughness of adult spider mite, spider, and silkworm silks. The spider and silkworm data are from Elices *et al.* [27].

Silk	Elastic	Tensile	Breaking	
	Modulus	Strength	Strain	Toughness
	(GPa)	(GPa)	%	(MJ/m ³)
Adult Spider Mite ^a	24 ± 3	~0.2–0.3	~4	~9
Spider ^b	1–10	1.8	30	≥130
Silk Worm ^c	5	0.6	12	≥50

^a *Tetranychus urticae*

^b *Nephila clavipes*

^c *Bombyx mori*

bre's centre may be used [9, 11]. The two techniques are complimentary and it is suggested to first record many small elastic-limit deformation measurements to accurately measure the modulus and to test the chosen mechanical model, then to perform one large deformation measurement at the centre to determine additional mechanical properties. Here the open-loop scanner of the atomic force microscope did not allow the cantilever tip to be accurately placed at the centre of fibres for single large deformation measurements.

5.5 Conclusion

The mechanical properties of adult and larval spider mite silk nanofibres deposited onto silicon gratings were determined by measuring fibre restoring force versus vertical displacement with an atomic force microscope. The fibres were modelled as clamped beams made of a linear elastic material. Since the fibre displacement was greater than the fibre radius, tensile stresses had to be considered [9]. Further, it was determined that an initial tension in the fibres also had to be considered.

A model has been presented, for determining the force versus displacement mechanical behaviour of suspended nanofibres with clamped boundaries, that accounts for bending stress, tensile stress due to elongation during deformation, and tensile stress due to an initial tension. It appears that an initial tensile stress has never been considered in previous AFM measurements of fibres. Despite force versus displacement curves ranging from nearly linear to highly nonlinear, the model provides consistent measurements of the elastic modulus of spider mite silk fibres. Fibres produced by adult and larval spider mites have average diameters of 54 ± 3 nm and 23.3 ± 0.9 nm, respectively. Adult fibres have a modulus of 24 ± 3 GPa while larval fibres have a modulus of 15 ± 3 GPa. Both adult and larval fibres exhibit an ultimate strength of approximately 200–300 MPa which is reached at a strain of approximately 1–1.5%. The fibre break at an estimated strain of 4% and their toughness is of order 9 MJ/m³.

5.6 Bibliography for Chapter 5

1. *Silk Polymers: Materials Science and Biotechnology* (eds Kaplan, D., Adams, W. W., Farmer, B. & Viney, C.) (American Chemical Society, 1994).
2. Altman, G. H. *et al.* "Silk-based biomaterials." *Biomaterials* **24**, 401–416 (2003).
3. MacIntosh, A. C., Kearns, V. R., Crawford, A. & Hatton, P. V. "Skeletal tissue engineering using silk biomaterials." *J. Tissue Eng. Regen. Med.* **2**, 71–80 (2008).
4. Hofmann, S. *et al.* "Cartilage-like Tissue Engineering Using Silk Scaffolds and Mesenchymal Stem Cells." *Tissue Eng.* **12**, 2729–2738 (2006).
5. Holland, C., Terry, A. E., Porter, D. & Vollrath, F. "Natural and unnatural silk." *Polymer* **48**, 3388–3392 (2007).
6. Gosline, J. M., DeMont, M. E. & Denny, M. W. "The structure and properties of spider silk." *Endeavour* **10**, 37–43 (1986).
7. Lee, S.-H., Tekmen, C. & Sigmund, W. M. "Three-point bending of electrospun TiO₂ nanofibers." *Mat. Sci. Eng. A-Struct.* **398**, 77–81 (2005).
8. Wu, B., Heidelberg, A. & Boland, J. J. "Mechanical properties of ultrahigh-strength gold nanowires." *Nat. Mater.* **4**, 525–529 (2005).
9. Heidelberg, A. *et al.* "A generalized description of the elastic properties of nanowires." *Nano Lett.* **6**, 1101–1106 (2006).
10. Ni, H., Li, X. & Gao, H. "Elastic modulus of amorphous SiO₂ nanowires." *Appl. Phys. Lett.* **88**, 043108:1–3 (2006).
11. Wen, B., Sader, J. E. & Boland, J. J. "Mechanical Properties of ZnO Nanowires." *Phys. Rev. Lett.* **101**, 175502:1–4 (2008).
12. Salvetat, J.-P. *et al.* "Mechanical properties of carbon nanotubes." *Appl. Phys. A* **69**, 255–260 (1999).
13. Kim, G.-T., Gu, G., Waizmann, U. & Roth, S. "Simple method to prepare individual suspended nanofibers." *Appl. Phys. Lett.* **80**, 1815–1817 (2002).
14. Guhadós, G., Wan, W., Sun, X. & Hutter, J. L. "Simultaneous measurement of Young's and shear moduli of multiwalled carbon nanotubes using atomic force microscopy." *J. Appl. Phys.* **101**, 033514–1–5 (2007).
15. Tan, E. P. S. & Lim, C. T. "Physical properties of a single polymeric nanofiber." *Appl. Phys. Lett.* **84**, 1603–1605 (2004).

16. Guhados, G., Wan, W. & Hutter, J. L. "Measurement of the Elastic Modulus of Single Bacterial Cellulose Fibers Using Atomic Force Microscopy." *Langmuir* **21**, 6642–6646 (2005).
17. Shin, M. K., Kim, S. I. & Kim, S. J. "Size-dependent elastic modulus of single electroactive polymer nanofibers." *Appl. Phys. Lett.* **89**, 231929:1–3 (2006).
18. Iwamoto, S., Kai, W., Isogai, A. & Iwata, T. "Elastic Modulus of Single Cellulose Microfibrils from Tunicate Measured by Atomic Force Microscopy." *Biomacromolecules* **10**, 2571–2576 (2009).
19. Chen, C. Q., Shi, Y., Zhang, Y. S., Zhu, J. & Yan, Y. J. "Size Dependence of Young's Modulus in ZnO Nanowires." *Phys. Rev. Lett.* **96**, 075505:1–4 (2006).
20. Grbić, M. *et al.* "The genome of the two-spotted spider mite *Tetranychus urticae*: a model for plant insect interactions (tentative title)." *Nature* (In preparation).
21. Hutter, J. L. & Bechhoefer, J. "Calibration of atomic-force microscope tips." *Rev. Sci. Instrum.* **64**, 1868–1873 (1993).
22. Butt, H.-J. & Jaschke, M. "Calculation of thermal noise in atomic force microscopy." *Nanotechnol.* **6**, 1–7 (1995).
23. Walters, D. A. *et al.* "Short cantilevers for atomic force microscopy." *Rev. Sci. Instrum.* **67**, 3583–3590 (1996).
24. Hutter, J. L. "Comment on Tilt of Atomic Force Microscope Cantilevers: Effect on Spring Constant and Adhesion Measurements." *Langmuir* **21**, 2630–2632 (2005).
25. Timoshenko, S. P. "On the correction for shear of the differential equation for transverse vibrations of prismatic bars." *Philos. Mag.* **41**, 744 (1921).
26. Landau, L. D. & Lifshitz, E. M. *Theory of elasticity, 2nd Ed.* (Pergamon Press, 1970).
27. Elices, M., Pérez-Rigueiro, J., Plaza, G. R. & Guinea, G. V. "Finding Inspiration in Argiope Trifasciata Spider Silk Fibers." *JOM* **57**, 60–66 (2005).

Chapter 6

Conclusions

6.1 Thesis Summary

Polyvinyl Alcohol (PVA) is a hydrophilic and biocompatible polymer whose hydrogels are used for magnetic resonance imaging (MRI) and ultrasound phantoms, drug delivery systems, and wound dressings. Physically cross-linked PVA hydrogels produced by freezing and thawing PVA solution can be made with mechanical properties matching those of porcine aorta and are being investigated for use as heart valve stents and artificial heart valves [1, 2]. The mechanical properties of hydrogels may be further controlled and improved by addition of reinforcing material such as nanofibres, hydroxyapatite, or clay nanoparticles [3–9]. Characterization of the structure of PVA hydrogels, understanding of the connection between structure and bulk mechanical properties, and determination of the mechanical properties of materials suitable for reinforcing PVA hydrogels may hasten the development of biomedical prostheses used to improve our longevity and quality of life.

In Chapter 2, the structures of isotropic and anisotropic PVA hydrogels were characterized using small-angle neutron scattering (SANS), ultra small-angle neutron scattering (USANS), and atomic force microscopy (AFM). The structure was successfully modelled as dense blobs of PVA arranged into fractal aggregates.

In Chapter 3, entropy was identified as the dominant source of the observed stress versus strain. It was found that the simple 3-chain model of Treloar [10] and the 8-chain model of Arruda and Boyce [11] were capable of modelling isotropic uniaxial extension stress versus strain data. Further, anisotropic versions of the 3-chain and 8-chain models were developed and found to adequately model the uniaxial extension of anisotropic PVA hydrogels. Though the mechanical models were simpler than the structural model of Chapter 2, the models were found to be compatible.

In Chapter 4, the mechanical properties of spider mite silk nanofibres were measured using AFM. Restoring force versus lateral displacement was recorded by pushing suspended nanofibres with the tip of an atomic force microscope cantilever. Previously reported models could not account for the varied curvature of force versus displacement curves, and a new model, which accounted for an initial tension, was developed and found to accurately model the data.

6.2 Future Work

The following recommendations for continued mechanical modelling of PVA hydrogels and characterization of spider mite silk nanofibres are made.

6.2.1 Mechanical Modelling of PVA hydrogels

Mechanical modelling could be improved by performing numerical simulations of networks that more closely resemble the true structure. Improvements include:

1. arranging the crystallites in fractal aggregates,
2. superimposing a porous structure on the network,
3. adding polydispersity to the contour length of polymer strands,

4. enforcing non-zero equilibrium fractional extension of polymer strands via a repulsive force between, crystallites
5. incorporating reinforcing structures such as nanofibres, and
6. simulating compression, torsion, biaxial extension, and shear.

6.2.2 Spider Mite Silk Fibres

High priority next steps for characterization of spider mite silk are to accurately determine the ultimate strength and toughness of the fibres by acquiring force versus displacement data to the breaking point and to measure the mechanical properties of synthetic electrospun spider mite silk fibres. Ideally, a closed loop system would be used to accurately position the atomic force microscope cantilever tip at the centre fibre before performing a single force measurement. Vertical displacements would require gratings with deeper trenches. Alternatively, horizontal displacements could be used [12].

6.3 Bibliography for Chapter 6

1. Wan, W. K., Campbell, G., Zhang, Z. F., Hui, A. J. & Boughner, D. R. “Optimizing the Tensile Properties of Polyvinyl Alcohol Hydrogel for the Construction of a Bioprosthetic Heart Valve Stent.” *J. Biomed. Mater. Res.* **63**, 854–861 (2002).
2. Millon, L. E., Mohammadi, H. & Wan, W. K. “Anisotropic Polyvinyl Alcohol Hydrogel for Cardiovascular Applications.” *J. Biomed. Mater. Res. Part B: Appl. Biomater.* **79B**, 305–311 (2006).
3. Millon, L. E. & Wan, W. K. “The Polyvinyl Alcohol-Bacterial Cellulose System As a New Nanocomposite for Biomedical Applications.” *J. Biomed. Mater. Res. Part B: Appl. Biomater.* **79B**, 245–253 (2006).
4. Millon, L. E., Guhados, G. & Wan, W. “Anisotropic Polyvinyl Alcohol – Bacterial Cellulose Nanocomposite for Biomedical Applications.” *J. Biomed. Mater. Res. B: Appl. Biomater.* **86B**, 444–452 (2008).
5. Millon, L. E., Oates, C. J. & Wan, W. “Compression Properties of Polyvinyl Alcohol – Bacterial Cellulose Nanocomposite.” *J. Biomed. Mater. Res. B: Appl. Biomater.* **90B**, 922–929 (2009).
6. Wu, G., Su, B., Zhang, W. & Wang, C. “*In vitro* behaviors of hydroxyapatite reinforced polyvinyl alcohol hydrogel composite.” *Mater. Chem. Phys.* **107**, 364–369 (2008).
7. Xu, F., Li, Y., Deng, Y. & Xiong, J. “Porous nano-hydroxyapatite/poly(vinyl alcohol) composite hydrogel as artificial cornea fringe: characterization and evaluation *in vitro*.” *J. Biomater. Sci. Polymer Edn.* **19**, 431–439 (2008).
8. Pan, Y., Xiong, D. & Gao, F. “Viscoelastic behavior of nano-hydroxyapatite reinforced poly(vinyl alcohol) gel biocomposites as an articular cartilage.” *J. Mater. Sci.-Mater. M.* (2008).
9. Kokabi, M., Sirousazar, M. & Hassan, Z. M. “PVAclay nanocomposite hydrogels for wound dressing.” *Eur. Polym. J.* **43**, 773–781 (2007).
10. Treloar, L. R. G. *The physics of rubber elasticity* (Oxford University Press, USA, 2005).
11. Arruda, E. M. & Boyce, M. C. “A Three-dimensional constitutive model for the large stretch behavior of rubber elastic materials.” *J. Mech. Phys. Solids* **41**, 389–412 (1993).

12. Wu, B., Heidelberg, A. & Boland, J. J. “Mechanical properties of ultrahigh-strength gold nanowires.” *Nat. Mater.* **4**, 525–529 (2005).

Appendix A

Attachment of Microspheres to Atomic Force Microscope Cantilevers

Glass microspheres were glued onto the end of NP-S atomic force microscopy (AFM) cantilevers (Digital Instruments, Santa Barbara, CA) with ultraviolet (UV) curing, Norland Optical Adhesive #81 (Norland Products Inc., New Brunswick, NJ). To achieve this, a thin strip of glue was created on a silicon substrate using a fine wire. Functionalized microspheres were dispersed onto a second silicon substrate, and the water was evaporated at low heat with a hotplate. A cantilever was placed in the AFM cantilever holder and both the glue substrate and holder were mounted on the AFM. The tip of the cantilever was lowered, moved into the glue strip, and raised. The holder and glue substrate were removed. At this time, the bead substrate and the holder were mounted on the AFM. The cantilever was lowered near a bead, then the cantilever was moved such that the tip made contact with the bead. The cantilever holder was removed, and the bead placement was checked with an optical microscope, as shown in Figure A.1. Finally, the cantilever was placed under a UV lamp for 15 minutes to cure the glue.

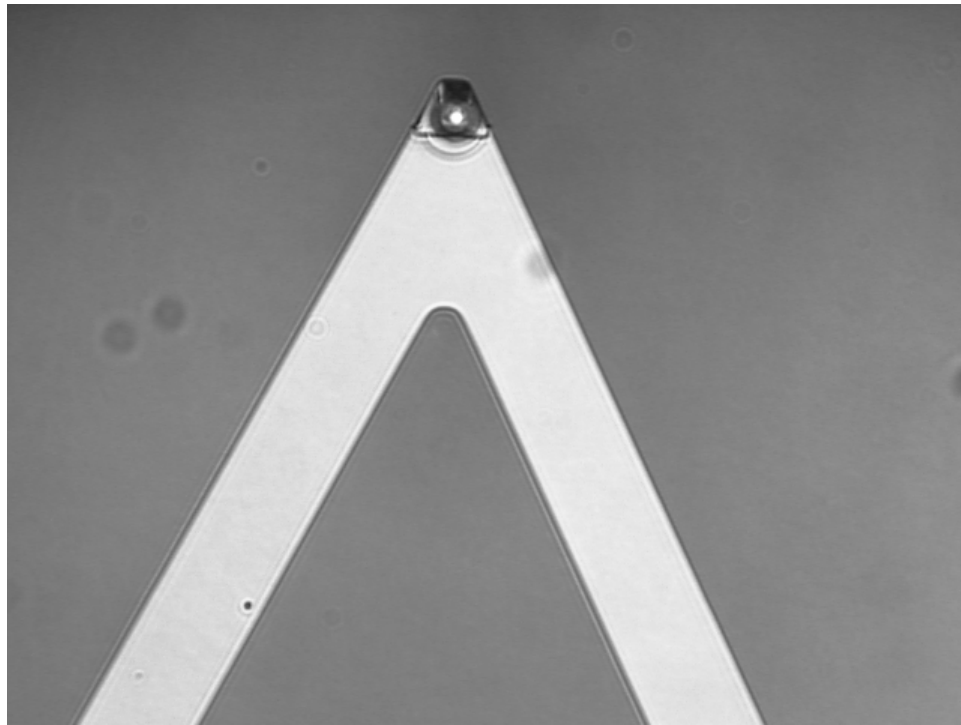


Figure A.1: Glass bead glued to a triangular NP-S cantilever.

Appendix B

Copyright Permissions

Sage Publications

Dear Stephen,

Thank you very much for your email.

You are very welcome to republish the following material : H Mohammadi, D Boughner, L E Million and W K Wan, Design and simulation of a poly(vinyl alcohol)—bacterial cellulose nanocomposite mechanical aortic heart valve prosthesis *Proceedings of the Institution of Mechanical Engineers*, Part H: Journal of Engineering in Medicine August 1, 2009 223: 697-711 in your doctoral thesis.

Please consider this email as written permission and make sure to include all academic referencing to the original material. Please inform the authors of this re-use.

I hope this helps,

Kind regards,

Valérie Bernard
Permissions Assistant

SAGE Publications Ltd

1 Oliver's Yard, 55 City Road

London, EC1Y 1SP

UK

Tel: [+44 \(0\) 207 336 9146](tel:+44(0)2073369146)

Fax: [+44 \(0\) 207 324 8600](tel:+44(0)2073248600)

www.sagepub.co.uk

SAGE Publications Ltd, Registered in England No.1017514

Los Angeles | London | New Delhi

Singapore | Washington DC

Thank you for considering the environment before printing this email.

American Institute of Physics License

AMERICAN INSTITUTE OF PHYSICS LICENSE TERMS AND CONDITIONS

Mar 23, 2011

This is a License Agreement between Stephen D Hudson ("You") and American Institute of Physics ("AIP") provided by Copyright Clearance Center ("CCC"). The license consists of your order details, the terms and conditions provided by American Institute of Physics, and the payment terms and conditions.

All payments must be made in full to CCC. For payment instructions, please see information listed at the bottom of this form.

License Number	2634990035785
License date	Mar 23, 2011
Licensed content publisher	American Institute of Physics
Licensed content publication	Journal of Chemical Physics
Licensed content title	Characterization of anisotropic poly(vinyl alcohol) hydrogel by small- and ultra-small-angle neutron scattering
Licensed content author	Stephen D. Hudson, Jeffrey L. Hutter, Mu-Ping Nieh, Jeremy Pencer, et al.
Licensed content date	Jan 20, 2009
Volume number	130
Issue number	3
Type of Use	Thesis/Dissertation
Requestor type	Author (original article)
Format	Print and electronic
Portion	Excerpt (> 800 words)
Will you be translating?	No
Title of your thesis / dissertation	Structure and Strength: Anisotropic Polyvinyl Alcohol Hydrogels and Spider Mite Silk Fibres
Expected completion date	May 2011
Estimated size (number of pages)	150
Total	0.00 USD

Terms and Conditions

American Institute of Physics -- Terms and Conditions: Permissions Uses

American Institute of Physics ("AIP") hereby grants to you the non-exclusive right and license to use and/or distribute the Material according to the use specified in your order, on a one-time basis, for the specified term, with a maximum distribution equal to the number that you have ordered. Any links or other content accompanying the Material are not the subject of this license.

1. You agree to include the following copyright and permission notice with the reproduction of the Material: "Reprinted with permission from [FULL CITATION]."

Copyright [PUBLICATION YEAR], American Institute of Physics." For an article, the copyright and permission notice must be printed on the first page of the article or book chapter. For photographs, covers, or tables, the copyright and permission notice may appear with the Material, in a footnote, or in the reference list.

2. If you have licensed reuse of a figure, photograph, cover, or table, it is your responsibility to ensure that the material is original to AIP and does not contain the copyright of another entity, and that the copyright notice of the figure, photograph, cover, or table does not indicate that it was reprinted by AIP, with permission, from another source. Under no circumstances does AIP, purport or intend to grant permission to reuse material to which it does not hold copyright.
3. You may not alter or modify the Material in any manner. You may translate the Material into another language only if you have licensed translation rights. You may not use the Material for promotional purposes. AIP reserves all rights not specifically granted herein.
4. The foregoing license shall not take effect unless and until AIP or its agent, Copyright Clearance Center, receives the Payment in accordance with Copyright Clearance Center Billing and Payment Terms and Conditions, which are incorporated herein by reference.
5. AIP or the Copyright Clearance Center may, within two business days of granting this license, revoke the license for any reason whatsoever, with a full refund payable to you. Should you violate the terms of this license at any time, AIP, American Institute of Physics, or Copyright Clearance Center may revoke the license with no refund to you. Notice of such revocation will be made using the contact information provided by you. Failure to receive such notice will not nullify the revocation.
6. AIP makes no representations or warranties with respect to the Material. You agree to indemnify and hold harmless AIP, American Institute of Physics, and their officers, directors, employees or agents from and against any and all claims arising out of your use of the Material other than as specifically authorized herein.
7. The permission granted herein is personal to you and is not transferable or assignable without the prior written permission of AIP. This license may not be amended except in a writing signed by the party to be charged.
8. If purchase orders, acknowledgments or check endorsements are issued on any forms containing terms and conditions which are inconsistent with these provisions, such inconsistent terms and conditions shall be of no force and effect. This document, including the CCC Billing and Payment Terms and Conditions, shall be the entire agreement between the parties relating to the subject matter hereof.

This Agreement shall be governed by and construed in accordance with the laws of the State of New York. Both parties hereby submit to the jurisdiction of the courts of New York County for purposes of resolving any disputes that may arise hereunder.

Gratis licenses (referencing \$0 in the Total field) are free. Please retain this printable license for your reference. No payment is required.

If you would like to pay for this license now, please remit this license along with your payment made payable to "COPYRIGHT CLEARANCE CENTER" otherwise you will be invoiced within 48 hours of the license date. Payment should be in the form of a check or money order referencing your account number and this invoice number RLNK10955853.

Once you receive your invoice for this order, you may pay your invoice by credit card. Please follow instructions provided at that time.

Make Payment To:
Copyright Clearance Center
Dept 001
P.O. Box 843006
Boston, MA 02284-3006

For suggestions or comments regarding this order, contact Rightslink Customer Support: customer@copyright.com or +1-877-622-5543 (toll free in the US) or +1-978-646-2777.

International Union of Crystallography 1

Dear Dr Hudson

Thank you for your message.

Permission is hereby granted, on behalf of the IUCr, for you to reproduce Figure 1 from

J. Appl. Cryst. (1998). 31, 430-445 [doi:10.1107/S0021889897017020]
C. J. Glinka, J. G. Barker, B. Hammouda, S. Krueger, J. J. Moyer and
W. J. Orts

subject to the following conditions:

1. Reproduction is intended in a primary journal, secondary journal, CD-ROM, book or thesis.
2. The original article in which the material appeared is cited.
3. IUCr's copyright permission is indicated next to the Figure/Table in print. In electronic form, this acknowledgement must be visible at the same time as the Figure/Table, and must be hyperlinked to Crystallography Journals Online (<http://journals.iucr.org/>).

Best wishes
Peter Strickland

Managing Editor
IUCr Journals

IUCr Editorial Office, 5 Abbey Square, Chester CH1 2HU, England
Phone: 44 1244 342878 Fax: 44 1244 314888 Email: ps@iucr.org
Ftp: <ftp://iucr.org> WWW: <http://journals.iucr.org/>

International Union of Crystallography 2

Dear Dr Hudson

Thank you for your message.

Permission is hereby granted, on behalf of the IUCr, for you to reproduce Figure 1 from

J. Appl. Cryst. (2005). 38, 1004-1011 [doi:10.1107/S0021889805032103]
J. G. Barker, C. J. Glinka, J. J. Moyer, M. H. Kim, A. R. Drews and
M. Agamalian

subject to the following conditions:

1. Reproduction is intended in a primary journal, secondary journal, CD-ROM, book or thesis.
2. The original article in which the material appeared is cited.
3. IUCr's copyright permission is indicated next to the Figure/Table in print. In electronic form, this acknowledgement must be visible at the same time as the Figure/Table, and must be hyperlinked to Crystallography Journals Online (<http://journals.iucr.org/>).

Best wishes
Peter Strickland

Managing Editor
IUCr Journals

IUCr Editorial Office, 5 Abbey Square, Chester CH1 2HU, England
Phone: 44 1244 342878 Fax: 44 1244 314888 Email: ps@iucr.org
Ftp: <ftp://iucr.org> WWW: <http://journals.iucr.org/>

Curriculum Vitae

Stephen Donald Hudson

Education

- 2011** **Doctor of Philosophy (PhD) in Physics**
The University of Western Ontario, London, Ontario, Canada
- 2005** **Honours Bachelor of Science (BSc) in Physics**
The University of Western Ontario, London, Ontario, Canada

Awards and Scholarships

- 2009** Western Graduate Thesis Research Award
- 2007** Lillian Margaret and Walter David Jackson Scholarship
- 2007 – 2010** NSERC 3 year Doctoral Postgraduate Scholarship
- 2007** Western Graduate Thesis Research Award
- 2006** Ontario Graduate Scholarship
- 2006** Western Graduate Thesis Research Award
- 2005** Ontario Graduate Scholarship
- 2005** Raymond Compton Dearle Gold Medal in Physics
- 2003** NSERC Undergraduate Student Research Award
- 2001** Western Scholarship of Excellence

Related Work Experience

- 2010 – 2011** Measured the mechanical properties of silk nanofibres using the atomic force microscope and developed a new mechanical model
- 2005 – 2010** Studied the structure and properties of anisotropic poly(vinyl alcohol) hydrogels using neutron scattering, atomic force microscopy, optical microscopy, and numerical simulation
- 2004 – 2005** Developed and tested a protocol for functionalizing atomic force microscope cantilevers with protein and measured chemical stimulation of cell receptor-protein bonding using an atomic force microscope
- 2003 – 2004** Compared atomic force microscope cantilever calibration methods and refined our labs implementation of the thermal noise method

2003 Studied the effect of kinetic inhibitors on wax crystallization in a model diesel fuel using an optical microscope

Publications

Grbić, M., *et al.* (52 authors including **Hudson, S.D.**) “The genome of *Tetranychus urticae* reveals herbivorous pest adaptations.” *Nature* (In preparation).

Hudson, S.D., Hutter, J.L., Zhurov, V., and Grbić, M. “Measurement of the Elastic Modulus of Spider Mite Silk Fibers Using Atomic Force Microscopy.” *Nano Letters* (In preparation).

Hudson, S.D., Hutter, J.L., Millon, L.E., Wan, W. “Anisotropic Poly(Vinyl Alcohol) Hydrogel: Connection Between Structure and Bulk Mechanical Properties.” *Journal of Applied Physics* (In preparation).

Hudson, S.D. “Structure and Strength: Anisotropic Polyvinyl Alcohol Hydrogels and Spider Mite Silk Fibres.” PhD thesis, The University of Western Ontario, 161 pages.

Hudson, P., **Hudson, S.D.**, Handler, W.B., and Chronik, B.A. “Finite-length shim coil design using a fourier series minimum inductance and minimum power algorithm.” *Concepts in Magnetic Resonance Part B* **37B**, 245–253 (2010).

Hudson, P., **Hudson, S.D.**, Handler, W.B., Scholl, T.J., and Chronik, B.A. “Quantitative comparison of minimum inductance and minimum power algorithms for the design of shim coils for small animal imaging.” *Concepts in Magnetic Resonance Part B* **37B**, 65–74 (2010).

Hudson, S.D., Hutter, J.L., Nieh, M.-P., Pencer, J., Millon, L.E., and Wan, W.K. “Characterization of Anisotropic Poly(Vinyl Alcohol) Hydrogel by Small- and Ultra Small- Angle Neutron Scattering.” *Journal of Chemical Physics* **130**, 034903-1–9 (2009).

Tetervak, A., **Hudson, S.**, Zhang, J., and Hutter, J.L. “Continuum model for mesh crystallization.” *Physical Review E* **71**, 051606-1–8 (2005).

Hutter, J.L., **Hudson, S.**, Smith, C., Tetervak, A., and Zhang, J. “Banded crystallization of tricosane in the presence of kinetic inhibitors during directional solidification.” *Journal of Crystal Growth* **273**, 292–302 (2004).

Hudson, S.D. “Measuring the effects of stimulation on cell-protein interactions using the atomic force microscope.” Honours BSc thesis, The University of Western Ontario, 75 pages.

Conference Presentations

Hudson, S., Hutter, J., Millon, L., Wan, W. “Mechanical modelling of anisotropic poly (vinyl alcohol) hydrogels.” The Canadian Association of Physicists Congress (2010).

Hudson, S., Hutter, J., Millon, L., Wan, W., Nieh, M.-P. “Anisotropic Poly(Vinyl Alcohol) Hydrogel: Connection Between Structure and Bulk Mechanical Properties.” American Physical Society March Meeting (2009).

Hudson, S.D., Hutter, J.L., Nieh, M.-P., Millon, L.E., and Wan, W. “SANS and USANS of Anisotropic Polyvinyl Alcohol Hydrogels.” The Canadian Association of Physicists Congress (2008).

Hudson, S.D., Hutter, J.L., Nieh, M.-P., Millon, L.E., and Wan, W. “SANS and USANS of Anisotropic Poly(vinyl alcohol) Hydrogels.” American Conference on Neutron Scattering (2008, poster).

Hudson, S.D., Millon, L.E., Nieh, M.-P., Pencer, J., Lin, M., Wan, W., and Hutter, J.L. “Structure and Properties of Poly(Vinyl Alcohol) Hydrogels.” The Canadian Association of Physicists Congress (2006).

Hudson, S.D., Millon, L.E., Nieh, M.-P., Pencer, J., Lin, M., Wan, W., and Hutter, J.L. “Small- and ultra small- angle neutron scattering study of anisotropic poly(vinyl alcohol) hydrogel structures.” AFMNet Hydrogels Workshop. (2006, poster)

Hudson, S.D., Hutter, J.L., Chan, B.M.C., Uniyal, S., and Wan, W. “Measuring the effect of stimulation on cell-protein interactions using the atomic force microscope.” Chemical Biophysics Symposium, P32. (2005, poster).

Hutter, J., **Hudson, S.**, Tetervak, A., and Zhang, J. “Continuous Model of Banded Growth in Alkane Crystallization.” American Physical Society March Meeting (2004).